Electrical and optical detections of spin-filter effects in the ferromagnetic metal / semiconductor junctions

Xiaoxin Li

ÉCOLE POLYTECHNIQUE

Thèse présentée pour obtenir le grade de

DOCTEUR DE L'ÉCOLE POLYTECHNIQUE

Spécialité: Physique des Solides

par

Xiaoxin LI

Détections électriques et optiques des effets de filtre à spin dans les jonctions métal ferromagnétique / semi-conducteur

Soutenue le 24 juin 2011 devant le jury composé de :

Dr. André Thiaville	Université de Paris-Sud - LPS	Rapporteur
Dr. Wolfgang Weber	IPCMS	Rapporteur
Dr. Michel Hehn	Universite Henri Poincaré - LPM	Examinateur
Dr. Jean-Eric Wegrowe	Ecole Polytechnique – LSI	Président du jury
Dr. Yves Lassailly	Ecole Polytechnique – PMC	Directeur de thèse
Dr. Jacques Peretti	Ecole Polytechnique – PMC	Co-Directeur de thèse

ÉCOLE POLYTECHNIQUE

Thesis presented for the degree of

DOCTOR OF ÉCOLE POLYTECHNIQUE

Speciality : Solid-State Physics

by

Xiaoxin LI

Electrical and optical detections of spin-filter effects in the ferromagnetic metal / semiconductor junctions

Defended on the 24th June, 2011 in front of the jury composed of :

Dr. André Thiaville	Université de Paris-Sud - LPS	Referee
Dr. Wolfgang Weber	IPCMS	Referee
Dr. Michel Hehn	Universite Henri Poincaré - LPM	Examiner
Dr. Jean-Eric Wegrowe	Ecole Polytechnique – LSI	President of the jury
Dr. Yves Lassailly	Ecole Polytechnique – PMC	Supervisor
Dr. Jacques Peretti	Ecole Polytechnique – PMC	Co-Supervisor

To My Wife and Our Parents

Résumé

L'objectif de ce travail de thèse est d'étudier expérimentalement le transport d'électrons chauds dépendant du spin à travers une jonction métal ferromagnétique / semi-conducteur. En pratique, un faisceau d'électrons polarisés de spin, émis par une photocathode GaAs en condition de pompage optique, est injecté dans la jonction. L'énergie d'injection peut être réglée entre 5 et 3000 eV. Le courant transmis au-dessus de la barrière métal / semi-conducteur montre une asymétrie de spin due à l'effet de filtre à spin de la couche magnétique. Pour la détection directe du courant électrique transmis dans un dispositif métal / semi-conducteur, on a besoin d'une structure ayant un fort caractère redresseur avec une résistance dynamique de jonction très élevée (typiquement quelques MΩ). Ces propriétés sont obtenus par l'introduction d'une couche mince (de quelques nanomètres) interfaciale d'oxyde entre le métal et le semi-conducteur (structure de type MIS). Nous montrons que la transmission d'électrons chands et les effets de filtre à spin à travers les structures MIS dépendent fortement la couche d'oxyde. Afin de surmonter les difficultés relatives à la détection électrique de la transmission d'électrons dans les jonctions MIS, nous avons développé une méthode de détection optique basée sur la mesure de la cathodoluminescence émise par la recombinaison d'électrons transmis dans le collecteur semi-conducteur. Pour ce faire, nous avons conçu la structure Fe / GaAs / InGaAs / GaAs, qui comprend les puits quantiques InGaAs, dans lesquels les électrons transmis à travers la jonction se recombinent avec les trous. L'intensité de la lumière de recombinaison est détectée en face arrière du le substrat GaAs. Nous démontrons que cette technique permet en effet la détection optique de la transmission d'électrons et de l'effet de filtre à spin dans les structures métal ferromagnétique / semi-conducteur. Les limites et les perspectives de la spectroscopie de cathodoluminescence sont discutées.

Mots clés: transmission d'électrons polarisés de spin, effet de filtre à spin, vanne de spin, électrons secondaires, cathodoluminescence, jonction Schottky, contacts métal / isolant / semi-conducteur, puits quantiques, couche mince magnétique.

Abstract

The objective of this thesis work is to experimentally investigate the phenomena of the spin-dependent transport of hot electrons at room temperature into ferromagnetic metal (Fe or Co) / semiconductor (GaAs) Schottky junctions. In practice, a spin-polarized electron beam generated by optical orientation is injected into the two-terminal structure with energies varying from 10 to 3 keV above the Fermi level. The transmitted current shows a spin asymmetry, which depends on the relative orientation between the iron magnetization and the incident spin direction. In this PhD work, we have pursued two experimental approaches, one optical and the other electrical for detecting the transmitted current through the junction above the Fermi level, both exploiting the multiplication of electrons due to the generation of secondary electrons inside the metal layer. The *electrical* measurement requires of working with structures having a very high dynamic resistance of junction (typically a few MΩ). The spin-dependent asymmetries are studied in samples characterized by different thicknesses of the oxide layer between magnetic metal layer and GaAs. We observe different transport regimes associated with the electron transmission at different interfaces. The *optical* measurement of the transmitted current is based on the radiative recombination of the injected electrons with the holes through the *p*-type semiconductor band gap. For this purpose a new structure including InGaAs quantum wells and one single Fe layer has been grown. Spin-polarized electrons injected into such a structure produce an asymmetry in the recombination light intensity. The variation of the luminescence asymmetry is studied relative the energy of the incident electrons. The optical detection offers the advantage of being less sensitive to the junction resistance.

Key words: spin-dependent electron transmission, spin-filter effect, spin-valve effect, Schottky junction, metal / oxide / semiconductor contacts, secondary electrons, quantum wells, photoluminescence.

Acknowledgement

After four years of work in PMC laboratory, I finally succeeded in changing myself into a PhD in Physics. When I recall all the memories during this period, I should say, it wasn't easy! Frequently, I have felt tired, helpless, and disappointed. However, the work was pushed to the end with one achievement after another, and life changed for the better after each small success. Meanwhile, lots of kind people around me have given me a hand. Without their help, I would never have made it!

First of all, I would like to express my sincere appreciation and gratitude to my supervisor, Yves Lassailly, and my co-supervisor, Jacques Peretti. In fact, I think that I can never say enough "Thanks" to them. They gave me great guidance and encouragement not only for work but also for life. They really cared about my future career and all the difficulties I had as a foreigner in France. For all of this, they have gained my complete respect and confidence!

Afterwards, the committee of my PhD defense.

- I appreciate the referees for my thesis, André Thiaville and Wolfgang Weber, for their precious time for reviewing my thesis, making lots of important comments and corrections, editing the reports in detail, and taking part in my defense.
- I am deeply grateful to Michel Hehn, the examiner for my defense and one of the most important cooperators, with whom I have had helpful discussions and suggestions throughout my PhD. At the same time, many thanks to his research team. Under his leadship, they have brought me most of the main samples for our study, which form the first part of my PhD work. They are our hand-in-hand partners on the way to success!
- The same appreciation is sent to Jean-Eric Wegrowe, the president of my defense committee, for his kind and helpful discussions and suggestions, and the nice management of my defense.

Then, great thanks are given to my colleagues and former PhD students in the EPS group.

- George Lampel, the first man with whom I worked in PMC, was always working with me and gently guided me to learn how to generate scientific ideas and to be a physicist.

- Oleg Tereshchenko (researcher at A. V. Rzhanov Institute of Semiconductor Physics, Novosibirsk State University, Russia) brought me lots of excellent ideas and discussions about science, and the samples he made yielded new results which form the content of the second part of my thesis.
- Alistair Rowe, a really scientific and technical guy, worked with me for several months but always gave me "little but important" suggestions on key points.
- Daniel Paget, an excellent physicist, brought me to the lab and arranged all the affairs to help me to settle down in France four years ago. And then, he was paying attention to my subject in these years and indeed gave me many helpful and precious discussions and suggestions.
- Driss Lamine, Frédéric Roux, and Nicholas Rougemaille, they helped me with the initial knowledge of my subject and improved my understanding of the science when they were still in the lab, and they kept doing me favors both on science and in general even after they left.
- Filippo Fabbri and Vu Duong, they were always with me in the lab. I can never forget the very relaxed time with them, and the moment that one of them passed me a sandwich when I was in the dark room in the weekends and said to me "have a break now!"

Many thanks go to the whole service staff.

- Eve Brunswic (personnel and contracts manager), who is one of the most important people here, made extreme efforts to deal with my administrative affairs (I cannot imagine how difficult things would be without her function).
- André Wack and Dominique Clément (mechanists), Didier Lenoir and Thomas Dachy (electronic engineers), Julien Monguillon and Denis Coupvent-Desgraviers (computer engineers), their hard working did the solid support for my subject. I'm sorry that I really asked them for quite a lot of work.
- Patrice Déaroque (technical assistant), Anne-Marie Hernecq (general secretary), and Sébastien Maron, and all the other present and former service staff members, thanks for their kindly favors.

I am heartily thankful to Phillippe Allongue for having shared the office and enjoyed the peaceful and pleasant time with him. Special thanks to Magali Florens for all her help during my PhD: correction of my French, important information on searching for job opportunities, and bringing me the simplicities at every aspect in the life.

Great thanks to François Ozanam, the director of the lab. I can never forget the moment four and half years ago when I received from him the first and the only answer after having sent several tens of applications to the PhD position. Followed his instruction, I got to the connections with the lab and finally came here and joined the PMC family. Then I still received his continuous help and advices throughout my PhD.

Thanks the same to Michel Rosso and Andrey Lemaréchal, the former director and the secretary of the Ecole Doctoral, for their kindly help on the administrative affairs.

I thank all the permanent researchers in the other groups at lab for all the valuable advices for my study. Especially, to Fouad Maroun, Isabelle Maurin, Marcel Filoche, Mathis Plapp, Jean-Pierre Boilot, Jean-Noël Chazalviel, Robert Cortes, Anne-Chantal Gouget-Laemmel, and Ionel Solomon, for all the helpful advices and suggestions with humors in the day-to-day meetings, and these brought me the fresh air every day.

I thank all the former and present internees, PhD students, and Postdocs in the lab, especially to Oscar de Abril, Duc Vu Anh, Houria Chemmi, Alexis Damian, Sunita Darbe, Blaise Fleury, Gabriel Freiman, Mei Han, Lili Lu, Yiwen Ma, Subimal Majee, Kei Nishikawa, Binh Thanh Nguyen, Le Thang Long Nguyen, Rafael Novak, Nayely Pannier, Emmanuel Perez, Morgane Presle, Grégory Savidand, Vincent Tariel, Charlotte Vichery, for all the help and the delighted time spending with them. Particular thanks to Aurélie Foucquier, Ania Baïri, Larbi Touahir, Hugo Jurca, Sébastien Nguyen, for all the aids on the life, and to Daniel Alves Dalla Corte, Jason Milne, Viacheslav Kubytskyi, Matteo Nicoli, for everyday relaxation and excellent free time with them.

I am sincerely grateful to Qiang Chen who has been my supervisor in the Master work, Rong Chen, Xiaoliang Fan, Cong Gao, Sheng Gao, Bo Gu, Hoa Nguyen, Eugénie Lafon, Ye

Liang, Xin Lin, Yan Ma, Chenqi Mou, Sachiko Nishikawa, Ryna Lam Pech, Yuan Shen, Fei Sun, Benoit Toulmé, Dongming Wang, Lina Wang, Xiaomin Wang, Han Xiao, Rong Xiao, Xi Xu, Feng Yang, Mengyin Yu, Juliana Zarpellon, Ting Zhao, Xin Zhou, and all my friends in France and all over the world for sharing my happiness and helping me when I was in difficulty during these years.

The most important and special thanks to my wife Wei Niu and our parents. Their constant support, encouragement, and never fading love did let me have powerful motivations to go further and arrive at the success!

In the end, what can be concluded? A PhD is a title awarded to one person, but the work is not a cake that can be accomplished by the PhD himself. It is a prize to a group of people! For me, it is here, Laboratoire de Physique de la Matière Condensée in Palaiseau.

Contents

Introduction

In the early 1980's, it was shown that inelastic electron scattering in ferromagnetic metals at energies well above the Fermi level depends on the orientation of the electron spin with respect to the magnetization [Unguris82, Kisker82, Hopster82, Penn85a]. This dependence is a direct consequence of the exchange interaction which induces a spin asymmetry in the electron density of states in the vicinity of the Fermi level. Different numbers of available empty states for the two directions of spin result in different values of the inelastic mean free path. Thus electrons which cross a magnetic thin film are spin-filtered. This effect was demonstrated in ballistic electron transmission experiments and the spin dependence of the electron inelastic mean free path was measured over an energy range which extends up to several tens of eV. [Pappas91, Getzlaff93, Schönhense93, Lassailly94, Vescovo95, Gröbli95, Drouhin96, Oberli98, Cacho02] This spin selectivity of ultrathin magnetic films has been exploited in magnetic domain imaging and in several model spintronic devices. [Monsma95, Filipe98, vanDijken03, Jiang04, Kinno97, Rippard99, Rippard00, Heer04, Kaidatzis08] Such devices, based on metal semiconductor junctions, exhibit high spin selectivity but suffer from high current attenuation. Attenuation can be compensated by increasing injection energy in order to benefit from secondary electron multiplication. [Filipe98, Rougemaille08] However, although the spin-dependent scattering is qualitatively well understood in the case of ballistic electron transmission, the situation is not so clear when dealing with inelastically scattered electrons.

The purpose of this thesis is to study the spin-dependent transport of electrons across ferromagnetic metal / semiconductor junctions as a function of the injection energy in a range which extends from 5 to 3000 eV *above the Fermi level*. Indeed, in high energy range the transport is dominated by electron-electron scattering which gives rise to the excitation of a secondary electron cascade. In this framework, several questions rise up like:

1) How does spin-polarized electron transmission through the junction depend on the electron injection energy and on the metal / semiconductor barrier shape?

2) How to describe the energy and momentum relaxation which results in the formation of the secondary electron distribution?

3) Which spin transport processes have to be considered: relaxation, precession, filtering, dilution / exchange?

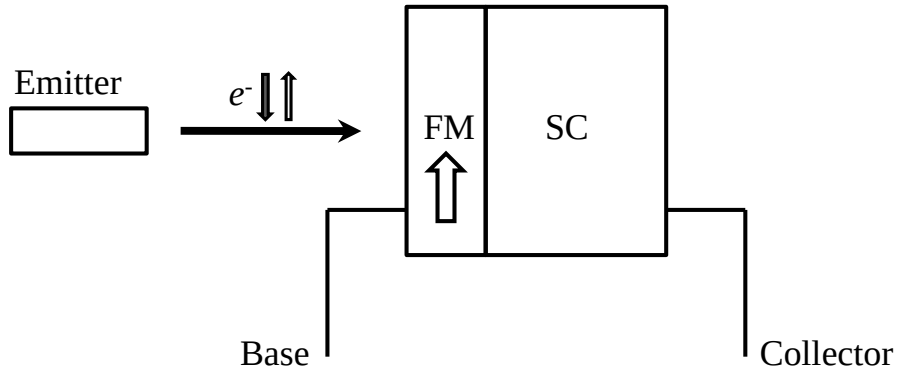

Figure A.1: Scheme of the three-terminal hybrid device. The emitter provides spin-polarized free electrons. The electrons are injected into the ferromagnetic metal (FM) / semiconductor (SC) junction. Base (metal) and collector (semiconductor) currents are separately detected.

In order to address these issues, we will have to answer the preliminary question of how to detect spin-dependent transport properties in a hybrid structure which combines ferromagnetic and semiconductor materials. The general scheme for such experiments is the one of a three terminal transistor-like device with a ferromagnetic metal base and a semiconductor collector. Then different configurations can be envisaged which mainly differ by the emitter. Our approach, schematized in Fig.I.1, is based on the use of a spin-polarized free electron source. The emitter is thus spatially separated from the base / collector junction, which offers the main advantage of controlling the spin polarization of the incident electron beam and that of accurately tuning the injection energy. The spin-polarized electron source is a *p*-doped GaAs

photocathode activated in negative electron affinity. When excited in optical pumping conditions with circularly polarized near-bandgap light it produces an electron beam of polarization $P_0 = \pm 25$ %. The sign of P_0 can be simply reversed by reversing the helicity of the excitation light. The base, which contains one (or two) ultrathin ferromagnetic layer(s), acts as a spin filter by favoring the transmission of one electron spin state. It is required to exhibit a square hysteresis loop to achieve electron transmission in a persistent magnetic state. It is the relative orientation of the magnetization to the incident spin polarization, which determines the transmission of the base. Electrons travelling through the junction are detected at the collector as a transmitted current, whose magnitude depends on the magnetic state of the base. The other part of electrons, which are absorbed in the spin filter layer, contribute to the base current. Such transport measurements rely on the ability of independently measuring the base and the collector currents. This can only be achieved for junctions of very high impedance, provided by a Schottky-like barrier at the interface between the metal base and the semiconductor collector which exhibits a strong rectifying character. To work out a ferromagnetic metal / semiconductor junction with good rectifying behavior is a highly nontrivial task in practice. The main limitation comes from the fact that in a Schottky junction made of an abrupt metal / semiconductor contact, the interdiffusion between the metal and the semiconductor cannot be fully avoided. To overcome this problem we have explored two different approaches. One is to introduce a very thin oxide interfacial layer between the metal and the semiconductor which is known to improve the junction barrier and to prevent against the interdiffusion. The main difficulty is that the oxide layer has to be thin enough to let pass the electron without applying a bias. The other approach is to give up the electrical measurement of transmitted current and to develop instead an optical detection technique insensitive to the electrical properties of the junction. To do so we will exploit the light emitted from the recombination of the transmitted electrons into the semiconductor collector.

In Chapter I, we will start by reviewing the state of art of the spin-dependent transmission

experiments with emphasis on the energy range of electrons implicated in the transport.

In Chapter 2, we present the first approach, where we study electron transmission through Metal / Insulator / Semiconductor junctions. Several structures are considered which differ one from the other by the composition of the metal layer, the thickness and bandgap of the oxide and finally by the semiconductor collector. In most samples we could not detect a reliable electron transmission signal at low injection energy (typically below few hundreds of eV) while, at high injection energy, we have obtained electron transmission larger than unity (because of secondary electron multiplication) and spin filtering effects. Finally, for samples containing two magnetic layers, no spin valve effect has been detected.

In Chapter 3, we describe the cathodoluminescence experiment that we have developed to exploit the radiative recombination of electron in the semiconductor collector in order to detect the transmission through the junction. For this purpose, specific semiconductor collectors have been grown with quantum wells to favor electron recombination close to the metal / semiconductor interface. We present the first results that we have obtained on the optical detection of spin-polarized electron transmission through ferromagnetic metal / semiconductor junctions.

In conclusion, we discuss the main limitations and advantages of the optical detection method and we present some perspectives for future experiments.

Chapter I
Spin-dependent effects in magnetic thin films

Transport of electrons injected at energies well above the Fermi level into empty bands is a complex problem. This chapter is intended to present and discuss experimental results that are relevant to the understanding of spin-dependent transmission experiments when inelastic electron scattering dominates the transport properties.

The present thesis work is related to the wide field of spintronics. Most of the approaches developed in this field concern the transport properties at the Fermi level E_F. The giant magnetoresistance (GMR) effect constitutes the most well-known paradigm. The approach pursued along this work deals with the transport of spin-polarized "hot" electrons having energies greater than E_F. It makes use of tools at the frontier between electron transport and electron spectroscopy techniques. We will briefly review the state of art in this domain, before describing the objectives of our work.

I.1 "Transport" at high energy in metallic thin films

The first energy range to consider is the low energy range of a few eV above E_F (where the electron transport through thin films is mainly ballistic). This situation is met in tunneling injection [Alvarado92, LaBella01, Vu11] and BEEM experiments [Rippard99, Kaidatzis08]. Electron transport above E_F in the empty bands is ensured by thereafter called hot electrons, which have the kinetic energy greater than E_F and interact with the Fermi sea. Hot electron transport can be described in term of mean free path as being the characteristic attenuation length, which is generally of the same order of magnitude as the thickness of metal layers.

Transport at higher energy range (several tens of eV) is far from being quantitatively well understood. Electrons crossing the sample interact with the conduction electrons, leading to the production of secondary electrons. The secondary emission is a cascade process of excitation from the Fermi sea combined with elastic and inelastic scatterings of the electron cascade. Thus a complete treatment of the secondary emission requires the knowledge of the electronic transition probabilities in the sample, of the scattering cross sections for elastic and inelastic electrons. So far, there is no single theory, which takes into account all of these features. However, previous results obtained in our group by the electron injection of energies up to 2 keV [Rougemaille08] will help us compare our spin dependence measurements of

electrons crossing ferromagnetic films.

Let us now give an overview of results, which are pertinent to the understanding of our work.

I.1.1 Low energy transport above E_F in thin ferromagnetic films

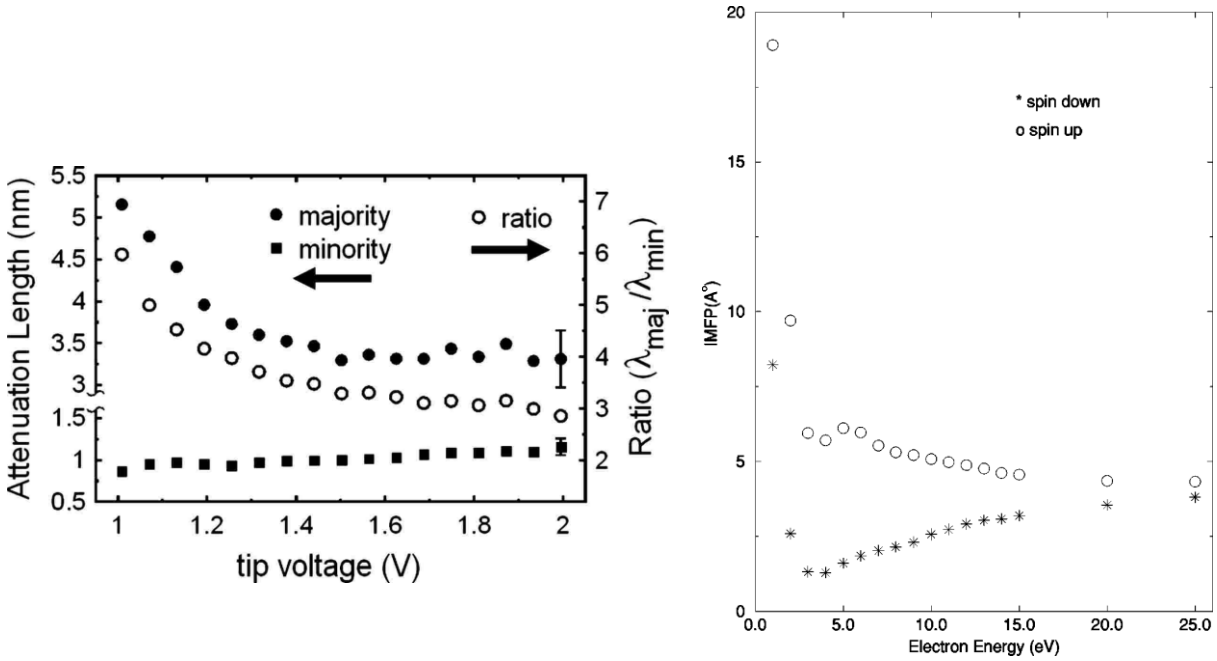

(a) (b)

Figure 1.1: Hot electron transport. (a) Hot electron attenuation length for majority-spin and minority-spin electrons in Co in the energy range of 1 to 2 eV above the Fermi level, deduced from BEEM experiments [from Kaidatzis08]. Right: Inelastic mean free path calculated for majority-spin and minority-spin electrons in Fe at low energy [Hong00] (sp contributions are included). It evidences a large spin asymmetry in the mean free path ($\lambda^+ >> \lambda^-$) within about 10 eV from the vacuum level (electron energy equals zero). Its origin comes from the very strong spin-flip exchange scattering.

The key idea, common to all spin-injection experiments exploits the consequence of the imbalance of densities of the electronic states at E_F in ferromagnetic metals: the inelastic

mean free path of majority-spin electrons is larger than that of minority-spin electrons in an energy range up to 50 eV above E_F [Penn85b, Pappas91, Grobli95, Oberli98, Weber01]. In other words the scattering rate for minority-spin electrons injected into the ferromagnetic empty band is enhanced due to the excess of minority spin holes. (cf. Figure 1.1)

This asymmetrical transport of spin-polarized electrons gives rise to electron spin filtering in thin ferromagnetic films. The spin filtering techniques may be loosely classified into three groups.

1) **Spin filter**

Figure 1.2-a illustrates how to operate a spin filter. When an electron beam of spin polarization P_0 strikes an ultrathin ferromagnetic sample the transmitted current depends on the relative orientation of the incident spin polarization with respect to the film saturated magnetization.

One of the properties of the spin filter is that its spin selectivity depends on the energy of hot electrons traveling through the ferromagnetic film. The spin filter is characterized by the following experimental quantities:

- The asymmetry A of the transmitted current $A = (I^+ - I^-) / (I^+ + I^-)$, I^+ (I^-) being the transmitted current for $+P_0$ ($-P_0$) respectively;

- The spin-dependent transmission $\Delta T = (I^+ - I^-) / I_0$, I_0 being the incident current;

- And by analogy to spin polarimetry, its capability of spin discrimination, the *so-called* Sherman function S. It is the polarization acquired by an unpolarized beam when passed through the spin filter.

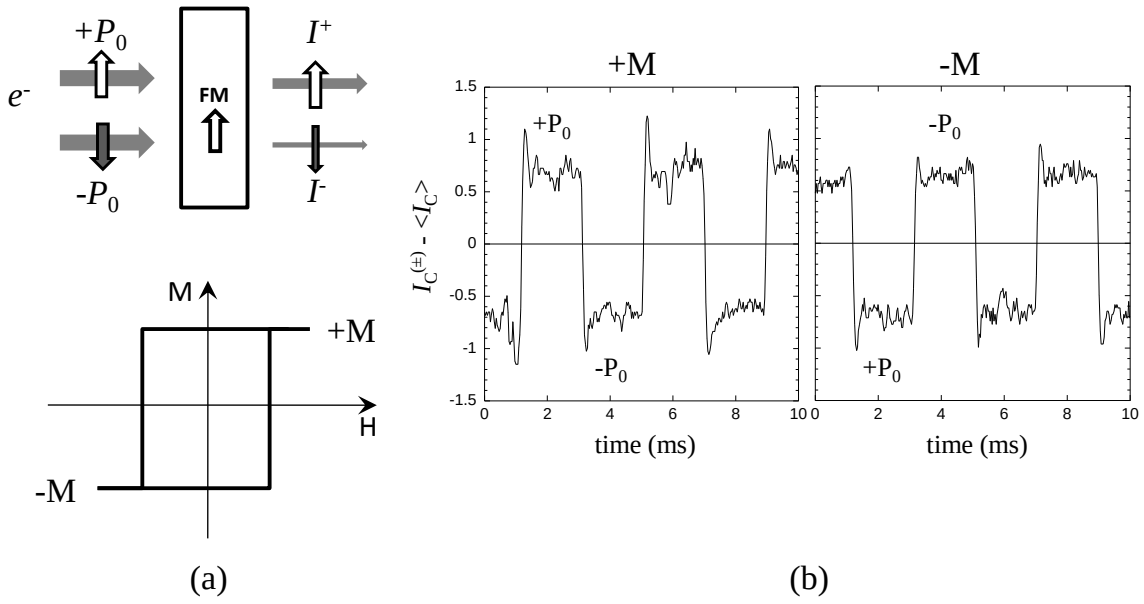

Figure 1.2: Working principle of spin filter in transmission geometry. (a) The ultrathin magnetic film preferentially transmits electron whose incident spin direction is parallel to the magnetization orientation. One of the prerequisites for having a spin filter relies on the square hysteresis loop with two saturated magnetized states +M and –M. Thus electron transport occurs under zero applied magnetic field. Reversing the saturated magnetization from +M to –M is equivalent to switching the incident electron polarization from $+P_0$ to $-P_0$. For a given magnetization an asymmetry between the transmitted currents I^+ and I^- is measured. (b) Experimental results showing the spin-filter effect in the Fe / GaAs junction. Variation of the transmitted current I_C as a function of time, when modulating periodically the polarization of the incident electrons between $+P_0$ and $-P_0$. When flipping the magnetization the spin filtering effect is reversed. $\langle I_C \rangle$ refers to the spin-independent part of the transmitted current I_C. The current scale is in nA.[Rougemaille03]

Typically the structure Au / Co / Au (1 nm thick Co layer) has a transmission of 4×10^{-4}, a spin-dependent transmission $\Delta T = 6 \times 10^{-5}$ and a current asymmetry $A = 8.5\ \%$ for an incident electron polarization of 25 %. The Sherman function value of such a spin filter is 0.34 for low injection energy, less than 5 eV. It can be shown that the transmission asymmetry verifies the equation $A = P_0 S$. It means that to measure a spin-dependent asymmetry an *initial spin polarization* P_0 is required in conjunction with the spin-filter layer. This is the working

condition of a spin filter.

Two experimental configurations have been explored for measuring spin filter effect: either the transmission takes place through a freestanding foil, such as Au / Co / Au of total thickness of 21 nm [Lassailly94, Oberli98] or through a compact structure, where the ferromagnetic layer is deposited on a bulk semiconductor, the latter collecting the transmitted current [Filippe98, Rougemaille03]. It is the latter configuration that we will use in the thesis.

2) **Spin valve: polarizer-analyzer experiments** [Mousma95, Jansen01, Rippard00, Cacho02, VanDijken03]

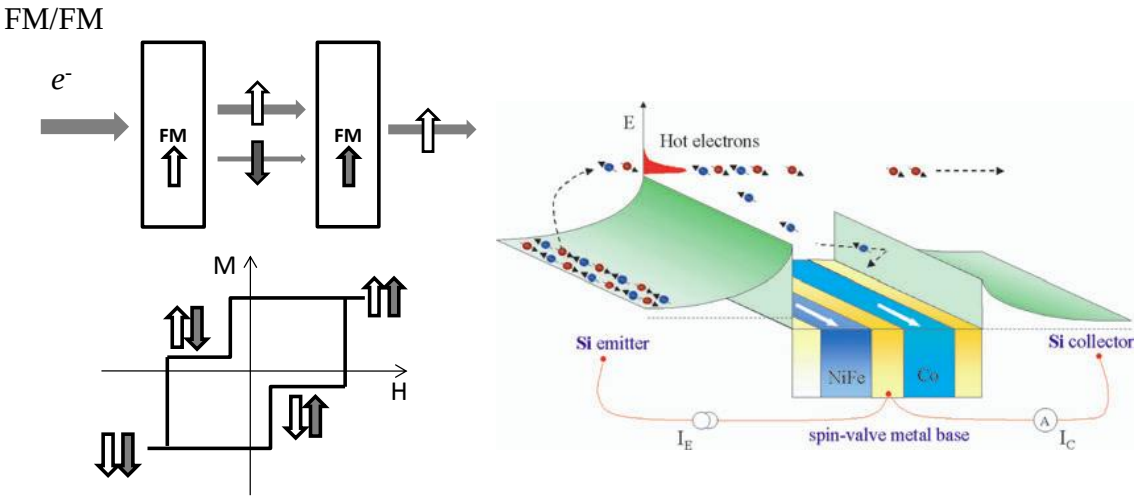

(a) (b)

Figure 1.3: Working principle of spin-valve device. (a) An unpolarized electron beam is transmitted through two uncoupled ferromagnetic layers separated by a nonmagnetic layer. The two magnetic layers act as polarizer and analyzer of electron spins, such that the relative orientation of the magnetization of the two layers determines the transmission of the base. (b): Schematic energy diagram of a spin valve transistor. Hot electrons are injected above the Fermi level. Hereby the incident electron energy is determined by the height of the Schottky barrier between the semiconductor emitter source and the metal base [from Jansen03].

The spin filtering effect can be exploited for achieving the optical equivalence of the polarizer-analyzer combination. Two ferromagnetic layers are required (Figure 1.3), the first one selecting a population of spin-polarized electrons, the second one detecting the projected spin component along the magnetization direction. The resulting salient feature is that the collector current depends on the magnetic state of the spin-valve layers, i.e. the base. Examples of spin-valve device include the magnetic tunneling transistor and the spin-valve transistor. Both devices are junctions sensible to electronic properties of interface, the transmission probability being determined by energy and momentum constraints imposed by the band structure difference between the semiconductor and the metal interface. Such junctions operate in low energy range from 0.8 to 2 eV, higher voltages resulting in a breakdown of the junction. To explore a higher energy range the electron source has to be decoupled from the spin-valve structure. It is the strategy that we have followed during this work. It also offers the advantage of optically controlling the incident spin polarization and tuning the energy of incident electrons up to 3 keV.

3) Spin-precession of the polarization

When the spin-polarization vector of the incident electron beam is perpendicular to the magnetization of the ferromagnetic layer, then it rotates into the direction of the magnetization and simultaneously precesses around it. The angle of rotation depends on the spin asymmetry *A* [Oberli98]. The rotation around the magnetization is the optical analog of the linear magneto-optics Faraday effect, the light propagation vector being oriented along the magnetization vector. Precession of electron spin can also be generated by the reflection at ferromagnetic surface [Weber02], by the injection of spin-polarized beam into non-magnetic materials but under a continuous magnetic field [Huang07]. Typically electron energy involved in spin-precession experiments is in the range of a few eV.

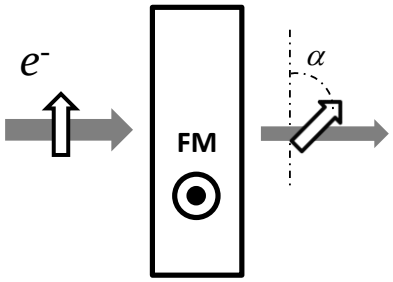

Figure 1.4: Spin-precession effect. When electrons are injected into the ferromagnetic layer with the spin direction normal to the magnetization, the electron spin will rotate of the angle α into the direction of the magnetization of the layer and at the same time process around it.

I.1.2 High energy transport: the secondary electrons at play

Electron transmission in spin-valve structure up to 100 eV of injection energy reveals a linear increase versus the injection energy due to the secondary electron multiplication [Cacho02]. As soon as electrons enter the metal cap layer prior the magnetic filter, the secondary electron process induces a dilution of the initial spin polarization. Consequently the polarization of secondary electrons does not depend on the polarization of the injected electrons. At very high injection energy up to 3 keV, we can only predict an increase in the electron mean free path by referring to the well-known $E^{1/2}$ variation of the electron mean free path versus electron energy. The ballistic transport is no longer valid in all sample thickness and must be replaced by the spatial evolution of a distribution composed of primary electrons, which keep the memory of the initial spin polarization, and secondary electrons. Varying the incident energy amounts to broad the electron distribution reaching the interface metal / semiconductor. The electron energy distribution of secondary electrons is characterized by a mean energy ε_M, which corresponds to the energy of electron travelling within the interface and an amplitude given by the secondary multiplication factor. The collected current corresponds to the upper energy part of the electron distribution, the lower

part being successively energy filtered when crossing interface barriers. The spin-dependent part of transmission in the spin filter can be included by considering two electron distributions for the primary electrons, each being associated with spin-dependent mean free paths λ^+ and λ^-. Figure 1.5 gives a pictorial representation of the different transport mechanisms involved in the spin filter.

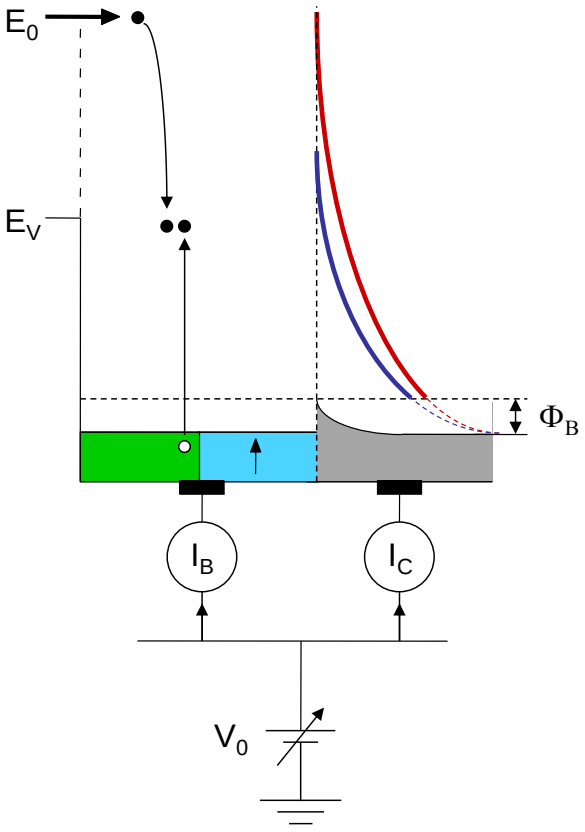

Figure 1.5: Schematic layout showing the transport in the structure metal / semiconductor based on the electron-electron interaction, each scattering yielding two electrons. Φ_B is the Schottky height, E_V the vacuum level and E_0 the energy of incident electrons. The incoming electron relaxes its energy in the metal base by generating a cascade of secondary electrons. The base current I_B corresponds to electrons, which have not enough energy to surmount the barrier Φ_B. Electrons which pass the barrier form the collector current I_C in the semiconductor. The spin filter effect results in two different energy distributions of the transmitted electrons (red and blue curves), whose low energy part is cut off by the barrier Φ_B. The current I_C is actually the integral in energy of the energy distribution. The potential V_0 applied on the two terminals of the junction determines the injection energy E_0.

Increasing the incident energy E_0 amounts to a boost in the multiplication of secondary electrons, and therefore to a broadening of the electron distribution resulting from the subsequent cascade. The unknown quantity, which is not directly accessible from our measurement, is the mean energy ε_M of the electron distribution within the sample. Its variation with the injection energy E_0 can be obtained by self-consistently solving the equation which yields the total transmission T through the junction:

$$T = \frac{E_0}{\varepsilon_M}\left[\alpha_{SC}\exp\left(-\frac{\Phi_{SC}}{\varepsilon_M}\right) + \alpha_{Ox}\exp\left(-\frac{\Phi_{Ox}}{\varepsilon_M}\right)\right],$$

where the value of α_{SC} (α_{Ox}) the collection efficiency in the semiconductor (the oxide layer), and Φ_{SC} (Φ_{Ox}) the semiconductor band bending barrier (the oxide layer barrier height) are known [Rougemaille08]. The exponential function reproduces the accumulation of secondary electrons due to the electron cascade. Figure 1.6 shows the variation of ε_M versus E_0 deduced from the experimental measurement of the transmission through the Fe / Oxide / GaAs sample.

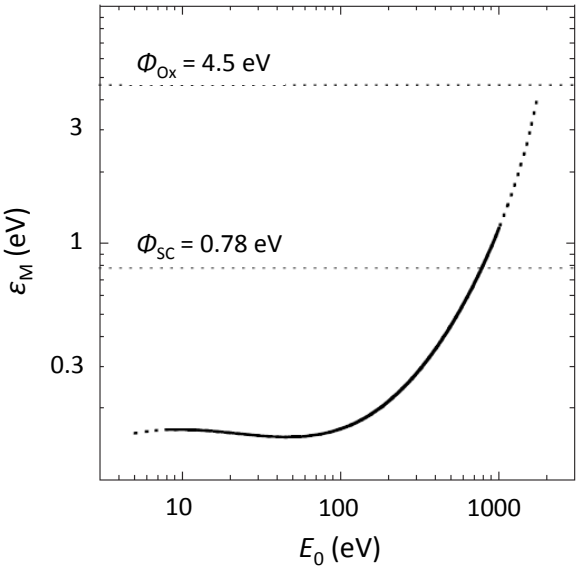

Figure 1.6 [Rougemaiile08]: Calculated variation of the electron mean energy ε_M, which describes the electron distribution width at the metal / Oxide interface in the structure Fe (3.5 nm) / Oxide / GaAs as a function of the injection energy E_0. Horizontal dotted lines correspond to the two barrier heights Φ_{Ox} and Φ_{SC}.

I.2 Our experimental strategy

We briefly list the main features, which constitute the backbone of our experimental work. They will be thoroughly described in the next chapters.

I.2.1 A three-terminal device or the importance of having an abrupt, high-quality Schottky barrier

The metal base, which includes the spin-filter layer, is grown on the semiconductor substrate, which is used as a collector. The spin injection is achieved by an electron source separated from the base-collector electrodes by vacuum. The two electrodes are connected to the same potential, which defines the injection energy. The potential barrier formed at the metal-semiconductor interface has to fulfill two objectives. First, as previously mentioned, it ensures the selectivity in energy of the transmitted electrons. Electrons of energy below the potential barrier are collected in the base layer. Second, the barrier provides a junction resistance, whose value should be high enough for measuring *independently* the base current and the collector current under zero applied voltage to the junction. We will have to find out how to accurately measure the junction resistance.

I.2.2 What type of metal-semiconductor junctions?

Effort has been concentrated in our group on the growth of Fe on GaAs [Filippe98] to form a Fe / GaAs Schottky diode. The electrical properties of such samples are given by quality of the metal / semiconductor interface. Indeed the junction must block electrons of energies below the barrier. Pin holes and defects at the interface give rise to leak currents, which can compensate the current passing over the barrier. Also our working conditions

require using samples of quite large area (typically 7×7 mm^2). To overcome these obstacles, the approach is to form a *Schottky-like* junction. In this type of structure, a very thin oxide layer of different thicknesses (typically from 1 to 3 nm) is grown at the interface between the metal and the semiconductor.

In a first step we will study the archetype junction Pd / Fe / oxide / n^+ - GaAs, whose spin-polarized-electron transport has been experimentally and theoretically analyzed [Rougemaille08, Lamine07]. The structure contains a single iron layer grown onto a 2 nm thick oxide layer. Then in a second step transmission through junctions having different thicknesses of oxide will be compared with transmission through the Pd / Fe / oxide / n^+ - GaAs. These junctions are fabricated by our collaborators of the group "Nanomagnetism and Spin-Electronics", led by Michel Hehn, at the Laboratory of Material Physics of Nancy University.

I.2.3 What type of detection for the transmitted electrons?

As early described in the chapter, the principle of all injection experiments is based on the electrical measurement of currents transmitted through the sample. The price to pay is the necessity of working with a high impedance sample. Indeed such a measurement amounts to detecting a weak current flowing through finite impedance terminals. In particular it remains to determine the threshold of detection for the transmitted currents. Another alternative to the current measurement is the optical detection of the transmitted current. Based on the formal analogy between polarizing and analyzing spin filter, one might expect that GaAs is not only a source but also a detector of spin polarization. This means to carry out a cathodoluminescence experiment, in which the transmitted electrons recombine with holes across the semiconductor band gap thereby by emitting light. Moreover spin-polarized electrons should produce circularly polarized luminescence. The oxide barrier presented in the previous samples is now

replaced by the energy gap of semiconductor. A new junction comprising the electron-photon converter part has been elaborated by Oleg Tereschenko of the Institute of Semiconductor Physics in Novosibirsk. The main advantage of the optical detection is that the constraint of having a rectifying behavior is now avoided. A new experimental setup will be developed to meet the need of such luminescence detection.

Chapter II

Electrical detection of spin-filter effect in ferromagnetic metal / semiconductor junctions

---

The existence and the properties of spin-filtering in ferromagnetic metal / semiconductor rectifying junctions can be measured by injecting spin-polarized electrons into empty bands of the ferromagnetic metal. In this chapter we review the experimental configuration to achieve such a transport measurement. Then we present the transmission results obtained from junctions having one or two ferromagnetic layers. We also show the effect of an interfacial oxide barrier introduced between the metal and the semiconductor.

II.1 The objectives

Our experimental approach relies on injecting spin-polarized electrons into a ferromagnetic metal / oxide / semiconductor (hereafter referred as MIS) junction, where the oxide layer behaves as a tunnel potential barrier for electrons having an energy less than the barrier height ($E < \Phi_B + h$, Figure 2.1).

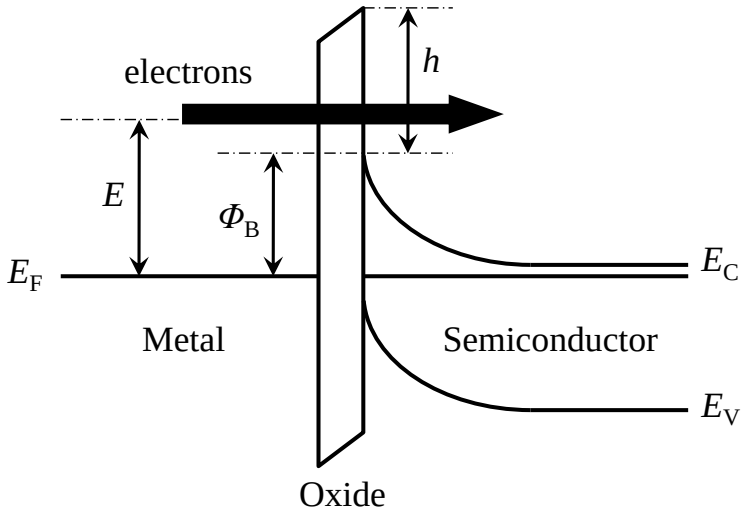

Figure 2.1: Schematic energy diagram of electrical injection and detection at zero bias in MIS junction with n-type semiconductor substrate. Φ_B is the Schottky barrier height (i.e. the barrier height due to the semiconductor band bending). The main issue discussed in this chapter revolves around the oxide thickness, which affects the I-V characteristics and the results of the transmission experiments. E is the injection energy referred to the Fermi level E_F.

The junction has to fulfill the following criteria.

The electrical properties. When collecting current on a metal electrode in ultra-high vacuum environment, the current flows through an infinite impedance, which is the impedance of the vacuum / electrode barrier. This is the ideal configuration to measure small currents, when, for instance, performing direct electron transmission through a freestanding sample [Cacho00]. However, measuring the current crossing a junction turns out to be limited

by the intrinsic resistance of the junction, as it will be explained in § III.3.4. Therefore the equivalent resistance of the junction has to be as large as possible. In principle, when injecting high energy electrons into a junction, the rectifying character of the metal / semiconductor contact should provide high enough junction impedance to allow independent measurement of the currents flowing in the metal and in the semiconductor terminals. In practice, this is often not the case. Then, inserting an oxide layer (which introduces a barrier for both charge transport and atoms interdiffusion) between the ferromagnetic metal and the semiconductor provides a means of controlling the junction resistance. The oxide layer must be thin enough to behave as a tunnel barrier (Figure 2.1).

The magnetic properties. In our experimental geometry, the samples must contain ferromagnetic layers with in-plane magnetic anisotropy so that the spin polarization of the incident electron beam is parallel to the sample surface. We recall that our concern is to measure the transmitted current according to the relative orientation between the spin polarization and the saturated magnetization of the ferromagnetic layers. The number of ferromagnetic layers allows one to investigate either the spin-filter effect (one ferromagnetic layer) or the spin-valve effect (two ferromagnetic layers). In the case of the spin-valve sample the coercivity of each ferromagnetic layer should be quite distinct in order to reverse the magnetization of one layer without affecting the second one.

Thickness consideration. Concerning the interfacial oxide layer, it must be thin enough (in the range of 1~3 nm) to differ from the genuine metal / insulator / semiconductor capacitor. Concerning the metal layer thickness, as shown by the previous transmission experiments [Rougemaille03, Lamine07, Rougemaille08], the overall metal multilayer film has to be less than 20 nm thick, otherwise the transmission factor becomes too weak to give a detectable transmitted current.

II.2 Nature of junctions

II.2.1 Sample structures

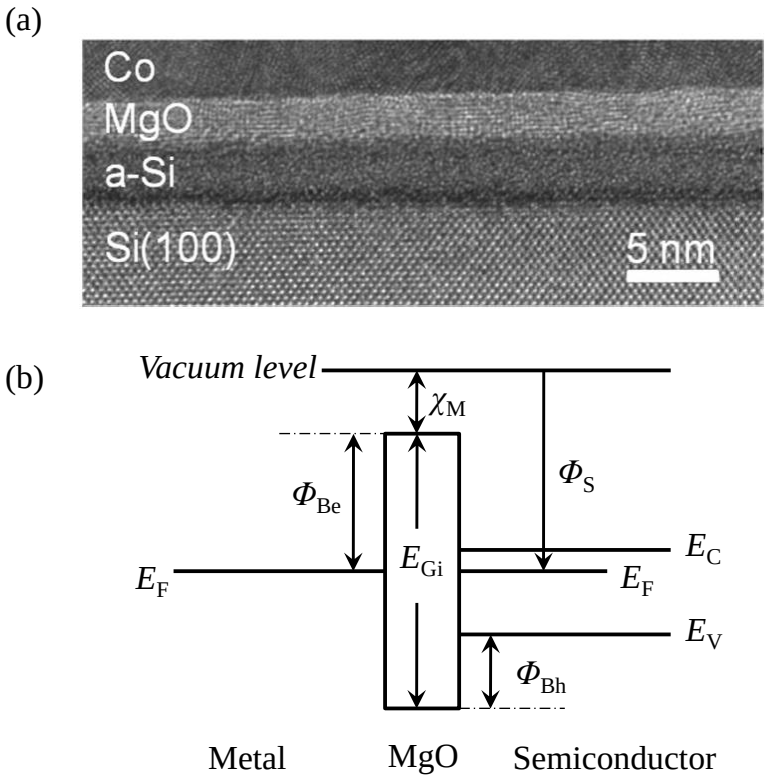

Figure 2.2: Schematic diagram of MgO interface in the junction Co / MgO / Si. (a) Zoom of the interface Si(100) / MgO(100) showing a highly textured MgO layer of 2 nm and a sharp and atomically flat interface [Bernos10]. An amorphous Si layer is between the Si substrate and the MgO layer. (b) Energy-band diagram of an ideal metal / MgO / semiconductor junction (equal metal and Si work function Φ_S). The gap of MgO E_{Gi} = 7.6 eV, the electron barrier height Φ_{Be} = 3.7 eV, the hole barrier height Φ_{Bh} = 3.0 eV, the energy gap of Si is 1.1 eV, and the electron affinity of MgO χ_M = 1.5 eV. [Parkin04, Kurt10]

As previously stated, an oxide layer is grown on the semiconductor substrate prior to the deposition of the ferromagnetic layer. We have used three types of oxide layers: magnesium oxide (MgO), aluminum oxide (Al_2O_3) and gallium oxide (Ga_2O_3) generated at room temperature by UVOCS ("Ultra-Violet Ozone Cleaning System"). However, the samples

containing a 2 nm thick aluminum oxide barrier show no photogenerated current under the light illumination (the main reason for that will be further described). In the rest of the thesis we will confine ourselves to the junctions with the two other types of oxides. All the semiconductors substrates are *n*-doped, so the majority carriers are electrons.

1. The junction Pd (5 nm) / Fe (4 nm) / Uvocs (10 Å) / *n*-GaAs, hereafter referred to as GaAs_1, which is the "canonical" junction, has been successfully studied in our group [Rougemaille03, Lamine07, Rougemaille08]. It will be used as the reference sample to give evidence to the effects due to the nature of barrier in the transmission experiments.

2. The junction Pt (3 nm) / Co (5 nm) / MgO (100) (2 nm) / *n*-Si (100), hereafter referred as MgO_1, to study the spin-dependent electron transport in Si. The choice of the MgO barrier is dictated by a barrier height higher (3.7 eV for an ideal MgO tunnel barrier, assuming that the Fermi level is pinned mid-gap, i.e. in the absence of fixed oxide charges, see Fig.2.2-b) than the amorphous Al_2O_3 barrier of 2.6 eV and by a higher magnetoresistance in the magnetic tunnel junctions. According to the deposition process worked out by Bernos *et al* in Nancy [Bernos10], the MgO layer, which is RF sputtered on a unoxided silicon surface is textured with a very good planarity. The Figure 2.2-a shows the high-resolution cross-section image of the sample after annealing obtained by transmission electron microscope: starting from the Si (100) substrate, an amorphous Si layer followed by the 2 nm thick barrier can be successively observed.

3. The bilayer structure Pt (2 nm) / IrMn (7.5 nm) / Co (5 nm) / Cu (3.5 nm) / Co (5 nm) / MgO (3 nm) / *n*-Si (100), denoted by MgO_2. It contains two ferromagnetic layers decoupled by a thin non-magnetic Cu metallic layer. One of the cobalt layers is covered by the antiferromagnetic layer IrMn, which shifts the cobalt hysteresis loop due to the exchange interaction at the interface of both layers. To crystallize the MgO

junction and to block the exchange layer, the structure has been annealed for 1 hour in an external field of 200 Oe directed along its easy axis. This structure is designed to form a spin valve for hot electrons. The first cobalt layer polarizes the electron beam by passing a spin direction. The second cobalt layer stops or transmits the polarized electrons depending on its magnetization orientation with respect to the one of the polarizing layer.

The two last samples were grown at the Laboratory of Material Physics (LPM), at the Nancy University.

II.2.2 Electric characterization of the samples

II.2.2.1 Current transport in metal / oxide / semiconductor structures

As previously mentioned, all the samples dedicated to the electron transmission experiments should present the rectifier electrical properties, so that the junction resistance is much larger than the access resistance of the junction. Here we start to give a short survey of the electronic transport in metal / insulator / semiconductor structure.

In MIS structure, the current-voltage characteristics critically depend on the insulator thickness, since the tunneling probability varies exponentially with the thickness. If the insulator layer is sufficiently thick (for instance, for the Si-SiO_2 system greater than 7 nm [Av-Ron78]) the carrier transport through the insulator layer is negligible and the MIS structure is equivalent to a conventional MIS capacitor. On the other hand, if the insulator layer is very thin (less than 1 nm), little hindrance is met by carriers flowing between the metal and the semiconductor, and the electric behavior looks like a Schottky-barrier diode at least at low bias voltages. Then most of the biasing voltage will be applied to the semiconductor. In this case, the tunneling probability term $\exp(- d h^{1/2})$, where d is the oxide

thickness and *h* is the mean barrier height (Figure 2.1), is close to unity and the tunneling current can be approximated by an expression similar to the standard thermionic-emission equation for Schottky barriers. Samples having an ultra-thin oxide layer (≤ 2 nm) should correspond to the latter case. The basic transport mechanisms are the thermionic emission and tunneling. The tunneling current dominates when the width of the depletion layer is thin enough. Here we recall that the depletion-layer width decreases with the impurity concentration of the semiconductor. So for heavily doped semiconductors the tunneling current may become more significant. The major expected differences of MIS structure compared to the conventional metal / semiconductor contact should be a reduced thermionic current of electrons because of the additional interfacial layer without affecting the minority current, a lower barrier height (the existence of defect states across the interfacial layer), a higher ideality factor, and the possibility of modulating the carrier concentration at the semiconductor surface by bias voltages (then all the applied voltage drops across the oxide barrier). Along this thesis, by ease of use we will designate our samples as Schottky-barrier diodes.

When measuring the I-V characteristics of Schottky-barrier samples, some specific care has to be taken because of recurrent high contact resistances. Figure 2.3 shows such a case, where the back side contact has a high contact resistance. The two-terminal device essentially corresponds to two metal / semiconductor contacts connected back to back, i.e. two Schottky barriers connected back to back. When a low negative voltage is applied to the metal-semiconductor contact 1 with respect to Contact 2, the barrier Φ_1 is reverse-biased and Φ_2 is forward-biased. The applied voltage is shared between these two contacts but most of the voltage drop will occur across the depletion region of Contact 1. The electron current is due to the thermionic emission of electrons from Contact 1. Note that the current continuity requires that the reverse current for the Contact 1 is equal to the forward current for the Contact 2, assuming same areas for both contacts. Therefore to avoid the voltage drop across

the barrier of the Contact 2, we need to have an Ohmic contact with a very small contact resistance compared to the semiconductor resistance. A criterion to check the nature of transport across the back side is to measure the current-tension (I-V) characteristics under light illumination of energy larger than the semiconductor energy band gap. Indeed electrons, which are photoexcited across the semiconductor energy band gap, will diffuse toward the back side of junction in the same direction as the reverse saturation current, which gives an augmented current. The absence of such a photocurrent in I-V curves under reverse bias means that most of the carriers are blocked by a Schottky barrier on the back side. We will now briefly describe the I-V characteristics of an ideal Schottky diode, which we will use to analyze the rectifying electrical properties of our samples.

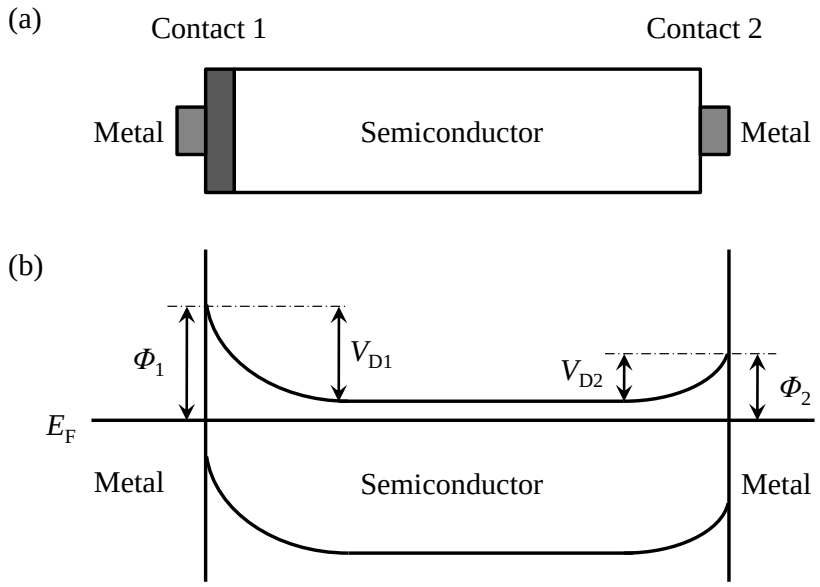

Figure 2.3: Schematic diagram of (a) a two-terminal device constituted of a Metal / Oxide / n-doped Semiconductor structure with the metallic contacts on both sides, whose high contact resistance at the back side (Contact 2) leads to two Schottky barriers connected back to back (the oxide layer is not shown), and (b) the corresponding band energy diagram at thermal equilibrium, where Φ_1 and Φ_2 are the barrier heights for electrons and V_{D1} and V_{D2} are the built-in potentials for contacts 1 and 2 respectively [Tantraporn70].

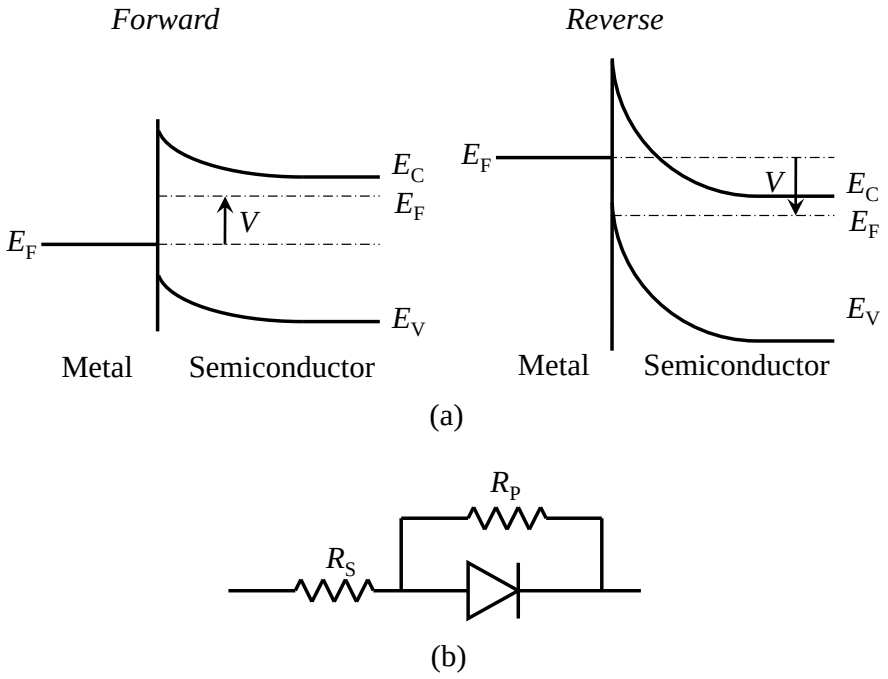

Figure 2.4: (a) Energy band diagram of metal on n-type semiconductor under different biasing conditions V. The electron flow is more important under Forward bias (V > 0) than under Reverse bias (V < 0). And (b) its equivalent circuit including the (access) series resistance R_S and the differential resistance R_P including the resistance due to the Schottky barrier and the resistance due to leak current through the junction. The differential capacitance of the space charge region is omitted. In the electron transmission experiments, the resistance R_S will be assimilated to the contact resistance r_B. (cf. Figure 2.20)

In the assumption of an ideal Schottky diode with moderately doped semiconductor, the main transport mechanism is the thermionic emission of majority carriers from the semiconductor over the potential barrier Φ_B into the metal. The current density flowing in the junction under an applied voltage V is given by the well-known equation: $J = J_0 [\exp (eV / kT) - 1]$, where $J_0 = A^* T^2 \exp (-\Phi_B / kT)$ is the saturation current density [Rhoderick78]. The effective Richardson constant A^* is equal to 8.64 A cm^{-2} K^{-2} for GaAs, 246 A cm^{-2} K^{-2} for silicon in (100) directions, and 258 A cm^{-2} K^{-2} for silicon in (111) directions, respectively. The equivalent circuit of a Shottky barrier includes the series resistance R_S which accounts for the contact resistance and the resistance of the neutral

semiconductor region between the ohmic contact and the depletion region (Figure 2.4). Therefore the voltage drop across R_S causes the actual voltage drop across the depletion region to be less than the applied bias V. So in the above equation, the applied bias V has to be replaced by the effective bias $V_{eff} = V - IR_S$, I being the current through the diode, which stands for the real potential drop across the barrier.

The following parameters fully characterize the electrical performances of our Schottky diodes:

- J_0, the dominant electron flow from the metal to the semiconductor for low reverse bias V. We thereafter refer to reverse bias as positive voltage applied to the *n*-type semiconductor back side with respect to the metal side. For small V values, $J \cong J_0\, eV / kT$, and 1 mV bias gives a current density $J \cong J_0 / 25$, which constitutes the lower limit of the polarization current. Therefore since our transmission experiments will be performed at zero bias, the samples must have values of J_0 as low as possible. The additional argument for minimizing J_0 is that the mean square noise current of shot noise for the Schottky junction is proportional to J_0. We will show that values of dark current of a few nA can be strongly detrimental for the detection of transmitted current.

- Φ_B, the potential barrier.

- The ideality factor $n = e / kT\, [dV / d(\ln J)]$, whose deviation from unity indicates that the thermionic transport is not the only dominant mechanism.

- The dynamic resistance of the Schottky barrier $R_0 = S^{-1} (dJ / dV)^{-1} = kT / [\, e\, S\, (J + J_0)]$ measured at zero bias (S is the surface of the sample), arising from the space charge region, where electrons are depleted in *n*-type semiconductor. Note that for several tenths of a volt of reverse bias $J \approx -J_0$ and R_0 becomes infinite. The R_0 resistance determines the Johnson noise of the junction.

II.2.2.2 How to measure I-V characteristics

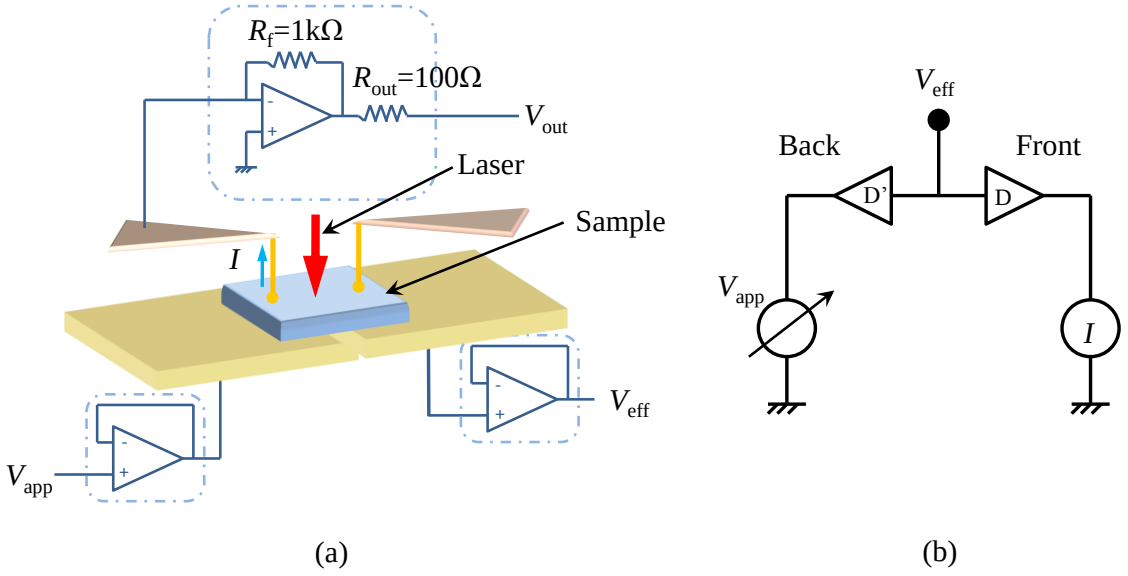

Figure 2.5: Three-terminal I-V measurement. (a) Experimental setup. The voltage is applied across the back terminal, I is the measured current through the MIS structure and V_{eff} corresponds to the genuine voltage applied to the back contact. Since the voltmeter has very high impedance, the current flowing between the back side pads is practically zero. (b) Equivalent circuit. D and D' correspond to the back junction and the front junction respectively.

We perform all the measurements with three-terminal system to directly get the real applied voltage V_{eff} to the back side of the sample, as shown in Figure 2.5.

To form an ohmic contact on the semiconductor backside, we deposit a drop of liquid metal, a gallium based alloy. The bias voltage V_{app} is applied to one pad on the back side and the voltage effectively applied V_{eff} is measured on the other pad. Then the voltage difference $V_{app} - V_{eff}$ corresponds to the voltage drop across the back side contact due to contact resistances and local junction resistance of non perfect ohmic contact. Two voltage followers are used to provide enough current gain. A soft gold tip is gently pressed on the top metal surface of the sample to measure the total current *I*, which is then converted into the output

voltage V_{out} of the amplifier with respect to the ground. Another gold tip is used to mechanically hold the sample. The I-V measurements can be easily performed in the dark and under illumination (630nm, 1.4mW).

In this configuration, the voltage is applied to the semiconductor side of the sample, which is opposite to the convention generally used in the measurement of I-V. Thus, in order to simplify the analysis of the electrical measurements and avoid any ambiguities, our I-V curves will be drawn to be compatible with the usual configuration, where the voltage is applied to the metal side of the diode.

II.2.2.3 Electrical characterizations of the samples

II.2.2.3.a Pd (5 nm) / Fe (4 nm) / Uvocs (1 nm) / *n*-GaAs, (sample GaAs_1): **An excellent Schottky diode**

For simplicity, bias denotes the real voltage applied to the junction of the sample V_{eff}. The I-V curves (Figure 2.6) present the electrical characteristics of a Schottky-barrier diode. A forward bias (positive voltage applied to the metal) decreases the potential barrier for electrons moving from the semiconductor into the metal. As the bias increases the current densities measured in the dark and under illumination follow an identical increase. On the other hand, in the reverse direction, a nearly constant difference of 1875 $\mu A/cm^2$ between the two measured densities appears as the negative bias increases. It leads to a photovoltage of 0.24 V, which corresponds to the positive shift of the minimum of the absolute current density. The existence of a photocurrent demonstrates that electrons generated in the conduction band of the semiconductor diffuse toward the metal contact on the back side, while holes created in the valence band diffuse toward the front metal contact. Let us emphasize that this photocurrent can be collected without bias.

The analysis of the I-V curves measured in the dark can be done by fitting the thermionic-emission equation (dashed line in Figure 2.6), which leads to the extraction of the following parameters (R_P is calculated from the raw data because of the deviation of the fitting curve from the measured one in case of high forward bias, the same treatment also for the other samples):

R_S = 23.3 Ω, R_P = 4.41 MΩ, R_0 = 160 kΩ, n = 1.003, Φ_B = 0.71 eV, and the saturation current density J_0 = 0.78 μA/cm^2.

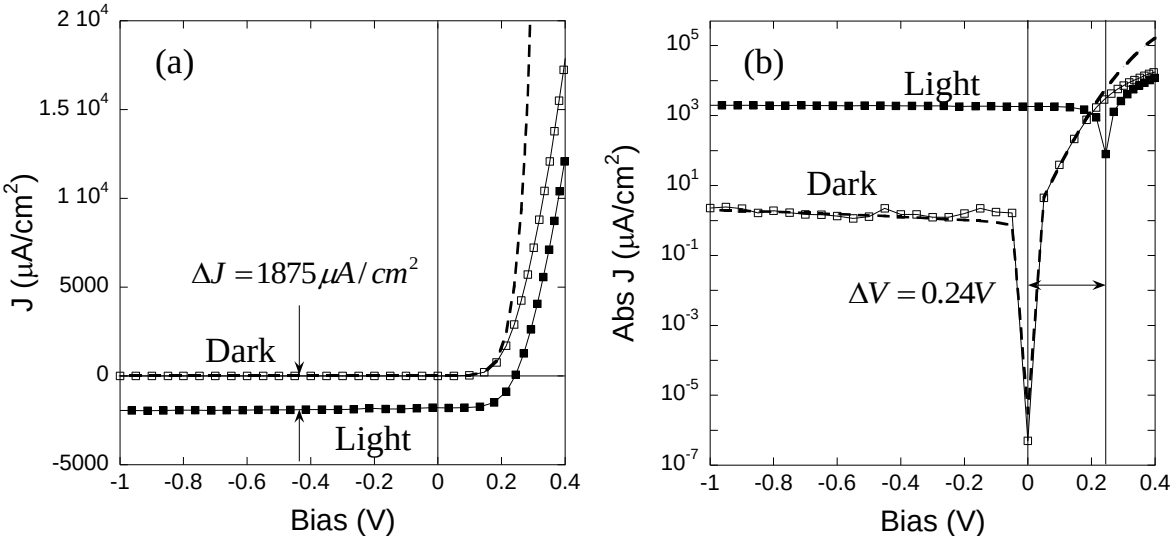

Figure 2.6: Measured and calculated (dashed lines) I-V curves for the n-type sample GaAs_1 (surface 0.35 cm^2) in dark and under irradiation by a red laser (1.96 eV, 2.15mW). (a) Current density versus Bias in semi-log scale; (b) Absolute current density versus Bias in semi-log scale. A constant photocurrent density of 1.875 mA / cm^2 and a shift of 0.24 V of Bias is detected at zero bias under laser illumination. The dashed lines correspond to the fitting to the thermionic emission equation.

Let us recall that this procedure allows comparing different samples but does not take into account the oxide thickness. We can only assert that the I-V curves of GaAs_1 samples are very well described by electron flow driven by the thermionic emission from the semiconductor to the metal. The high value of the parallel resistance R_P ensures that there is nearly no resistance-dependent leakage current. Also the relatively small series resistance R_S

indicates that almost all the voltage drop is on the metal-semiconductor contact but not on the metal itself. The value of the semiconductor barrier height Φ_B is in agreement with the one previously found [Rougemaille03]. This sample satisfies the electrical conditions listed in Section II.1.

II.2.2.3.b Pt (3 nm) / Co (5 nm) / MgO (2 nm) / *n*-Si (100) (10^{15} cm^{-3}) (sample MgO_1): **A situation intermediate between a Schottky diode and an MIS structure**

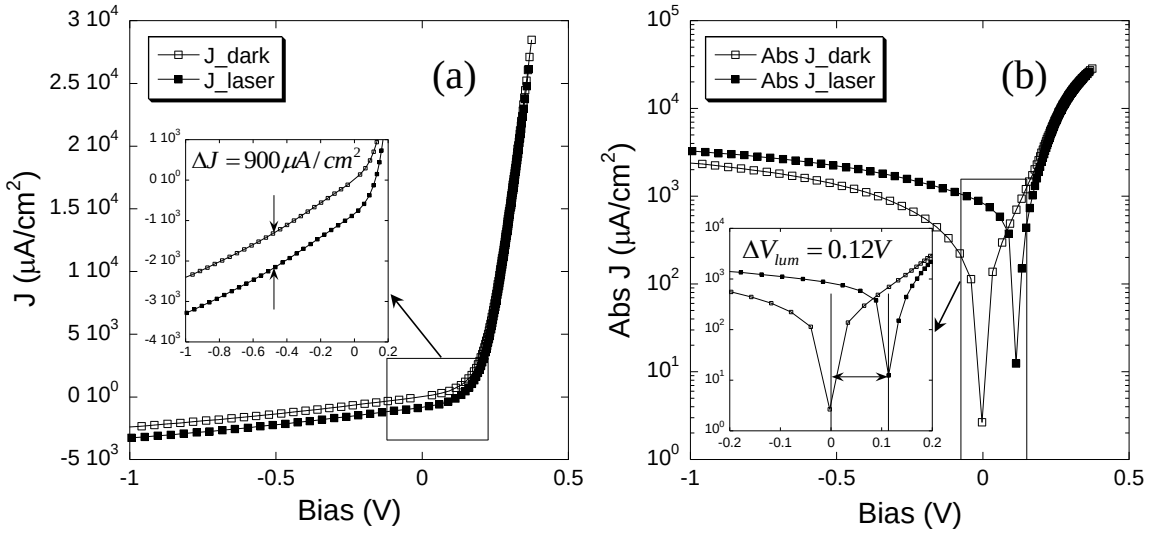

Figure 2.7: Measured I-V curves for the n-type silicon sample MgO_1 (surface 0.25 cm^2) in dark and under red laser illumination (1.96 eV, 1.4 mW). (a) Current density versus Bias in linear scale; (b) Absolute current density versus Bias in semi-log scale. A constant photocurrent density of 900 $\mu A/cm^2$ and a shift of 0.12 V of Bias at zero current are detected under laser irradiation.

As the oxide layer thickness increases from 1 nm (sample GaAs_1) to 2 nm (sample MgO_1), we can observe the transition from the Schottky barrier (sample GaAs_1, which has an interfacial layer essentially transparent to tunneling electrons) to a MIS-like structure (sample MgO_1). The I-V curves measured at room temperature show a nonlinear behavior (Figure 2.7). The rather unexpected result is that the presence of MgO oxide allows current flows of several orders of magnitudes for *forward* (positive bias) and *reverse* bias. As explained below, it indicates that the MgO layer effectively acts as a tunnel barrier. The

presence of the oxide layer allows the band structure of the metal and Si to displace in energy relative to one another. The tunneling current therefore depends on the position of the metal Fermi level relative to the band edges of the semiconductor, which in turn depends on the voltage across the oxide layer.

Before describing the different regimes of the I-V characteristic of the MgO MIS contact (Figure 2.7), let us mention that a thorough characterization of these regimes requires complementary capacitance measurements (C-V curve), in particular to evaluate the contribution of the surface band bending, the total interface-trapped charge, and the depletion depth. Such measurements cannot be performed in our laboratory.

At low bias, the surface of the *n*-type Si is depleted, leaving a positive charge due to uncompensated ionized donors (Figure 2.8). In the forward bias range (Bias > 0 in Figure 2.7) two different slopes are observed: at the lower voltage, the current increases exponentially over two decades due to the thermionic emission, while at higher bias voltage, tunneling occurs through the MgO barrier. As the bias is increased in forward direction, the semiconductor surface goes from depletion to accumulation and the changes in applied voltage are primarily absorbed across the oxide. This causes the metal Fermi level to move downwards on the band diagram relative to the semiconductor, until it reaches the energy of the valence band edge in the silicon. At this point (small hump at 0.2 V in the I-V curve) the tunneling current (from semiconductor valence band to metal), rapidly increases with bias. The reverse bias is associated with the tunneling current from the conduction and valence bands in Si to metal. On reverse bias the large concentration of holes creates a strong oxide field, which leads the metal Fermi level to move upwards to the conduction band edge of Si. At this point the tunneling current between the metal and the conduction band becomes small. As mentioned above, considering the absence of the additional information given by C-V curves, it is impossible to settle whether the silicon surface stays depleted or becomes inverted in the reverse regime.

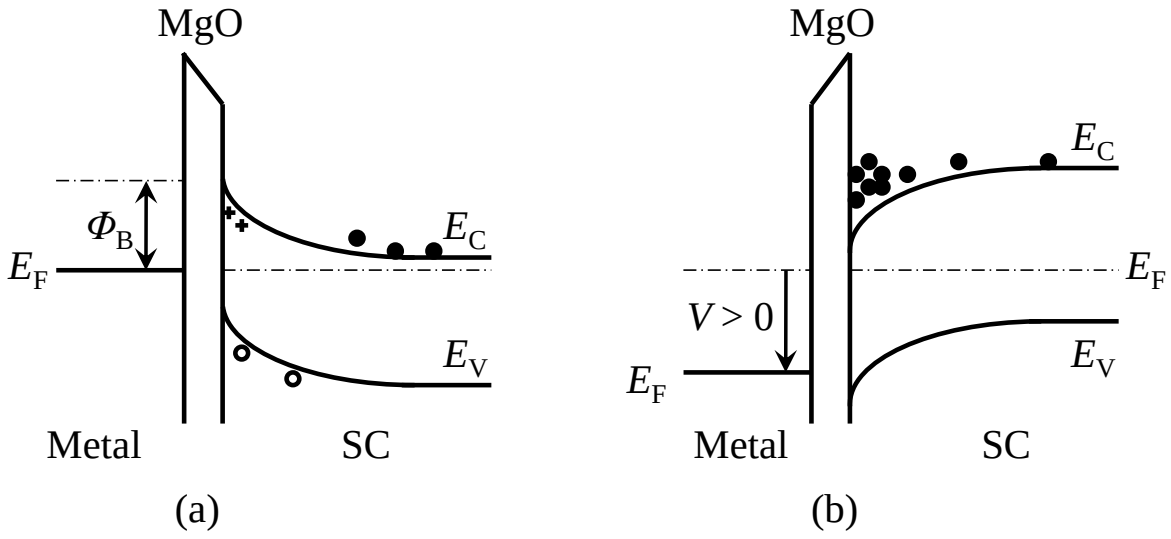

Figure 2.8: Energy band diagrams for ideal n-type MIS diode (a) under zero bias and (b) under forward bias for the conditions of (a) depletion and (b) accumulation.

If we consider the thermionic-emission model of electrons over the barrier Φ_B without taking into account the oxide layer, in order to fit the I-V curve at low applied bias, we get the parameters:

R_S = 25.9 Ω, R_P = 2.28 kΩ, R_0 = 1.2 kΩ, Φ_B = 0.63 eV, n = 1.005, J_0 = 497 μA/cm^2.

The fit reproduces very well the I-V curve at low bias and the transition to the asymptotic regime in the reverse bias but fails to describe the forward regime. The access resistance R_S is decreased by the order of 10 Ω. The evaluated barrier height is in agreement with previous values reported in the literature for magnetic tunnel junctions of similar MgO thickness, such as CoFe / MgO / Si [Kiyomura00, Uhrmann08].

II.2.2.3.c Pt (2 nm) / IrMn (7.5 nm) / Co (5 nm) / Cu (3.5 nm) / Co (5 nm) / MgO (3 nm) / *n*-Si (100) (10^{-15} cm^{-3}) (Sample MgO_2): **Towards an MIS diode**

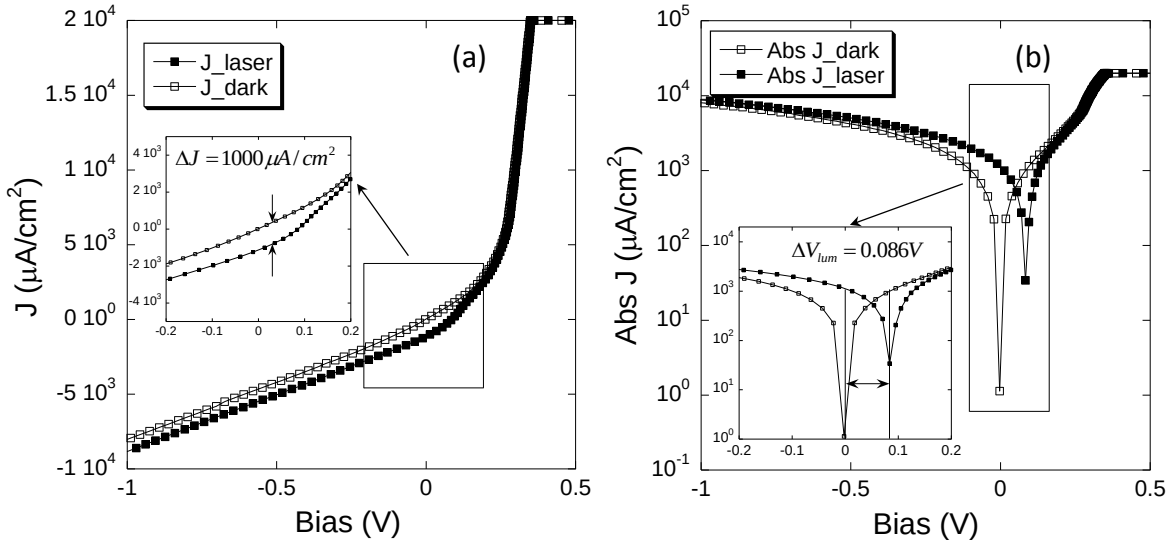

Figure 2.9: Measured I-V curves for the n-type silicon sample MgO_2 in dark and under laser illumination (1.96 eV, 1.4 mW). (a) Current density versus Bias in linear scale; (b) Absolute current density versus Bias in semi-log scale. A constant photocurrent density of 1000 $\mu A/cm^2$ and a shift of 0.086 V of the Bias at zero current are detected under light illumination (surface sample 0.5 cm^2). Note the increase in the reverse current with respect to the sample MgO_1 of thinner oxide layer. This comes about as a result of an increase in the Fermi energy of the metal relative to the Si surface.

From the measured I-V curves (Figure 2.9), we conclude unexpectedly that a thicker oxide layer increases the reverse-bias current. The mechanism for the reverse current results from tunneling through the oxide, when the metal Fermi level increases towards the Si conduction band edge E_C. Since enough voltage is dropped across the oxide, the metal Fermi level can move up to E_C. A thinner oxide layer will sustain a smaller voltage and there will be fewer electrons in the metal above the energy E_C. The decrease in the reverse current compensates the increased transmission due to a thinner oxide layer. Notice that the pronounced hump at 0.2 V is caused by the resultant increase in tunneling electron current from Si valence band edge to metal. The irradiation of the red laser (1.96 eV, 1.4 mW) generates a density of photocurrent of 1×10^3 μA/cm^2, which leads to a photovoltage of 0.086 V at the minimum of the absolute current density. The parameters obtained from the fitting procedure are:

R_S = 11 Ω, R_P = 253 Ω, R_0 = 180 Ω, Φ_B = 0.64 eV, n = 1.015, J_0 = 336.7 μA/cm^2.

One again that the fit procedure overestimates the forward regime as shown by the departure of the ideality factor from unity but gives a reliable result for the reverse regime with an identical barrier height and an access resistance R_S of the same order of magnitude.

II.2.3 Magnetic characterizations

It consists in measuring the hysteresis loop to determine the coercivity and the easy axis of magnetization.

II.2.3.1 Sample GaAs_1

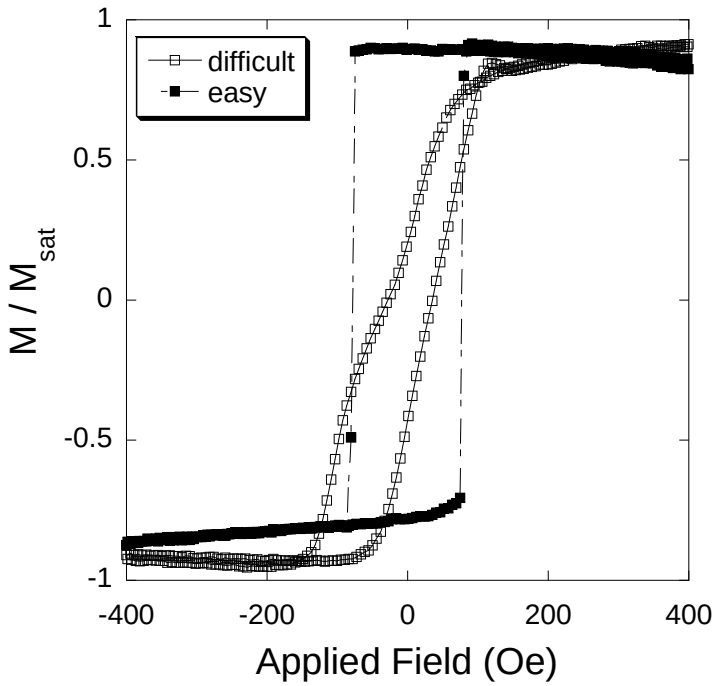

Figure 2.10: Hysteresis loop of the sample of the junction GaAs_1 measured by MOKE. The magnetic field is successively applied along the easy axis and the difficult axis. The magnetization is normalized by the magnetization at saturation.

According to the preparation of the sample, the magnetic easy and difficult axes of the sample are known. The hysteresis loops of the sample GaAs_1 are measured by Magneto-Optic Kerr Effect (MOKE) in geometry of reflection in the directions of the easy axis and the difficult axis, as shown in Figure 2.10. The magnetization is normalized by the magnetization at the saturation. The measured coercivity of the ferromagnetic layer is around 75 Oe.

II.2.3.2 Sample MgO_1

The hysteresis loop of the sample MgO_1 obtained by SQUID in the direction along the planar easy axis, is shown in Figure 2.11. The magnetization is calculated by dividing the measured average magnetic moment by the sample surface. A saturation of the magnetization of 3×10^{-4} emu/cm^2 is reached along with a coercivity of about 15 Oe. Note that the remanent magnetization $(3 \times 10^{-4}) / (5 \times 10^{-7}) = 600$ emu/cm^3 is quite low compared to the expected bulk value of 1400 emu/cm^3 in Co.

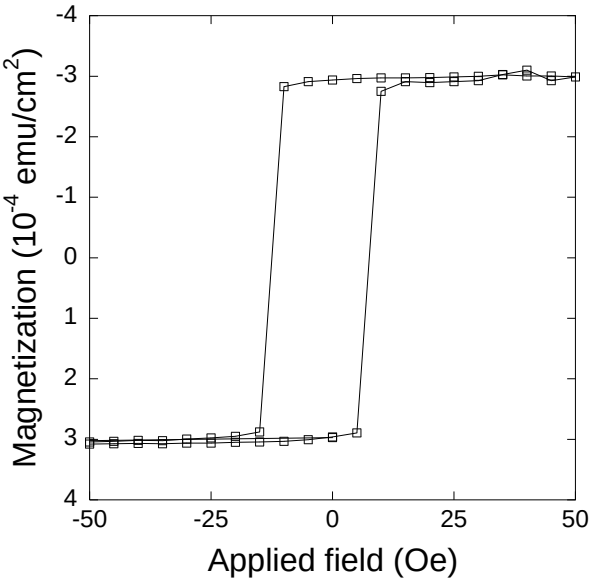

Figure 2.11: Square hysteresis curve of the sample MgO_1 measured by SQUID along the planar easy axis (5 nm thick Co). The magnetization saturates at 3×10^{-4} emu/cm^2 and the hysteresis loop has a coercivity of 15 Oe.

II.2.3.3 Spin-Valve sample MgO_2 with exchange bias

The hysteresis loop of the sample MgO_2 measured by SQUID reveals two cycles shifted from one another of 130 Oe in the field axis, i.e. the exchange bias (Figure 2.12). The top ferromagnetic layer (the pinned layer) in contact with the antiferromagnetic layer has the shifted loop, while the other ferromagnetic layer (the free layer) has a conventional hysteresis loop centered at zero field. Thus there is a field range, where the two ferromagnetic layers have antiparallel (AP) magnetizations. The field needed to reverse completely the ferromagnetic layer in contact with the antiferromagnetic layer is larger because an extra field is required to beat the microscopic torque. An external magnetic field of 50 Oe is enough to switch from the parallel (P) configuration to antiparallel configuration of both ferromagnetic layers. The saturated magnetizations of both layers are equal to 5×10^{-4} emu/cm^2 (i.e. 1000 emu/cm^3) and are much larger than that of the sample MgO_1.

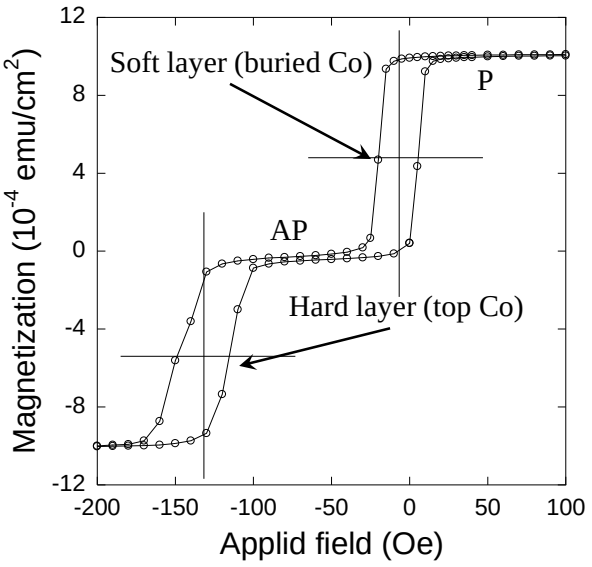

Figure 2.12: Easy axis major and minor magnetization loops of the sample MgO_2 measured by SQUID. The two cycles are separated one from the other by an exchange bias of 130 Oe. P= parallel configuration AP = antiparallel configuration

II.3 Electric transmission measurements

As opposite to GMR experiments, we plan to inject spin-polarized electrons into sample at energies well above the Fermi level of the ferromagnetic layer. All our transmission experiments focus on the spin-dependent transport in the unoccupied bands of the metal layers. The approach applied in our experiment has two main advantages: first the energy of the incident electrons is easily tunable and second the spin polarization of the incident electron can be optically modulated, since the electron emitter is decoupled from the sample. We briefly give an overview of the main features of our experimental setup.

II.3.1 The experimental setup

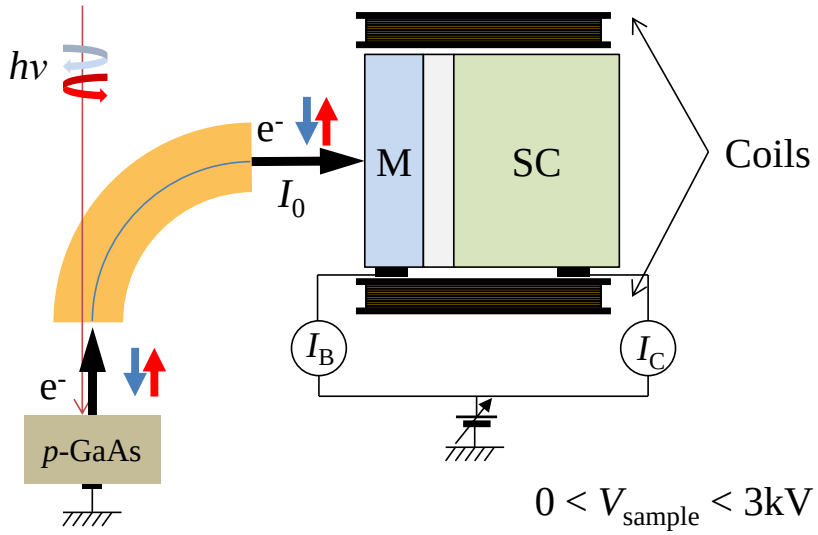

Figure 2.13: Scheme of the experimental setup. The spin-polarized electrons, which are photo-emitted from the p-type GaAs photocathode, are focused on the Ferromagnetic Metal / Oxide / Semiconductor junction. The spin polarization (vertical arrows) is parallel to the in-plane magnetization. The energy of the incident electron is given by the applied voltage V_{sample}. The two coils enable to reverse the saturated magnetization. The absorbed current I_B is measured at the metal side (M or base) and the collected current I_C is measured at the back side of semiconductor (SC or collector).

The principle of the experiment is schematically described in Figure 2.13. In the ultra-high vacuum chamber, the spin-polarized electron beam is generated by optical pumping of *p*-type GaAs. The electrons are then injected from the vacuum into the metallic surface of the sample via an electron optics. The currents collected at the front and the back sides of sample are labeled respectively as the base current I_B and the collector current I_C. The energy of the electrons impinging the sample surface can vary from 0 to 3 keV by applying the same voltage on both sides of the samples. Note that this configuration requires measuring both currents under high voltage, which turns out to be a non trivial task.

The main components dedicated to the transmission experiment are: the photoelectron emitter, the electron optics, and the detection chain for measuring very weak currents.

II.3.2 How to achieve an electron source

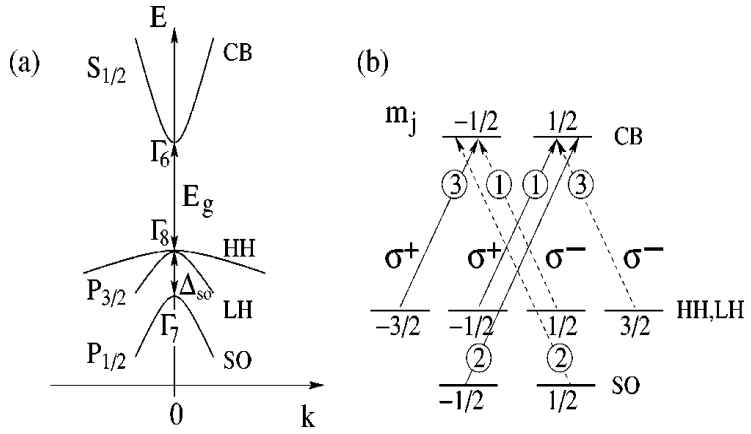

Figure 2.14 [Lampel68]: Optical orientation in GaAs: (a) schematic band structure of GaAs near the center of the Brillouin zone, where E_g is the band gap and Δ_{so} the spin-orbit splitting; CB, conduction band; HH, valence heavy hole; LH, light hole; SO, spin-orbit split-off subbands; $\Gamma_{6,7,8}$ are the corresponding symmetries at the k = 0 point; (b) selection rules for interband transitions between the sublevels m_j for circularly polarized light σ^+ and σ^-. The circled numbers indicate the relative transition probabilities for both excitations (depicted by the arrows).

The polarization of the electron beam is acquired by the optical pumping technique, whose basic principle is recalled in Figure 2.14. The main point is that absorption of σ^+ circularly polarized infrared photons of the energy $h\nu$ close to the GaAs band gap E_g ($E_g < h\nu < E_g + \Delta_{SO}$) gives a theoretical spin polarization $P = (n^+ - n^-) / (n^+ + n^-)$ = (1 – 3) / (1 + 3) = –50 % [Lampel68, Meier84, Hermann85]. Due to a difference in transition probabilities three times more electrons of spin –1/2 are excited by σ^+ light into the conduction than electrons of spin 1/2. The actual value of the spin polarization of the electron beam at room temperature, which was experimentally determined by Mott scattering [Drouhin85b], is reduced to –25 % due to the spin relaxation of electrons in the band bending region before being emitted into vacuum. The sign of polarization is inversed by switching the polarization of the infrared excitation from σ^+ to σ^-.

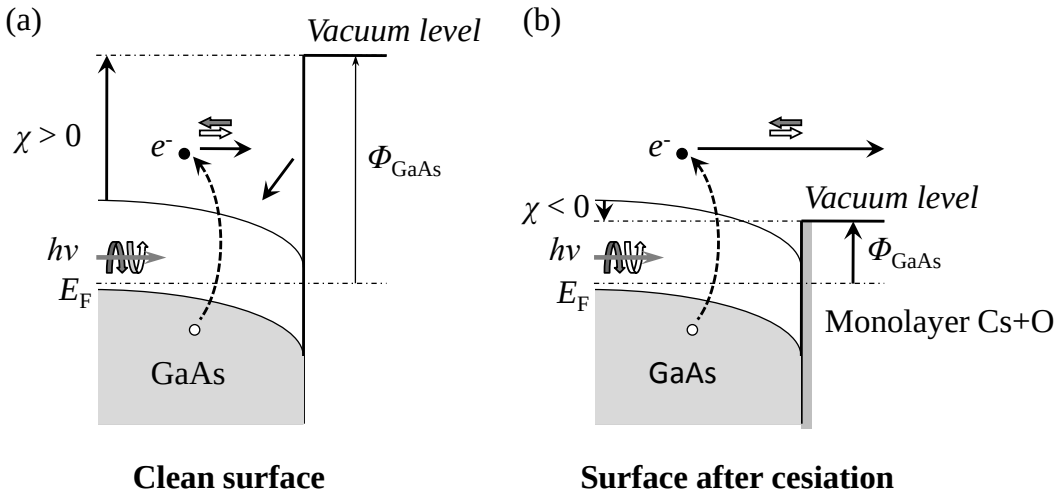

Figure 2.15 [Pierce75]: Lowering of the p-doped GaAs work function by surface activation in negative electron affinity (N.E.A.). (a) Clean GaAs surface. (b) GaAs surface N.E.A. activated by Cs and O_2 deposition. χ stands for the electron affinity and Φ_{GaAs} is work function of GaAs. In optical pumping process, the spin orientation axis of the photoelectrons is parallel to the direction of light excitation.

If *p*-type GaAs surface is shined by infrared light of energy close to E_g, no electrons can

come out since their energy is too low to cross the vacuum barrier of the amplitude between 4 and 5 eV. Therefore we need to well lower the work function below the bulk conduction level of GaAs in order to free photoexcited electrons into vacuum. This technique is called Negative Electron Affinity (N.E.A.) activation (see Figure 2.15) [Pierce75]. The N.E.A. activation process is now well controlled: it consists in evaporating an alkaline metal such as Cs (or Na, K [James69, Pierce75]) under oxygen flow to form a monolayer over the surface of GaAs, until the vacuum level at the GaAs surface shifts below the bottom of the bulk conduction band. Then the final work function is about 1 eV and any electron near the surface in the conduction band can escape into vacuum. The following task is now to obtain a stable electron source, whose work function does not steadily step up over few hours.

In order to realize a stable photocathode, some treatments should be done before and after introducing the photocathode into vacuum. In practice, we choose the *p*-doped GaAs [001] with two different doping levels of 2.1×10^{19} cm^{-3} and 8.3×10^{19} cm^{-3}.

Prior to the introduction of the photocathode into vacuum, the following chemical cleaning and surface passivation process are done *ex-situ*:

1) Dip the GaAs crystal in the solution of acetone and wash it with ultra-sonic excitation for 15 min;

2) Dry the crystal with gas flux of propyl;

3) Etching the crystal in concentrated sulfuric acid solution for 5 min;

4) Rinse the crystal in pure deionized water for several times;

5) Etching the crystal in piranha solution (H_2SO_4+H_2O_2+H_2O);

6) Rinse the crystal with pure deionized water for several times and dry the surface with isopropyl.

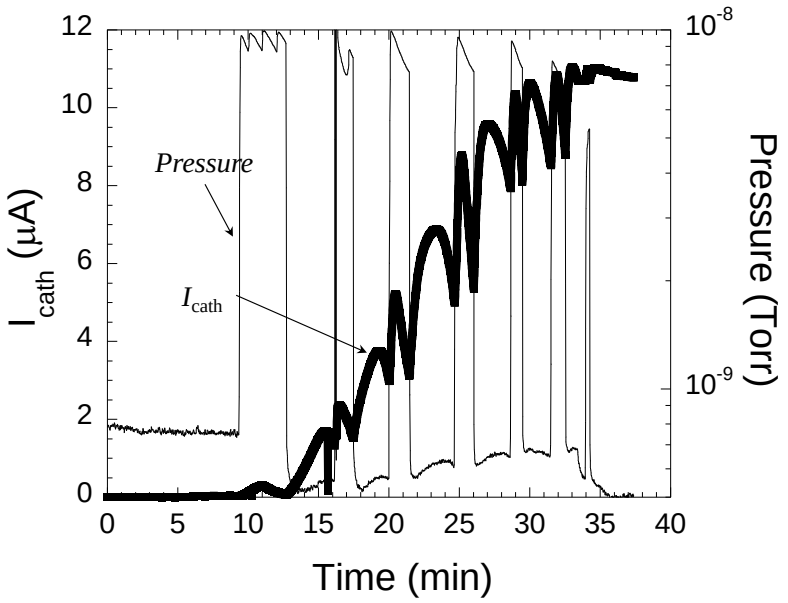

Figure 2.16: Cesiation process monitored in real time by the excitation of a 1.96 eV red laser (630nm, 0.85 mW) with the measurement of the photoemitted current. The subsequent jumps of pressure are the oxygen inlets, which kick the photoemitted current. The quantum yield of the resulting photocathode is $h\nu I_{cath} / P = 2.53\ \%$.

After the GaAs crystal is chemically cleaned, it is introduced into vacuum and then activation is done. To activate the GaAs surface in N.E.A. in the vacuum, an in-situ surface cleaning needs to be achieved by heating the crystal uniformly at a high temperature between 570 ℃ and the evaporation temperature of GaAs (about 600 ℃) for a period of tens of minutes. Then the Cs dispenser is turn on and the control of cesiation process is achieved by the excitation of a red laser of 1.96 eV, with the measurement of the photoemitted current. The onset of current occurs when the work function at the surface of GaAs reaches a value close to 1.96 eV. The peculiar "yo-yo" behavior of the photoemission comes from continuous Cs evaporation and repeated oxygen inlets (process shown in Figure 2.16).

A photocathode should be heated and activated many times to give a stable current. Also the basic pressure of the vacuum should be maintained in the 10^{-11} Torr range. In the best case, the pressure remains in the 10^{-9} Torr range during the heating process and in the 6×10^{-10} Torr

range during the cesiation process. Typically in optical pumping conditions in the experiment, an excitation at 780 nm gives a stable photoemitted current of 1~2 μA.

II.3.3 How to focus and inject the electron beam

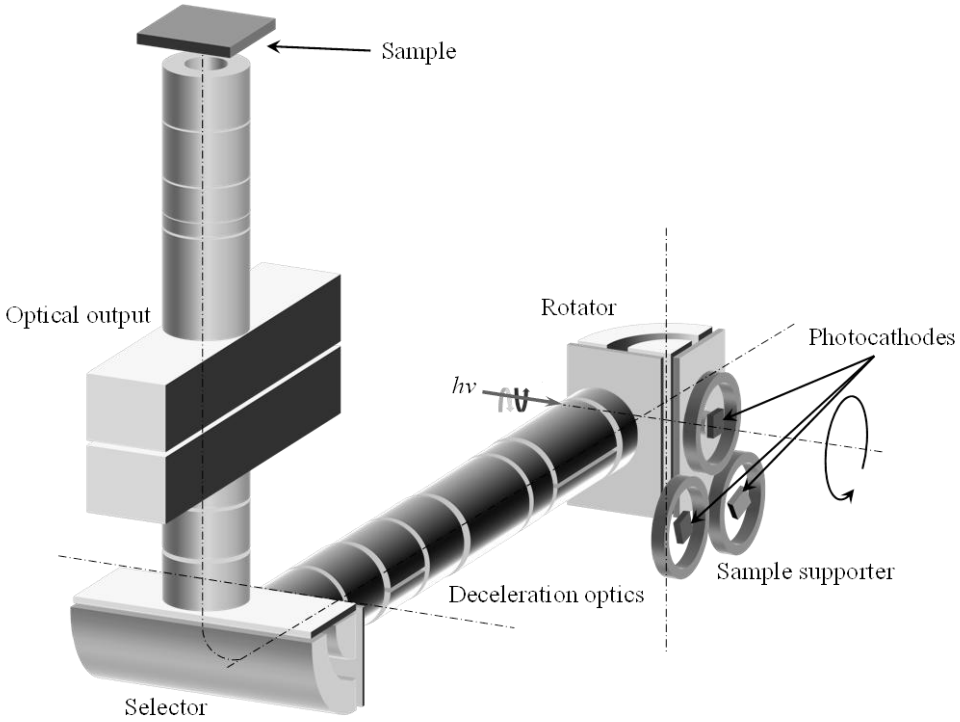

Figure 2.17 [Houdre85]: Scheme of the electron spectrometer comprising two 90° cylindrical electrostatic deflectors: the rotator and the energy selector. The electron beam, after rotation is first collimated, decelerated in three element cylinder lens, and then energy selected. The size of the electron spot focused on the sample surface is less than 1 mm and is kept invariant with the incident energy by adjusting the lens voltages. The arrow designates the spin orientation of the electron beam.

An electron optics is necessary to direct the photoemitted electrons from the photocathode to the front side of the sample. The type of electron optics that we have used consists of a group of electrostatic lenses. It has been designed in our group in the 1980s to work as a high resolution and high luminosity electron spectrometer, made up of two parts: a

90 ° rotator, which transforms the longitudinal spin polarization of the photoemitted electron beam into transverse, and a selector, which allows to achieve a narrow energy distribution of electrons (cf. Figure 2.17) [Drouhin82, Drouhin85a, Drouhin85b]. In the experiment, the performance of the electron spectrometer has been downgraded by working at an energy resolution of 200 meV, which corresponds to a total transmission of the electron optics of about 5 %. Working with a better energy resolution means the drastic reduction in the number of electrons entering the sample.

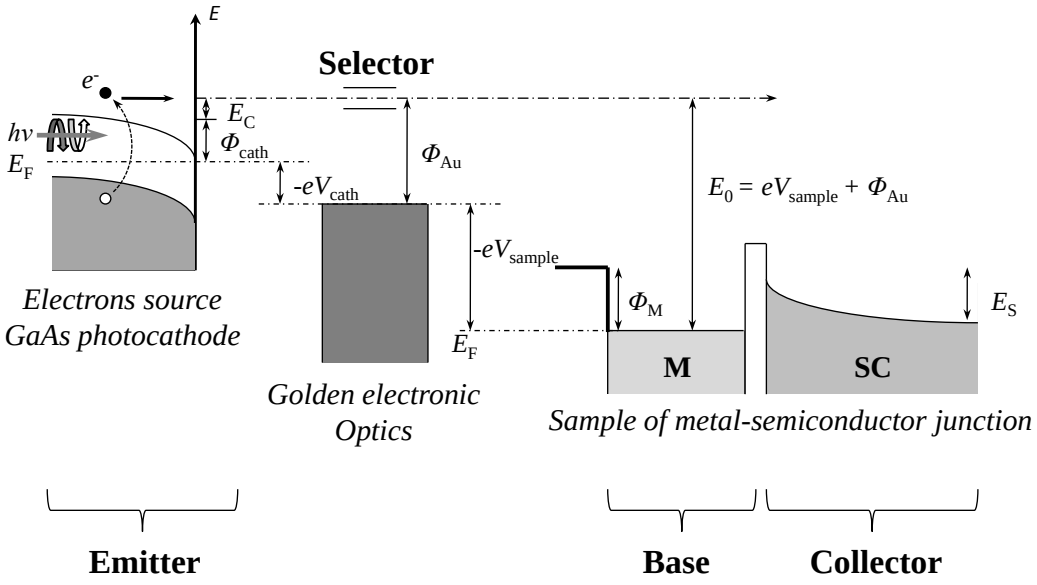

Figure 2.18: Energy diagram of the operating mode of the experiment. To select electrons of kinetic energy E_C, a negative bias is applied to the photocathode, so that electrons have a zero kinetic energy at the zero potential of the gold lenses of the spectrometer. The spectrometer acts as a pass band filter with a bandwidth of 200 meV centered at zero total energy. The injection energy E_0 of the electron beam is given by the voltage V_{sample} applied on the sample junction (Φ_{Au}: work function of the gold electrodes of the selector). Vertical scale is the total energy E (kinetics and potential).

Below we give the main lines of the operation mode of the electron spectrometer. The basic idea is to vary the photocathode bias to scan the electron energy distribution in front of the entrance slit of the spectrometer. In this case all voltages applied to the electrostatic

deflectors are kept fixed (cf. Figure 2.15). The conservation of the total energy requires that the kinetic energy E_C of the photoemitted electrons satisfies the following equation (Figure 2.18): $\Phi_{Au} = E_C + \Phi_{cath} - eV_{cath}$, where Φ_{cath} and Φ_{Au} are the work functions of gold and the GaAs photocathode, respectively, and V_{cath} is the potential applied on the photocathode which is negative. The injection energy E_0 can be defined by $E_0 = eV_{sample} + \Phi_{Au}$, where V_{sample} is the potential applied to the sample. So the injection energy is equal to the potential V_{sample} modulo Φ_{Au}.

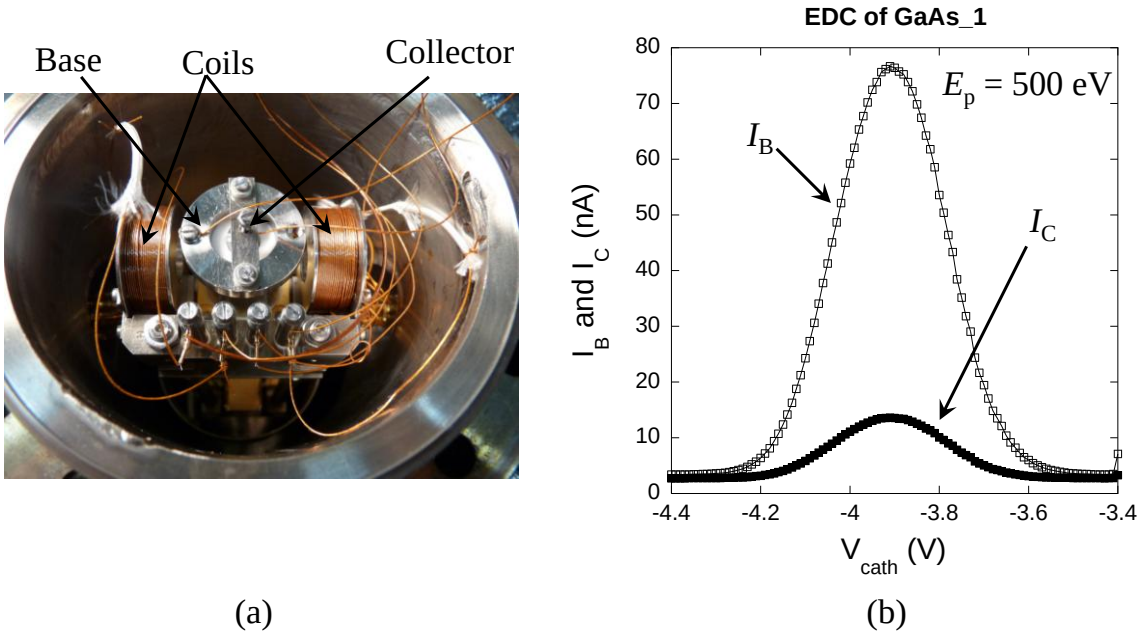

Figure 2.19: (a) Sample holder on top of the electron optics: The sample lies at the end of the cylinder (a magnetic material). The Base and Collector connections are insulated from one another. Two coils allow applying an external magnetic field in the plane of the sample. And (b) Energy distribution curves of the absorbed current I_B and the transmitted current I_C for an injection energy of 500 eV obtained by scanning the cathode potential for the sample GaAs_1: I_B = 78 nA and I_C = 14 nA. Note that the full width at half maximum of the curves is quite large, typically 0.3 eV. A better resolution of the electron spectrometer will curtail the current maxima.

The injected electrons enter the metal layer and the absorbed current or base current is measured on the front side by a gold circular diaphragm. The transmitted contribution is

measured on the back side via an InGa droplet to ensure an ohmic contact. The so-called currents I_B and I_C correspond to the maxima of the energy distribution curves (EDCs) of the respective currents (see Figure 2.19-b). For a given injection energy, we scan the voltage applied to the photocathode to precisely determine the maxima of both EDC's. To give an idea of the imperative sensitivity of our current measurement, let us consider the values of I_C obtained by the measurement of the transmission through the sample GaAs_1. The spin dependent signal for I_C is obtained by measuring the difference between I_C^+ obtained in case that electron polarization of + 0.25 and I_C^- obtained in case that the electron polarization of – 0.25. The polarization variation will produce two EDC's centered at the same cathode potential but accordingly shifted in amplitude due to the spin filter effect. Looking at the EDC of the current I_C measured for injection energy of 500 eV (Figure 2.19-b), it means two EDC curves shifted of 7.8 pA! Practically the difference between I_C^+ and I_C^- is acquired by modulating at 1 kHz the polarization of the light excitation between σ^+ and σ^- via an electro-optic modulator. The signal detected by a lock-in is then directly proportional to the difference $I_C^+ - I_C^- = \Delta I_C$. Then we have to check the magnetic signature of the signal ΔI_C, i.e. its change in sign upon reversal of magnetization. It is done by running a pulsed or a DC current into the magnetic coils surrounding the sample (see Figure 2.19-a) depending on the coercitive fields of the samples.

II.3.4 Current detections and noise considerations

Our specific goal is to be able of measuring an electron current flowing through a junction of finite impedance ranging a few tens of fA up to a few hundreds of nA. So it is mandatory to give an estimate of all the noises, which can hamper the current measurements and to identify the significant sources of noise. In our experiment the noise can be traced back to three sources:

1) Noise coming from the electron source.

The noise associated with the electron photocathode is the well known shot noise $(2eBI_0)^{1/2}$ where B is the bandwidth of our measurement and I_0 the incident electron current. For I_0 = 100 nA, fluctuations of the injected current is about 0.2 pA/(Hz)$^{1/2}$.

2) Noises inherent to the junction.

Before considering the parasitic current flowing into the junction when crossing by a current, we have to estimate the noise inherent to the junction with no injected current. One can show that at zero current the junction noise originates from the Johnson-Nyquist noise given by $(4k\tau B / R_0)^{1/2}$ where R_0 is the dynamic resistance of the junction and τ the absolute temperature. For R_0 = 1 MΩ (or 100 kΩ) the current noise of the junction is 0.13 pA/(Hz)$^{1/2}$ (or 0.4 pA/(Hz)$^{1/2}$) at room temperature.

We now calculate the current noise when a current is injected in it. We will show that it comprises a constant current noise independent of the transmission T and fluctuations of currents I_B and I_C linked to the fluctuations of the incident current I_0.

- "Background" component. As previously stated, currents I_B and I_C are separately measured at zero bias, but leakage currents will limit their detection. In our geometry, the base current is collected by an insulated circular diaphragm and not by a current-carrying tip as in the I-V measurements. Four-point-probe resistance measurements performed on the metal layer of our samples gives values of resistance of few tens of Ohms over a distance of 1 mm. Therefore we expect a contact resistance of the metal layer across the all area between the impact point of the electron beam and the diaphragm, which will induce a bias voltage and then a contact current. Our experimental configuration of collecting currents can be schematized by the contact resistance r_B in parallel with the junction resistance R_0 (Figure 2.20). The injected

current I_0 splits into the two currents $I_C = T\,I_0$ and $I_B = (1 - T)\,I_0$, where T is the transmission across the junction. The subsequent bias at the junction terminals A and B is $V_A - V_B = I_0\,[r_B - T\,(r_B + R_0)]$. When the transmission becomes negligible, $V_A - V_B \cong I_0\,r_B$. For $I_0 = 100$ nA and $r_B = 10\ \Omega$ the bias voltage is of the order of μV. Considering a typical junction resistance value of $R_0 = 1$ MΩ, it means a parasitic current of 1 pA arising only from the contact resistance r_B itself, whatever the injection energy. It then corresponds to a transmission of $T = I_C / I_0 = 10^{-5}$ for 100 nA injection. This transmission value fixes the lower detection threshold of the genuine transmission signal across the junction barrier.

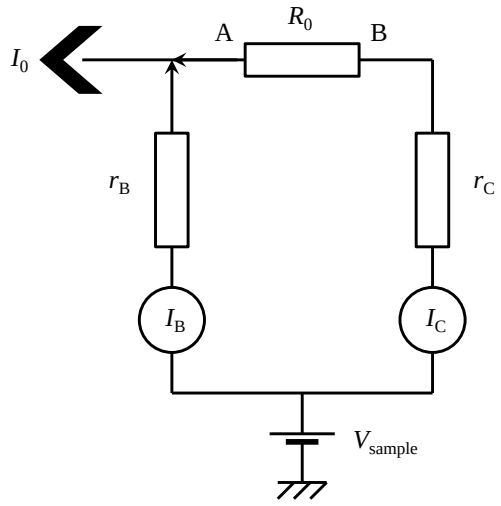

Figure 2.20: Equivalent circuit of the junction of resistance R_0 inserted into the measurement circuit. Since $r_C << R_0$, the backside resistance r_C is neglected. Incident current: $I_0 = I_B + I_C$. The resistance r_B represents the spreading resistance due to the annular geometry for colecting the I_B current under vacuum. At zero bias the leak current $I_C = r_B / R_0\,I_B$ determines the lower limit of transmission $T = I_C / I_0 = r_B / R_0 / (1 + I_C / I_B) \approx r_B / R_0$.

- Transmission dependent components. Using propagation error formula, it can be shown that both the transmitted current I_C and the absorbed current I_B being proportional to the incident current I_0 undergo fluctuations due to the shot noise and

vary as $(3.2 \times 10^{-26} T^2 + 3.2 \times 10^{-26} T)^{1/2}$ A/(Hz)$^{1/2}$. Therefore one can expect that both T contributions referred as source noise will not be preponderant for low values of transmission (less than 0.05 pA/(Hz)$^{1/2}$ for $T < 10^{-1}$) .

3) Noise introduced by the measuring instruments.

To measure the currents I_C and I_B under high voltage bias, a dedicated picoammeter has been worked out in our laboratory. It has two stages electrically insulated up to 5 kV via an optical coupler ISO100. In the first stage the input current flows through the feedback resistance of 100 MΩ of a low noise operational amplifier OPA111, whose power supply is provided by a battery to get rid of the 50 Hz noise. The inverting terminal of the op-amp is connected to the voltage V_{sample} applied to the sample. The second stage provides a voltage amplification to visualize the signal either with a bandwidth of 2 kHz or with a filtered output of 10 Hz. Three main sources of noise can be distinguished in the detection chain: the Johnson noise coming from the feedback resistance of 100 MΩ, which is 0.013 pA/(Hz)$^{1/2}$, the voltage noise and the current noise of the detection chain (amplifier and junction). The last part is negligible (8 fA/(Hz)$^{1/2}$) considering the OPA111 electric characteristics. On the contrary, the voltage noise, which depends on the ratio of resistances 100 MΩ / R_P gives a current noise of 0.15 pA/(Hz)$^{1/2}$ considering the voltage noise of the OPA111 itself of 15 nV/(Hz)$^{1/2}$ and a junction resistance $R_0 = 100$ kΩ. Actually the value of the voltage noise determined experimentally with a 100 kΩ junction resistance is found equal to 0.8 pA/(Hz)$^{1/2}$. Note that this value is of the same of magnitude as the Johnson noise produced by a junction of 100 kΩ.

Taking into account all the noise contributions, we can draw the variations of the fluctuations of I_B and I_C as a function of the transmission T. Looking at the I_C fluctuations calculated as an example in Figure 2.17, we conclude that the Johnson noise of the junction mainly drives the current fluctuations in a large range of transmission. At high transmission the T dependent terms contribute to hamper the accuracy of the current measurements. The

same conclusion prevails for I_B current. One can also assert that a junction resistance R_P of several orders of magnitude smaller than the feedback resistance of the amplifier will increase the voltage noise, which is detrimental for the accuracy in the current measurements.

II.3.5 Instrumental asymmetries.

Spin dependent asymmetry $A = \Delta T / 2T$ is expected to be about 10^{-3} at least at low injection energy. Therefore residual instrumental asymmetries have to be kept below this value. Looking at our experimental procedure, we have identified two sources of asymmetries. One is linked to the optical modulation between σ^+ and σ^- polarizations. Such an optical polarization is achieved by an optical modulator, a transverse Pockels cell, which operates at 1 KHz (square voltage modulation) between + 280 V to – 280 V. It is necessary to achieve accurate circular polarizations and above all to have perfect symmetry between σ^+ and σ^-. Controlling the alignment procedure of the Pockels cell, we are able to control the differences of light intensities between σ^+ and σ^- at best in the range 10^{-4}. In this condition, by measuring the base current I_B, we detect an asymmetry of 4×10^{-4}, mainly due to the weak spatial displacement of the focused electron beam on the sample. To give an estimate, a base current of 40 nA at low injection energy gives a difference of 1 pA between the two electron spots of identical size, i.e. a variation of 10^{-5} on the absorbed current I_B and therefore at least a variation of 10^{-8} on the transmitted current I_C. In any case such a current asymmetry does not mar the ΔT signal. The other source of instrumental asymmetry occurs when reversing the magnetization of the sample by running a pulse current through the coils. The electron beam is spatially deflected after a pulse of magnetic field. So to curb such effect we turn off the electron beam, when reversing the magnetization. Actually we never modulate the magnetic field: it only help us to unambiguously identify the signature of the spin dependent signal by its change in sign and to disentangle instrumental asymmetries.

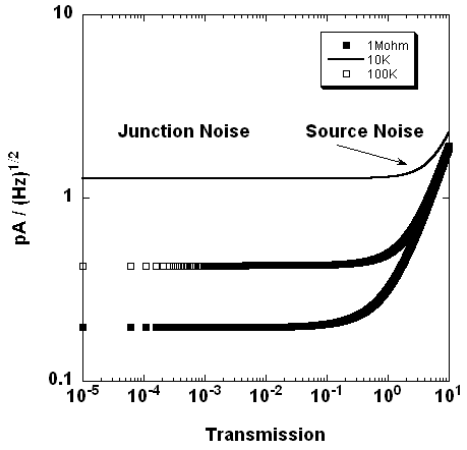

Figure 2.21: Calculated variation of the total noise attached to the transmitted current I_C versus the transmission of an incident beam of 100 nA, at room temperature and for three values of junction dynamical resistance. It is mandatory to dispose of Schottky-type samples with very high junction resistance.

II.4 Experimental results

In this section we describe the experimental results obtained on samples of different oxide barriers, when varying the injection energy of the incident electrons.

II.4.1 Spin-filter effect in the junction Pd (5 nm) / Fe (4 nm) / Uvocs (1 nm) / *n*-GaAs: sample GaAs_1 (R_0 = 160 kΩ)

We use this sample as a benchmark since it exhibits an electron transport very sensitive to the oxide barrier height and a high spin selectivity. The relevant normalized quantities to analyze the experimental data are: the transmission T, the spin-dependent transmission ΔT and the transmission spin asymmetry A, the latter characterizing the ability of the spin filter to discriminate between two opposite orientations of electron spin.

II.4.1.1 Transmission of unpolarized electrons

Figure 2.22 shows the variations of the base and collector currents and that of their sum I_0 versus the injection energy from 0 to 2 keV. The incident electrons start to enter the sample as soon their energy is equal to the vacuum barrier of the sample, i.e. for $V_{sample} = \delta\Phi$, $\delta\Phi$ being the difference between the work functions of gold electrodes of the electron optics and the metal side of the junction. In the energy range $\delta\Phi < E_0 < 100$ V, the base current is dominant $I_0 = I_B$, since the transmitted current I_C is totally negligible. As far as E_0 increases, I_B becomes zero at 630 eV, which means $I_C = I_0$ and the transmission $T = I_C / I_0$ equal to unity. Therefore we collect one electron while injecting one. At higher E_0 values, the gain in transmitted current continues to increase over 2 orders of magnitude to reach a value close of 100 (cf. Figure 2.23). This amplification process arises from the generation of secondary electron

cascade inside the metal. The transmission T varies over 5 orders of magnitude and reveals three regimes (numbered in Figure 2.23): in the low energy range up to 100 eV a linear increase in T, followed by a more pronounced increase up to 350 eV and finally an abrupt increase beyond unity. The electron transport through the metal layer can be described by an electron distribution of primary and secondary electrons. This internal electron distribution broadens in energy, when the injection energy is increased. As shown in previous theses [Rougemaille03, Lamine07], the three different regimes are associated with secondary electron multiplication (first regime) and electron crossing of two successive barriers of different heights: the Schottky barrier of 0.7 eV (E_0 > 100 eV) and the oxide barrier of 4.5 eV (E_0 > 350 eV). Electrons blocked by these barriers build up the base current I_B. For electrons having energies much higher than the last barrier, the metal / semiconductor interface is passing. At high injection energy, the slowest T variation stems from the multiplication of secondary electrons by ionization impact in the semiconductor itself. Note that the onset of transmission is 2.7×10^{-4}, which corresponds to a contact resistance r_B = 1.2 kΩ, quite much larger than the r_B value of 23.3 Ω extracted from I-V curves by three-point contact probes. It means that the sheet resistance of the metal layer is inhomogeneous.

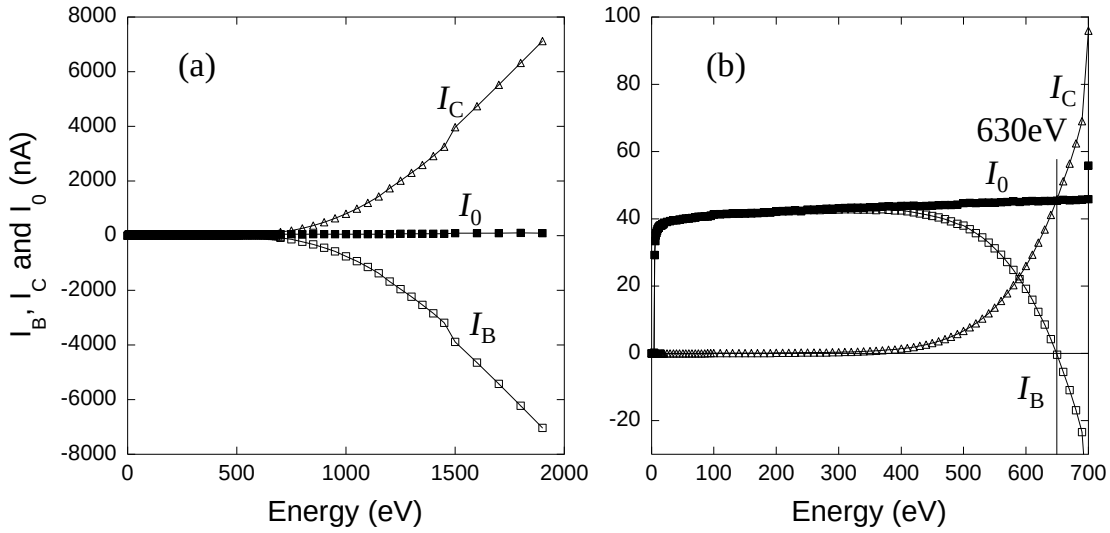

Figure 2.22: Variation of the base current I_B, the collector current I_C, and the total injected current $I_0 = I_B + I_C$ versus the injection energy E_0 for sample GaAs_1. (a) Energy scale from 0 to 2 keV; (b) Zoomed in curve up to 700eV. At 630 eV, $I_B = 0$ and $I_0 = I_C$. The conservation of I_0 is verified over a large range of E_0.

II.4.1.2 Transmission of spin-polarized electrons

To make sure of the orientation of the saturated magnetization, we apply an external magnetic field pulse of 75 Oe for 2 s along the easy axis of the sample. Then for the given orientation of magnetization, we modulate the spin polarization of the incident electron beam at 1 kHz between – 0.25 and + 0.25. The transmitted currents I_C^+ and I_C^- are respectively associated with the polarization values of + 0.25 and – 0.25. We now consider the two relevant quantities: the spin-dependent transmission ΔT, and the transmission spin asymmetry $A = \Delta I_C / (I_C^+ + I_C^-) = \Delta T / 2T$ which is the spin selectivity of the sample normalized to the incident spin polarization.

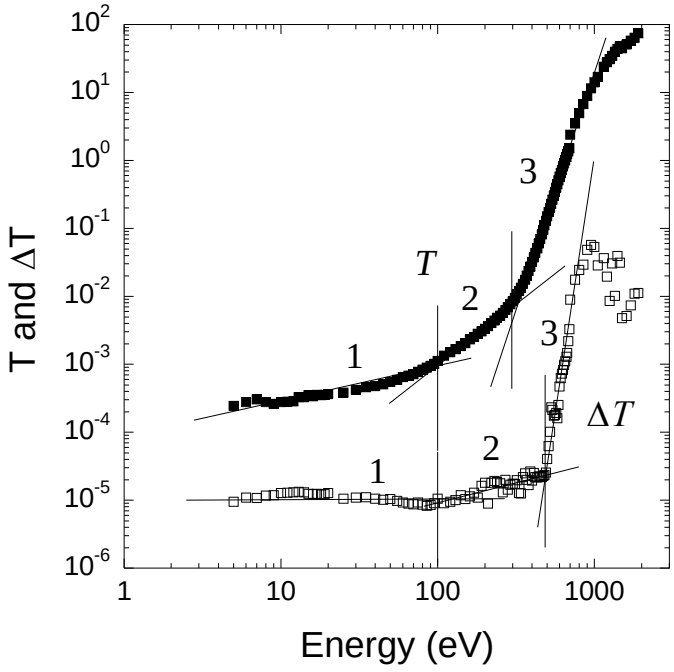

Figure 2.23: Measured current transmission $T = I_C / (I_B + I_C)$ and its spin dependence ΔT versus incident energy for sample GaAs_1. The three transmission regimes are clearly identified by plotting on a logarithm scale. From 10 eV to about 100 eV, T increases linearly, while ΔT is almost constant. From 100 eV to 470 eV, T increases by two orders of magnitude up to 1 and ΔT slowly increases. From 470 eV to 1 keV ΔT gains 3 orders of magnitude. Beyond 1 keV ΔT starts to decreases.

The spin-dependent transmission ΔT is defined as the difference of the transmitted currents I_C^+ and I_C^-, when the incident electron polarization is reversed: $\Delta T = \Delta I_C / (I_B + I_C)$, where $\Delta I_C = I_C^+ - I_C^-$. Figure 2.23 shows the variation of ΔT versus the injection energy from the vacuum level of the sample up to 2 keV. Once again, it reveals three regimes, which are shifted in energy relative to the T curve. From 0 to 100 eV, ΔT is constant. At 100 eV, ΔT slowly starts to increase but it definitively rises up at 470 eV, even faster than the variation in T (3 orders of magnitude).

Looking at the transmission spin asymmetry A (Figure 2.24), the previous three regimes are retrieved: a plateau at low energy followed by a sharp drop-off of more than 2 orders of

magnitude associated with the strong increase in T and beyond 500 eV the rise due to the sharp ΔT increase. It is worth mentioning that working at 860 eV ensures a transmission spin asymmetry of the order of 1 %. It means a spin selectivity as good as the conventional Mott detector, but with a much lower operating voltage.

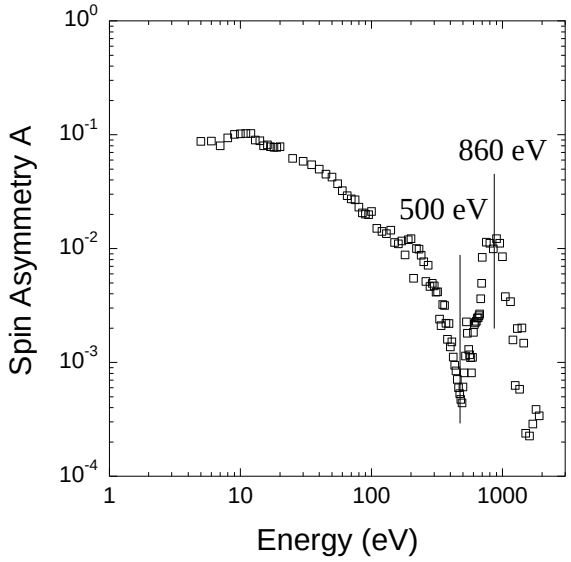

Figure 2.24: Transmission spin asymmetry A = ΔT / 2T versus injection energy for sample GaAs_1 (log. scale). Up to 470 eV, A is driven by the T variation. Minimum at 500 eV and maximum at 860 eV.

II.4.1.3 Determination of the hysteresis loop of the iron layer by electrical measurement

While flipping the spin polarization of incident electron beam from + 0.25 to – 0.25, the currents I_B and I_C are modulated. The total current conservation yields $\Delta I_C = -\Delta I_B$. The "π-phase shift" means that a decrease in I_B corresponds to an increase in I_C for a fixed incident polarization. Then the variation of I_C can be also detected via the detection of that of I_B and the ΔT measurement can be achieved by indistinctly measuring the variations in I_B or I_C. If one wants to measure the spin filter effect with a very high sensitivity, the trick is to operate at 630 eV, where I_B vanishes. In this condition, if we measure the variations of the

current I_B versus pulse amplitude of the magnetic field, we can reproduce the hysteresis cycle of the sample (see Figure 2.25). The largest variations are reached when high magnetic field pulses are applied in the configurations where the spin polarization is parallel and antiparallel to the saturated magnetization of the iron layer. Let us remark that the electrical measurement of the hysteresis cycle can also be performed by unpolarized electron beam, using the spin-valve effect or polarizing-analyzing effect. In this case, the first ferromagnetic layer polarizes the electron beam by passing a spin direction, while the second ferromagnetic layer detects the projected spin component.

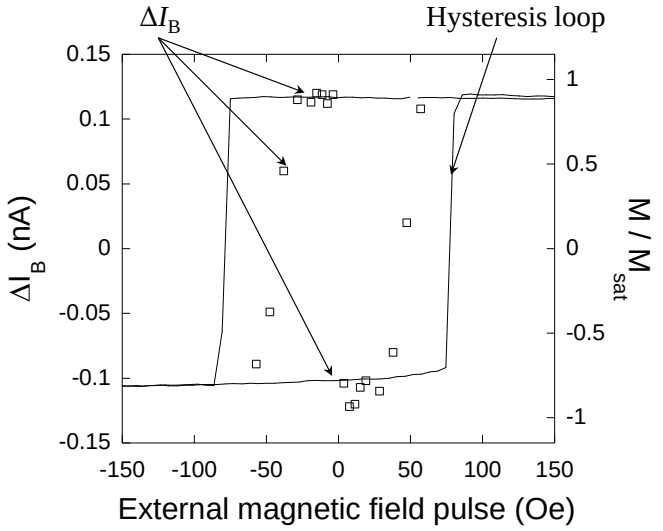

Figure 2.25: Exploiting the spin-filter effect: Electrical measurement of the hysteresis loop by measuring the spin dependent variation of the base current I_B at 630 eV (dots). The total injected current is about 46 nA (cf. Figure 2.22). External magnetic field pulses are applied to sample GaAs_1 step by step from – 60 Oe to + 60 Oe (field pulse to the saturation in reverse direction is applied before each step). Scaled magneto-optic cycle (line).

II.4.2 Spin-filter effect in the junction Pt (3 nm) / Co (5 nm) / MgO (2 nm) / *n*-Si

Let us recall that this sample has a total metal layer of same thickness than the sample GaAs_1.

II.4.2.1 Transmission of unpolarized electrons

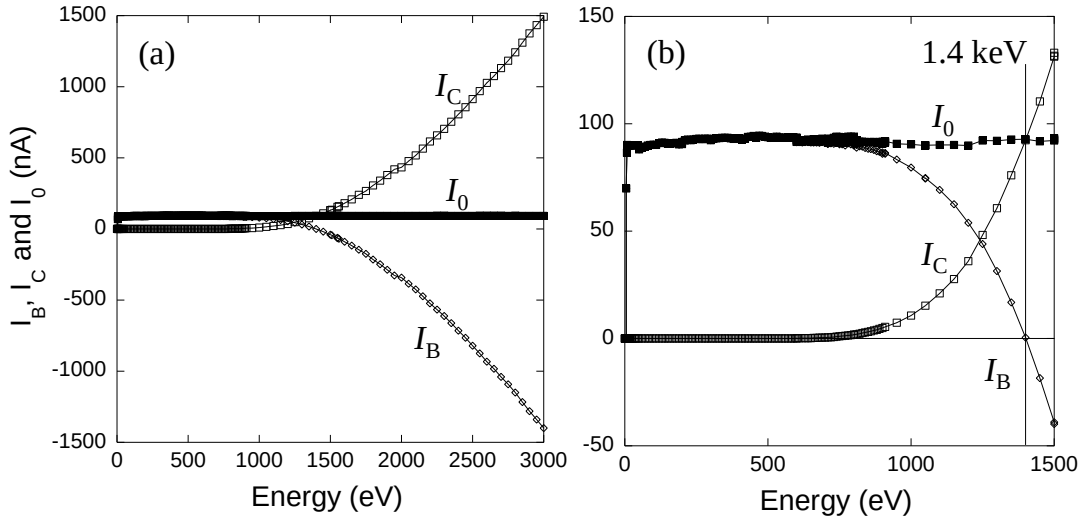

Figure 2.26: Measured currents I_B, I_C and I_0 versus energy for sample MgO_1. (a) Up to 3 keV. (b) Up to 1.5 keV. The transmitted current I_B vanishes at 1.4 keV

The variations of I_B and I_C currents are shown in Figure 2.26 as a function of the incident energy up to 3 keV. In comparison with the case of junction GaAs_1, one can conclude: i) the injection energy required to achieve a unity transmission ($I_C = 0$) takes place at much higher energy of 1.4 keV, ii) the onset of the transmission starts at 470 eV, evidencing the effect of a thicker oxide barrier (Figure 2.27-a). The transmission T varies over 5 orders of magnitude and reveals three regimes: the first one up to 470 eV, the second one between 500 eV and 700 eV over one order of magnitude and the last one steeper up to 1500 eV. The T variation in the regime 2 steps up more abruptly than the one observed in sample GaAs_1. The T variation in the regime 3 has the same slope as the third regime of sample GaAs_1. Based on the transport model developed for GaAs_1, we can interpret these two regimes as the crossing of the Schottky barrier and the oxide layer. Like for sample GaAs_1 the crossing of the Schottky barrier needs 250 eV to be completed. The minimal transmission value of 8×10^{-5} corresponds to an access resistance of 1 Ω. In final at 3 keV this sample has an electron gain

of 17, i.e. 17 electrons collected for one incident.

II.4.2.2 Transmission of spin-polarized electrons

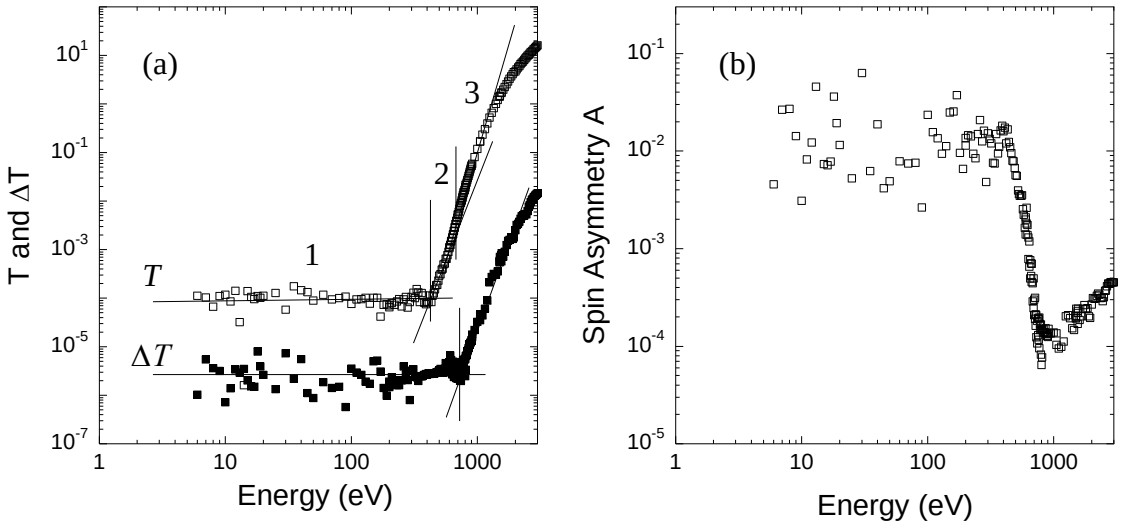

Figure 2.27: a) Measured current transmissions T and ΔT for sample MgO_1. b) Transmission spin asymmetry A = ΔT / T versus the injection energy.

The variation of the spin dependent transmission ΔT only reveals two regimes (Figure 2.27-a). At low injection energy ΔT is constant and equal to 1.2×10^{-6}. Beyond 800 eV, ΔT increases over almost 4 orders of magnitude with the same slope as the T slope.

The transmission spin asymmetry is reproduced Figure 2.27-b. It starts to decrease at 500 eV over 2 orders of magnitude to reach a minimum at around 1000 eV. However, unlike the case of sample GaAs_1, the maximum of the asymmetry is not attained, showing that the crossing over of the MgO barrier height is not completed at 3 keV. At 3 keV only a variation of 1 order of magnitude is obtained. Notice that for sample GaAs_1 the increase in A occurs over 2 orders of magnitude before going through a maximum.

II.4.3 Spin-valve effect in the junction Pt (2 nm) / IrMn (7.5 nm) / Co (5 nm) / Cu (3.5 nm) / Co (5 nm) / MgO (3 nm) / *n*-Si (MgO_2 sample)

The junction of this sample is thicker (26 nm) than that of the previous one (10 nm) with the same type of oxide barrier. So we expect a weaker transmitted current.

II.4.3.1 Transmission of non polarized electrons

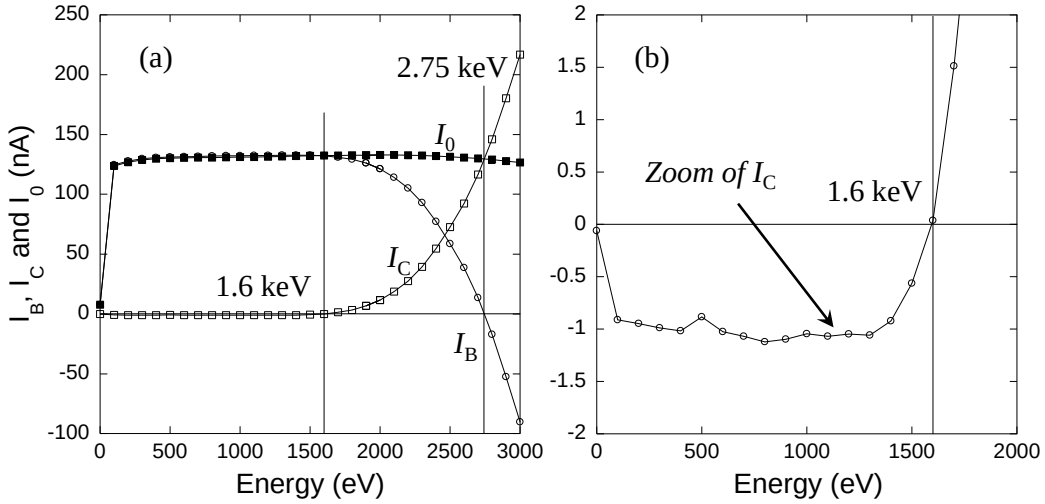

Figure 2.28: (a) Measured currents I_B, I_C and I_0 versus incident energy for sample MgO_2 and (b) I_C zoom in the energy range up to 2 keV. The onset of the transmitted current I_C occurs at 1.6 keV. I_B vanishes at 2.75 keV. The magnetic configuration is on the parallel state. Zoom in of I_C, showing the negative transmitted current below 1.6 keV.

The base and collector currents I_B and I_C are drawn as function of injection energy in Figure 2.28 for parallel saturated magnetizations in both Co layers. The current I_C starts to step up at 1.6 keV. As expected the current I_C is quite low: at 3 keV it is equal to 220 nA, a value which was reached in the sample Mgo_1 for an injection energy of about 1700 eV. The unity transmission is obtained at 2750 eV. At 2450 eV the transmission is 0.5 (cf. Figure 2.28-a), which means an attenuation of a factor 10 with respect the sample MgO_1 at the same energy. However the most intriguing feature is the negative sign of the current I_C

before changing sign at 1600 eV. The corresponding transmission is -7.5×10^{-3} (Figure 2.28-b). The negative sign of I_C means that the electrons are actually coming out of the Si collector, when incident electrons enter the front layers. A possible scenario to explain the blockage of transmitted electrons is the trapping of the incoming electrons *above the metal Fermi level* at the metal / semiconductor interface or within the MgO band gap. In this case a negative charge builds up on the entrance side of the insulator attracting holes on the other side. It is equivalent of having an effective negative bias at the metal side: the valence band and conduction band edge bend upward near the surface allowing the tunneling of either electrons from the Si conduction band to the metal or holes from the metal to the Si valence band. The fact that the I_C current remains constant up to 1.6 keV tends to say that it is probably the minority current which tunnels: the current is limited by the rate of supply through the *n*-type semiconductor, like the saturation current in a *p*-*n* junction.

II.4.3.2 Spin-dependent transmission of unpolarized electrons.

Injecting unpolarized electrons across a spin valve structure is equivalent of performing a coupled experiment of spin polarizing and spin analyzing of the travelling electrons. Each ferromagnetic layer can be characterized by its spin discriminating power, which is the polarization acquired by unpolarized electrons when passing through the spin filter. A perfect spin-valve effect (unity discriminating power for each ferromagnetic layer) would yield a zero transmitted current in antiparallel (AP) states in order to achieve the extinction condition. The experiment consists in measuring the difference in transmitted currents I_C for the two saturated magnetization configurations: parallel (P) and antiparallel (AP), the latter corresponding to zero magnetization (cf. hysteresis loop in Figure 2.9). The resulting transmissions are shown in Figure 2.29. The two curves are measured after applying external magnetic field pulse of amplitudes of 70 G either parallel or antiparallel to the direction of the easy axis of the sample to attain the P and AP configurations respectively. The difference of

transmission is always positive, meaning that the largest transmission is obtained in the parallel configuration and increases to reach 0.1 at 3 keV. It can be shown [Cacho02] that the asymmetry in transmitted currents I_C between P and AP states $(I_C^P - I_C^{AP}) / (I_C^P + I_C^{AP})$ yields directly the value of the product of spin discriminating power of each ferromagnetic layer. We found a value of 3 % above 1.6 keV, which indicates that the poor spin selectivity of our sample does not meet at all the criteria of a high-efficiency spin polarimeter, at least in this energy range. We recall that asymmetric ferromagnetic cobalt bilayer such as Au (18 nm) / Co (0.8 nm) / Au (2.2 nm) / Co (1.3 nm)/ Au (1.5 nm) gives a value of 70 % at very low injection energy (typically 4 eV above the Fermi level).

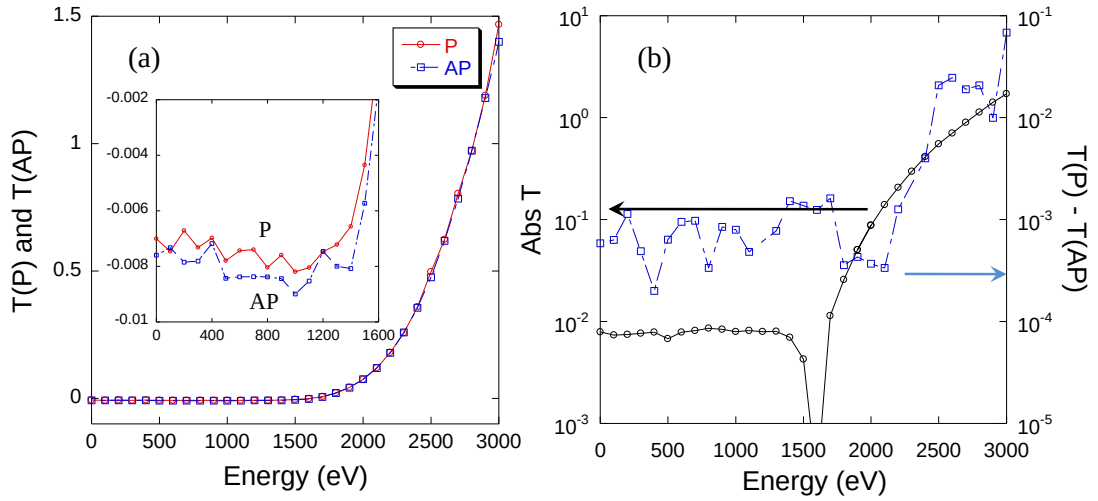

Figure 2.29: (a) Transmissions of unpolarized injected electron beam in P and AP configurations versus the injection energy for the junction MgO_2 in linear scale from 0 to 3 keV. Insert: Zoomed in scale from 0 to 2keV. (b) Difference between the transmissions in P and AP configurations and the transmission $T = I_C / I_0$.

We have tried to measure the transmission asymmetries of a polarized beam between two magnetic states + P and – P at 3 keV, the latter – P state being reached by applying magnetic field amplitude of 200 G according to the hysteresis loop. As expected the difference in transmitted currents I_C is not significant enough for reliable analysis.

III.4.4 What to conclude from the transmission experiments?

Let now see whether we can extract some common features in the transmissions curves for the different junctions. The table sums up all the energy values, for which the crossing of the Schottky barrier, the transport over the oxide barrier and the unity transmission are achieved (Table 2.1).

Table 2.1 Energy values necessary for crossing barriers

Samples (junction thickness)	E_0 for over Φ_B	E_0 for over Φ_{Oxide}	E_0 for T =1
GaAs_1 (10 nm)	100 eV	350 eV	630 eV
MgO_1 (10 nm)	470 eV	750 eV	1400 eV
MgO_2 (26 nm)	2400 eV	X	2750 eV

- A first remark can be made concerning the last column for the first two samples of equal metal thickness (metal cap layer + Co layer). A unity transmission means one entering electron produces one transmitted electron via the generation of secondary electrons. The property of secondary emission is the total yield, i.e. the total number of electrons emitted per incident primary electrons as a function of the energy of the incident primaries. It is known that the yield reaches its maximum value for the characteristic energy E_S depending upon the atomic number. Looking at the E_S values reported in the literature [Dekker58] there is a ratio of 2.4 between the metal Pd (top layer of GaAs_1) and the metal Pt (top layer of MgO_1). It is the same ratio as the energy ratio 1400/630 experimentally found. Increasing the thickness of the metal layers means an increase in the escape depth of the secondary electrons and a shift of E_S towards the high energy range. Also the value of 2750 eV for MgO_2 can be considered as an averaged electron yield of the different materials composing MgO.

- Second comment, which can be made: samples GaAs_1 and MgO_1 have the same thickness of metal layers, similar Schottky barrier heights of 0.71 eV and 0.63 eV. It means that the internal electron distribution has the similar energy distribution when reaching the oxide interface. However, the crossing of the Schottky barrier through the oxide layer does not occur at the same energies. We need to go over almost 500 eV to observe such a crossing in sample MgO_1. Therefore it is the convincing signature of the MgO barrier, which is thicker and might be denser with less defect densities. Note that about 250 eV are necessary to complete the transport over the Schottky barrier in both materials. Unfortunately from our experimental results we cannot deduce the height of the MgO barrier, which is 3.6 eV for an ideal MgO tunnel barrier, less than the 4.5 eV of Uvocs layer obtained by the transport model in sample GaAs_1.

- The last comment concerns the high energy regime linked to the ionization impact observed in the semiconductor of GaAs. Such a mechanism depends on the energy gap of the semiconductor. Therefore it is expected that it should be much efficient in Si than in GaAs, since the band gap of Si is lower.

Electrical detection of the transmission basically relies on the rectifying behavior of the metal / semiconductor interface. Also the most important parameter for this junction is the metal-insulator barrier height and the chemical composition of the interface due to the thermal oxidation. All parameters affect the ideal metal / semiconductor characteristics. So the ability to readily tailor the Schottky barrier is an elusive goal to pursue and it is out of scope of this thesis. An alternative approach to study the electrical spin injection and the spin-dependent transport is to take advantage of one of the intrinsic properties to the semiconductor, which is the radiative recombination of carriers and the consequent light emission. We know that the spin-polarized light emitting diode or spin-LED provide a quantitative measure of the electron spin polarization in the semiconductor [Fiederling99, Ohno99, Zhu01]. The primary advantage of performing optical detection of electron injection is to get rid of the need of

having very high junction impedance. Moreover through the electron-photon conversion we avoid the difficulty of measuring very low currents under high voltage. So one of the objectives of the next chapter will consist in investigating the cathodoluminescence experiments on structures combining ferromagnetic metal / semiconductor junctions.

Chapter III

Optical detection of spin-filtering effects in ferromagnetic metal / semiconductor junction

---

We present a cathodoluminescence experiment, where the transmission of spin-polarized electrons through a ferromagnetic metal / semiconductor junction is detected by measuring the light emitted from the recombination of the transmitted electrons with holes in the semiconductor collector. Departure with respect to the electrical detection of electron transmission is observed in the variation with injection energy of both the overall electron transmission and the spin-filtering effect.

This chapter aims at investigating the transport of spin-polarized hot electrons in ferromagnetic metal / semiconductor junctions by detecting the light emitted from the recombination of the collected electrons with holes in the semiconductor.

The detection of the luminescence is a usual tool used in spintronic devices such as spin-LED (Light Emitting Diode) to study the injection of spin-polarized electrons from a ferromagnetic metal into a semiconductor. In such devices, electrical electron injection requires to design a specific junction which basically consists in a MIS structure with a thin oxide interfacial layer which allows electron tunneling from the metal into the semiconductor under reverse-bias operation of the junction. Such a tunneling process helps overcome the resistance mismatch between the semiconductor and the ferromagnet to get a successful spin injection. Then, the use of an optical detection technique does not introduce any additional requirements on the electrical properties of the junction and is thus not limiting for the spin injection properties of the device.

To that respect, our experimental approach presented in this chapter is similar although it is based on different criteria. We study hot-electron transport and as previously explained we want to free ourselves from the requirements on the quality of the rectifying properties of the metal / semiconductor junction which provides limitations on the electrical detection of weak transmitted currents. We expect that the optical detection of the collected electrons will allow us to overcome these limitations and to achieve the measurement of spin-filtering effects even through an abrupt metal / semiconductor interface with poor rectifying character.

III.1 Ferromagnetic metal / semiconductor structure for cathodoluminescence

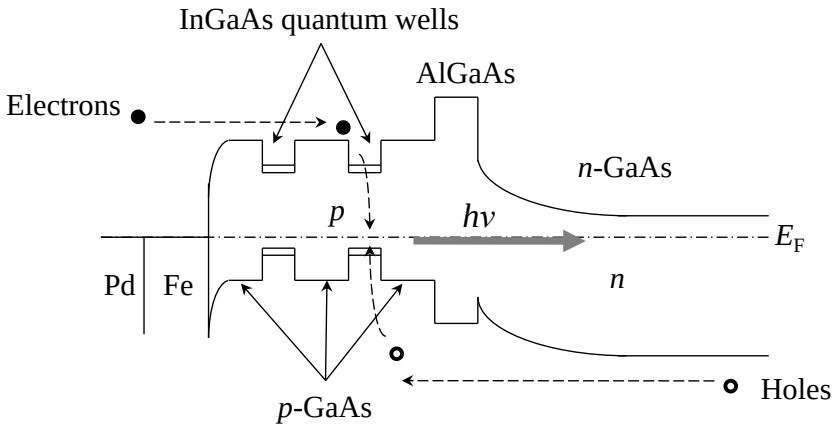

Figure 3.1: Structure of the GaInAs_1 junction: Pd (2 nm) / Fe (4 nm) / p-GaAs (20 nm) / p-$In_{0.18}Ga_{0.82}As$ (10 nm) / p-GaAs (20 nm) / p-$In_{0.18}Ga_{0.82}As$ (10 nm) / p-GaAs (20 nm) / p-$Al_{0.3}Ga_{0.7}As$ / GaAs:Si (100 nm) / n^+-GaAs epi-ready. The InGaAs layers constitute the quantum wells. The cathodoluminescence (CL) process which provides electron-photon conversion is schematized. The electrons are injected in the metal layers and the light emission due to the electron-hole recombination in the QW's is transmitted through the GaAs substrate and detected at the sample back side.

In this section, we will describe and characterize the device structure, hereafter referred as InGaAs_1, dedicated to cathodoluminescence experiments. The whole structure composition is schematized in Figure 3.1. The structure of the semiconductor collector is designed specifically to allow cathodoluminescence measurements in transmission geometry, i.e. through the collector substrate. The optically active region consists of two 10 nm thick InGaAs quantum wells (QW's) limited by 20 nm thick GaAs barriers. The conversion of transmitted electrons into photons occurs in the quantum wells. The $In_{0.18}Ga_{0.82}As$ band gap is close to 1.18 eV, as estimated from the work of Porod *et al* (1983) [Porod83], smaller than the GaAs direct gap of 1.42 eV. The electron transmitted through the metal layer recombine in the QW's producing light of energy smaller than the GaAs substrate bandgap which can be detected on the back side of the sample. An AlGaAs layer provides a potential barrier which

keeps the injected electrons in the optically active region and allows to improve the QW's luminescence efficiency. The AlGaAs layer is grown on an epitaxial Si-doped GaAs buffer layer. The substrate is a commercial wafer of n^+-doped GaAs which insures an ohmic back contact on the metallic sample holder. The structure of the semiconductor collector ends up with a GaAs layer. Well controlled epitaxial growth of iron can indeed be achieved on (100)-GaAs [Tereshchenko11]. The (100)-oriented GaAs surface was chemically treated in HCl-isopropanol solution to remove native oxides and then annealed at 550 ℃ to obtain Ga-rich (4×2) surface before Fe deposition [Tereshchenko99]. The deposition of the metal layers is carried out in our laboratory in an ultra-high vacuum chamber separated from the cathodoluminescence set-up. The growth conditions are similar to those used for the GaAs_1 sample preparation described in Chapter 2. A 4 nm thick Fe layer is grown at room temperature covered by a 2 nm thick Pd layer. As shown in many previous studies (see for instance [Filipe97]) Fe grows epitaxially on the (100) GaAs surface and the magnetization of a thin Fe layer has the same value than that of a bulk slice of same thickness [Tereshchenko11].

We will now present the electrical, magnetic and optical properties of our sample prior to the cathodoluminescence experiment.

III.1.1 Electrical characterization

The I-V characteristics of the InGaAs_1 junction are measured *in-situ* under high vacuum in the dark with a front contact on the Pd top layer and an ohmic back contact on the n^+-doped GaAs substrate.

Our sample actually combines a Schottky barrier on the front side (metal layer on the *p*-type GaAs) in series with a *p*-*n* junction. Knowing the respective doping levels of the *n*-side (2×10^{18}) and of the *p*-side (7×10^{17}), we calculate a built-in potential of 1.34 V for an abrupt

p-n junction, which corresponds to a depletion layer width of 60 nm. The equivalent circuit of this two-junction structure is two diodes connected back to back. Because of the high doping levels in the semiconductor structure, the two junctions have a poor rectifying character with no saturated current under reverse bias. This allows the current flow in both bias directions as seen in the I-V curve (a) of Figure 3.2. Positive bias applied to the metal layer corresponds to the forward regime of the *p-n* junction and to the reverse regime of the Schottky junction formed at the Fe / *p*-GaAs interface. From the slope of the I-V curve at zero bias, we extract the value of about 12 kΩ for the dynamic resistance linked to both junctions. This value is much smaller than the usually required values for electrical detection of electron transmission.

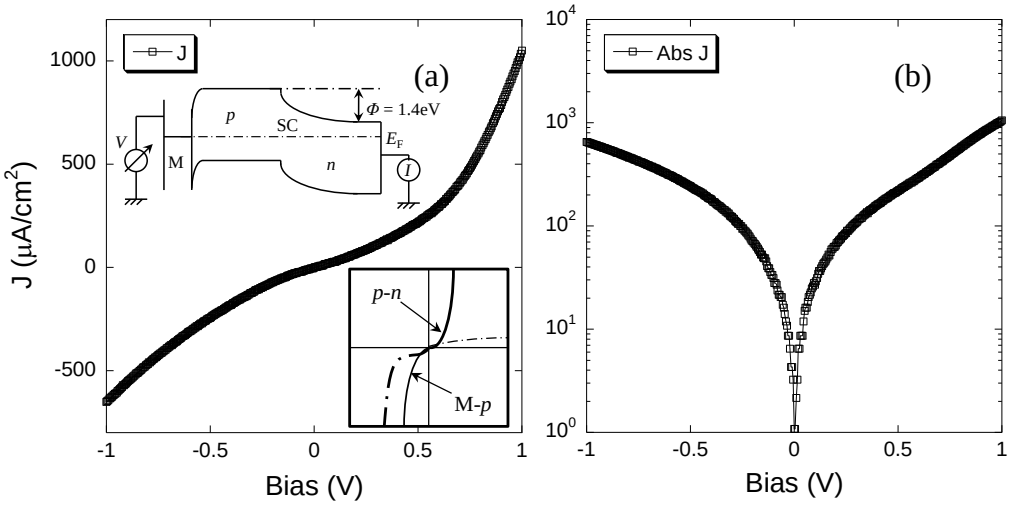

Figure 3.2: IV curves of sample InGaAs_1. Insert: Band structure of the p-n junction. Φ is the built-in potential of the p-n junction at zero bias. (a) Current density versus voltage bias; Note that the p-n junction and the Schottky junction are biased in opposite directions. (b) Absolute current density in logarithm scale versus voltage bias. R_P = 4 kΩ, R_0 = 11.75 kΩ and R_s = 1.4 kΩ. (All the values are calculated from the raw data, since the thermionic-emission theory is not appropriate in this case.)

III.1.2 Magnetic characterization

The magnetic characterization of junction InGaAs_1 is performed in air by MOKE

(Magneto-optic Kerr Effect) measurement with a scanning frequency of 0.1 Hz of the magnetic field applied along the in-plane easy axis (see Figure 3.3). It can be directly compared with the one of the GaAs_1 junction, measured in the same conditions. The squared hysteresis loop gives a coercive field of 25 Oe, much smaller than that of GaAs_1 sample (70 Oe). This difference may be attributed to different phenomena like:

- the difference in the Fe growth on the GaAs surface of sample InGaAs_1 with respect to the Fe growth on the Ga_2O_3 surface of the GaAs_1 substrate;
- the difference in the surface roughness;
- the difference in the thickness of the Pd layer.

However, calibration of the absolute magnetization shows comparable values for the 4 nm thick Fe layer of both samples.

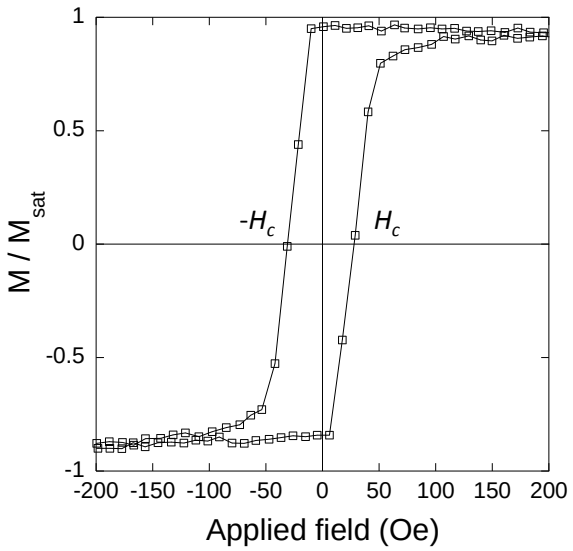

Figure 3.3: Magnetic hysteresis loop of the GaInAs_1 sample. The magnetic field is applied along the direction of the in-plane easy axis at a scanning frequency of 0.1 Hz. The coercive field H_c is 25 Oe.

III.1.3 Optical properties

The optical properties of our sample are characterized by photoluminescence (PL) spectroscopy. We performed these experiments in air at room temperature on the semiconductor structure prior to the deposition of the metal layers. We have used four different measurement configurations. First, the excitation beam is shined onto the front side of the semiconductor structure and the PL spectrum is measured either on the same side (reflection (R) mode) or on the back side through the semiconductor substrate (transmission (T) mode). The front side excitation addresses the QW's region and the comparison between reflection and transmission geometries will allow us to evaluate the efficiency of the detection of the QW's luminescence through the GaAs substrate which corresponds to the cathodoluminescence measurement configuration. Then, the laser beam is shined onto the semiconductor substrate and the PL spectrum is measured both on the same side (Reverse Reflection mode) and on the opposite side (Reverse Transmission mode). These two geometries allow to isolate the contribution of the substrate to the photoluminescence spectrum.

We have also performed experiments with different excitation wavelengths, 378 nm (3.28 eV, UV light), 532 nm (2.34 eV, green), and 660 nm (1.88 eV, red) in order to identify the contributions of the different regions of the structure to the luminescence spectrum. Indeed, the light intensity I decreases exponentially with depth x inside the semiconductor: $I = I_0 \exp(-\alpha x)$, I_0 being the light intensity transmitted at the air / semiconductor interface. The absorption coefficient α depends on the wavelength: the absorption is much higher for short-wavelength light than for long-wavelength light. So, in the R-mode photoluminescence experiment, UV light is mainly absorbed in the QW's region while visible (red and green) light deeply penetrates inside the structure up to the n^+ substrate. This is illustrated in Figure 3.4, where the variation of I / I_0 is reported relative to the distance from the sample surface. The calculated light attenuation profile plotted here is performed for bulk GaAs.

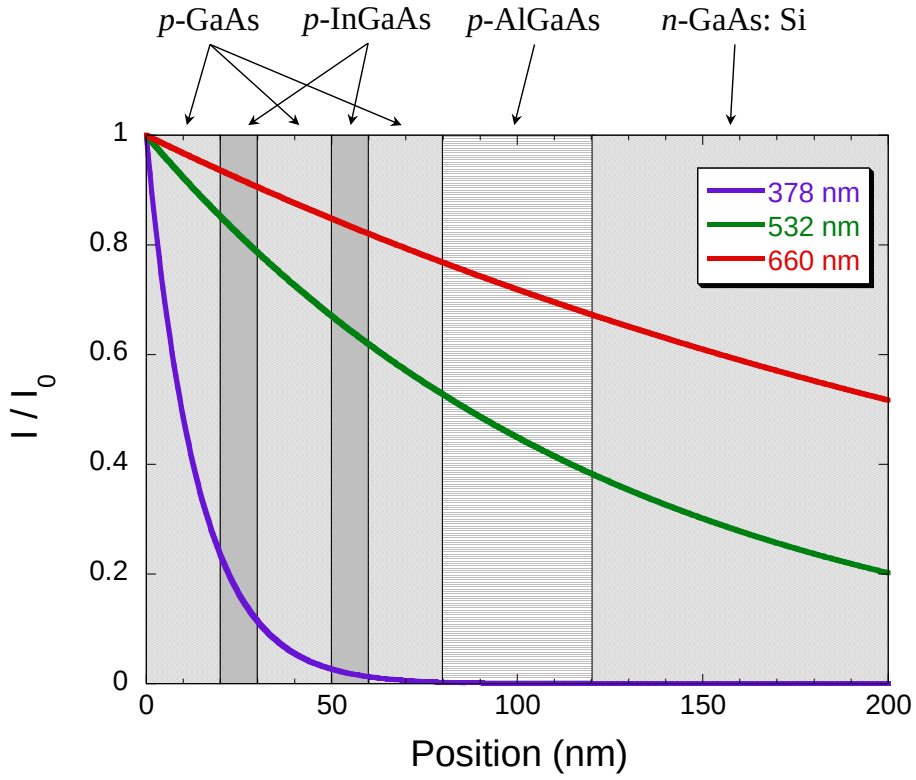

Figure 3.4: Attenuation of the excitation light in the InGaAs_1 structure for different wavelengths. For UV excitation (378 nm), most of the light is absorbed before hitting the second GaAs layer. For green (532 nm) and red (660 nm) excitation, light penetrate up to the n-GaAs substrate. Here the attenuation is calculated by considering the whole sample as a pure GaAs crystal.

The PL spectra measured in reflection geometry (R mode) for the three excitation wavelengths are plotted in Figure 3.5. With red light excitation, three luminescence peaks are observed. The peak at 984 nm (1.26 eV) originates from quantum wells (QW's). The peak at 870 nm (1.43 eV) corresponds to the recombination at the GaAs bandgap. The broad structure centered at 1070 nm (1.16 eV) corresponds to the emission from the heavily doped GaAs substrate. This is confirmed by the spectra obtained with larger excitation energies. For green light, the intensity of the peak at 984 nm increases with respect to the intensity of the peaks at 870 nm and 1070 nm, and for UV excitation only the peak at 984 nm is observed. As already discussed, when increasing the excitation energy, the absorption length decreases and for UV excitation light is almost fully absorbed in the QW's region so that no luminescence from the

GaAs substrate is observed. Note also that the GaAs layers which limit the quantum wells do not contribute to the luminescence spectrum which means that conduction electrons excited ahead of the AlGaAs layer all recombine in the QW's. So, in the cathodoluminescence experiment, electrons transmitted through the metal and injected into the semiconductor should be efficiently trapped and recombined in the QW's. Moreover, the photoluminescence spectra measured in the transmission geometry (T mode) for both red and green excitation energies do not exhibit the peak at 870 nm since the GaAs substrate acts as a high-pass filter in wavelength with a cut-off at 900 nm, but the QW's luminescence peak at 984 nm has an even larger intensity than in the reflection geometry. Thus, light emitted from the recombination in the QW's can be efficiently transmitted through the substrate and detected in the transmission geometry which corresponds to configuration of the cathodoluminescence set-up.

In the RR mode photoluminescence spectrum only exhibits the GaAs substrate contributions centered at 870 nm and 1070 nm. In this configuration we do not observe the QW's luminescence peak, since excitation light have not reached the QW's layers. The broad structure at high wavelength (around 1070 nm) comes from the recombination on deep donor levels of the n^+-substrate. This broad structure of energy smaller of the bandgap width of all the layers is the only contribution that remains in the RT mode spectrum while the 870 nm peak is not transmitted.

Finally let us mention that the QW's bandgap energy is 1.19 eV while the QW's luminescence peak singled out with UV light excitation in the R mode is centered at 984 nm, which is 1.26 eV, with a full-width at half maximum 37 meV. It is the signature of electron-hole recombination between the first quantized conduction level and the quantized heavy-hole level. One notices a peak shoulder at low wavelength located around 940 nm (1.31 eV), which might be attributed to the recombination from the second conduction quantized level.

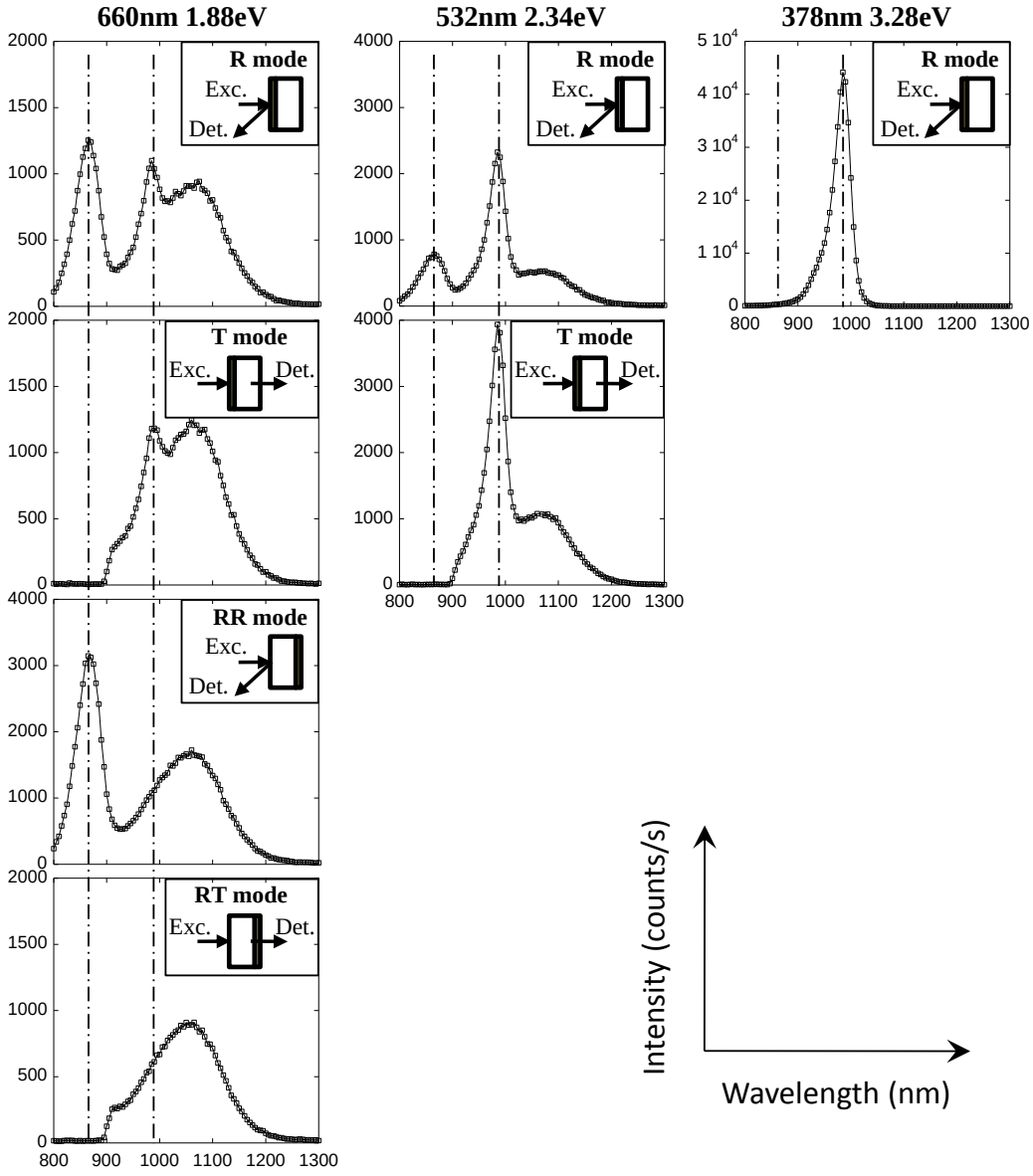

Figure 3.5: Photoluminescence (PL) spectra of the junction InGaAs_1 obtained (a) with red excitation (660 nm or 1.88 eV, 2.3 mW) (b) with green laser (532 nm or 2.33 eV, 10 mW) and (c) with UV excitation (378 nm or 3.28 eV, 7 mW). For each spectrum an inset shows the measurement geometry with respect to the sample structure, the dark area on the sample schematics indicating the QW's position. The different measurement geometries are labeled R for reflection mode, RR for reverse reflection mode, T for transmission mode, RT for reverse transmission mode. The peak at 984 nm (1.26 eV) originates from quantum wells (QW's). The peak at 870 nm (1.43 eV) corresponds to recombination in GaAs. The broad structure centered around 1070 nm (1.16 eV) corresponds to the emission from the heavily doped GaAs substrate.

III.1.4 Electrical detection of electron injection and transmission in the InGaAs_1 junction

Considering the band structure of the sample, one consequence of having electron injection in a *p*-type GaAs semiconductor is that the effective potential barrier that the electrons must surmount in order to be collected into the semiconductor when coming from the metal is equal to the GaAs band gap width, which is 1.42 eV at room temperature. This effective barrier is larger than the Shottky barrier height of the order of 0.7 eV seen by the electrons at the metal / *n*-type semiconductor interface in the samples studied in the previous chapter. It is thus expected to obtain lower electron transmission. However, the absence of interfacial oxide layer should increase the electron transfer probability from the metal into the semiconductor. Moreover, the Pd cap layer is thinner on the GaInAs_1 sample than for instance on the GaAs_1 sample, and this should favor electron transmission.

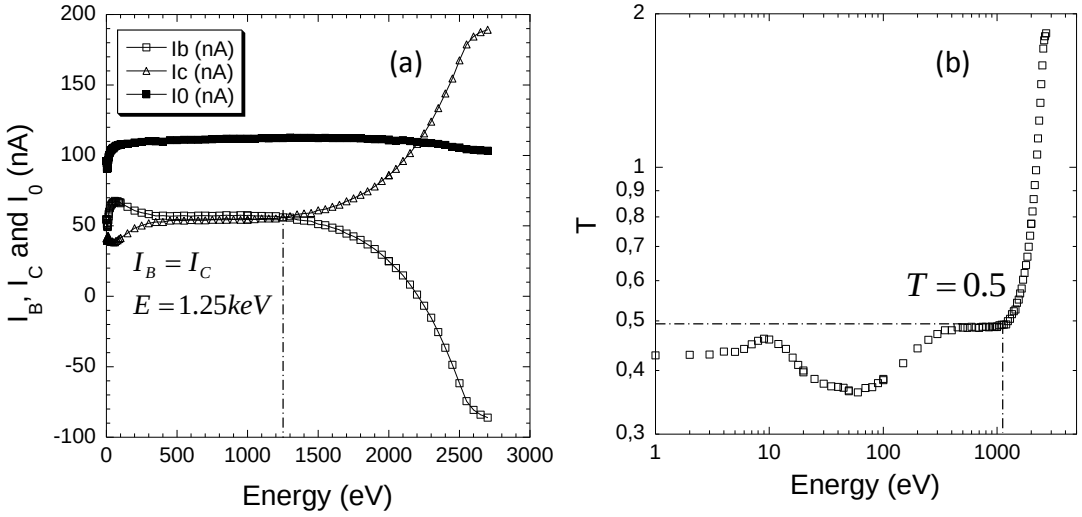

Figure 3.6: Injection and transmission of unpolarized electrons through the InGaAs_1 junction. (a) Variation of the metallic base current I_B, the collector current I_C, and the injected current I_0 (total current) versus electron injection energy. (b) Electron transmission versus electron injection energy in logarithmic scale. Note the high value of T at low injection energy.

We have first used the electrical detection technique to measure the electron transmission through the GaInAs_1 structure. In this experiment, electrons are injected into the metal side of the junction, the base current and the collector being simultaneously measured. Figure 4.6 (a) shows the variation of the injected current I_0, the metal base current I_B and the collector current I_C as a function of the injection energy. Surprisingly a large collector current is detected which corresponds approximately to half of the incident electrons. This value is almost constant from the very low injection energy range right from the injection threshold, i.e. the surface work function, up to about 1200 eV. Considering the access resistance r_B which is usually of the order of 10 Ω and the dynamical resistance R_0 of the structure extracted from the I-V curve which is of the order of 10 kΩ, we estimate the value of the parasitic transmission (which gives the lower limit of the measurable transmission) of about $10 / 10^4 = 10^{-3}$. This value cannot explain the actually measured transmission of 5×10^{-1}. Since the offset current is as large as half of the injected current and almost constant with injection energy, it is very improbable that it is due to direct injection of electrons into the semiconductor collector through pinholes in the metallic layer. This will be confirmed by the cathodoluminescence experiment. Considering the geometry of our experimental setup, it is also hardly conceivable that this parasitic collector current is due to a leakage current directly collected on the back side of the sample. At this stage, we can only assert that an unusually large offset of collector current prevails at low injection energy up to about 1 keV, which is only detected when electrons are injected in the metallic base. But we are unable to conclude where this offset comes from.

The high value of I_C which results in a quite large and constant transmission of about 0.5 in the low injection energy range is followed by a modest increase above 1.5 keV of injection energy (cf. Figure 3.7). However, above 2 keV, the collected current becomes larger than the injected current and the base current becomes negative. This strongly indicates that electrons indeed pass through the metallic base where they relax their energy by excitation of a

secondary electron cascade before being collected into the semiconductor. At 2500 eV, which is the highest injection energy used in this experiment, the transmission reaches the value of 2. By comparison, in sample GaAs_1, transmission reaches a value of 2 for an injection energy of only about 700 eV and is as large as 100 at 2 keV (see Chapter 2). So, in the sample GaInAs_1, transmission measured by the usual electrical detection technique is found to be orders of magnitude smaller than in any other samples studied up to now. This difference could partly be related to the higher barrier given by the GaAs band gap in the *p*-type collector but, as already discussed, other sample characteristics should favor electron transmission so that the weak actual values of the transmission are not understood.

When injecting spin-polarized electrons, a spin-dependent transmission signal is hardly detected only for injection energies larger than 1500 eV [Figure 3.7 (a)]. It corresponds to a spin asymmetry in the transmitted current of the order of a few 10^{-3} [Figure 3.7 (b)]. The uncertainty on these results is large. A signal-to-noise ratio larger than one could indeed hardly be obtained on these measurements.

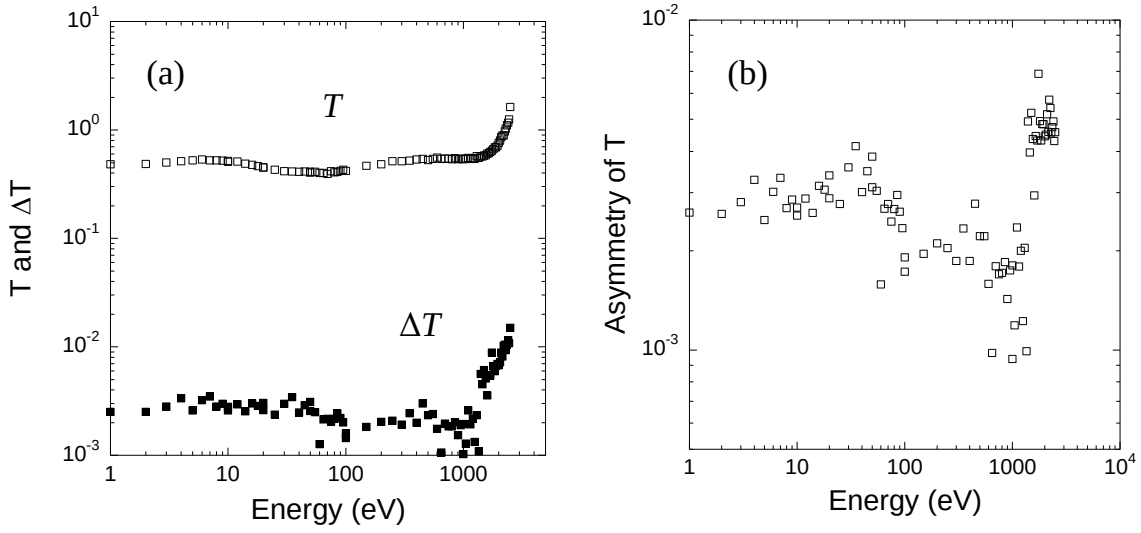

Figure 3.7: Spin-dependent electron transmission in junction InGaAs_1 versus injection energy. (a) Transmission T and its variation ΔT in logarithmic scale; (b) Asymmetry of T in logarithmic scale.

III.2 Cathodoluminescence experiments

As previously demonstrated by the photoluminescence experiment, we can detect the luminescence generated by the electron-hole recombination in the QW's in the transmission geometry. The issues that we will address in this paragraph are:

i) Can luminescence be also detected upon electron transmission?

ii) Does the luminescence intensity depend on the orientation of incident electron spin polarization with respect to the Fe layer magnetization?

We will first start to describe our experiment dedicated to the cathodoluminescence measurement. The experiment set-up has been modified to implement a luminescence spectroscopy in transmission mode.

III.2.1 The optical detection setup

The optical detection of the electron transmission through metal / semiconductor structure has first required the design of a new sample holder which, on one hand, allows taking electrical contacts on both the front and back terminals of the sample and, on the other hand, is equipped with a lens of short focal length and large numerical aperture to efficiently collect the luminescence emitted from the backside (substrate) of the sample (Figure 3.8).

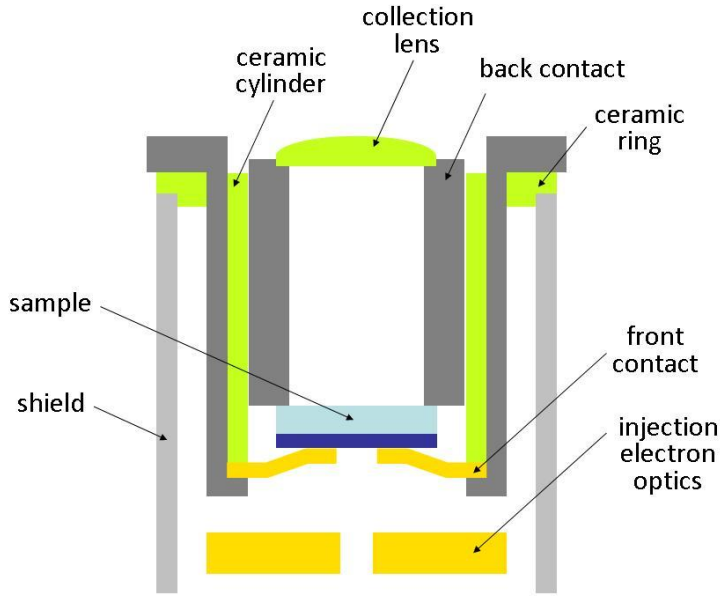

Figure 3.8: Schematics of the sample holder. The front contact is taken on a diaphragm which limits the injection area. The back contact is taken on a metallic cylinder isolated from the front contact by a ceramic cylinder. The luminescence collecting lens is held on the top of the back contact cylinder.

A window just behind the sample backside gives a free optical access for luminescence detection. The luminescence spectroscopy setup is installed outside the UHV chamber. A spectrometer is coupled to a photomultiplier tube equipped with a S1 cathode (see Figure 3.9). We use a high pass (in wavelength) optical filter with an 800 nm cut-off in order to eliminate visible parasitic light. When performing cathodoluminescence experiments we measure simultaneously the total injected current at the collector (substrate) of the junction.

Optical alignment is first obtained by performing PL measurement. A red laser at 660 nm is used to excite the GaAs substrate through a cold mirror. The collected GaAs photoluminescence spectrum is fully reflected by the cold mirror and focused on the entrance slide of the spectrometer.

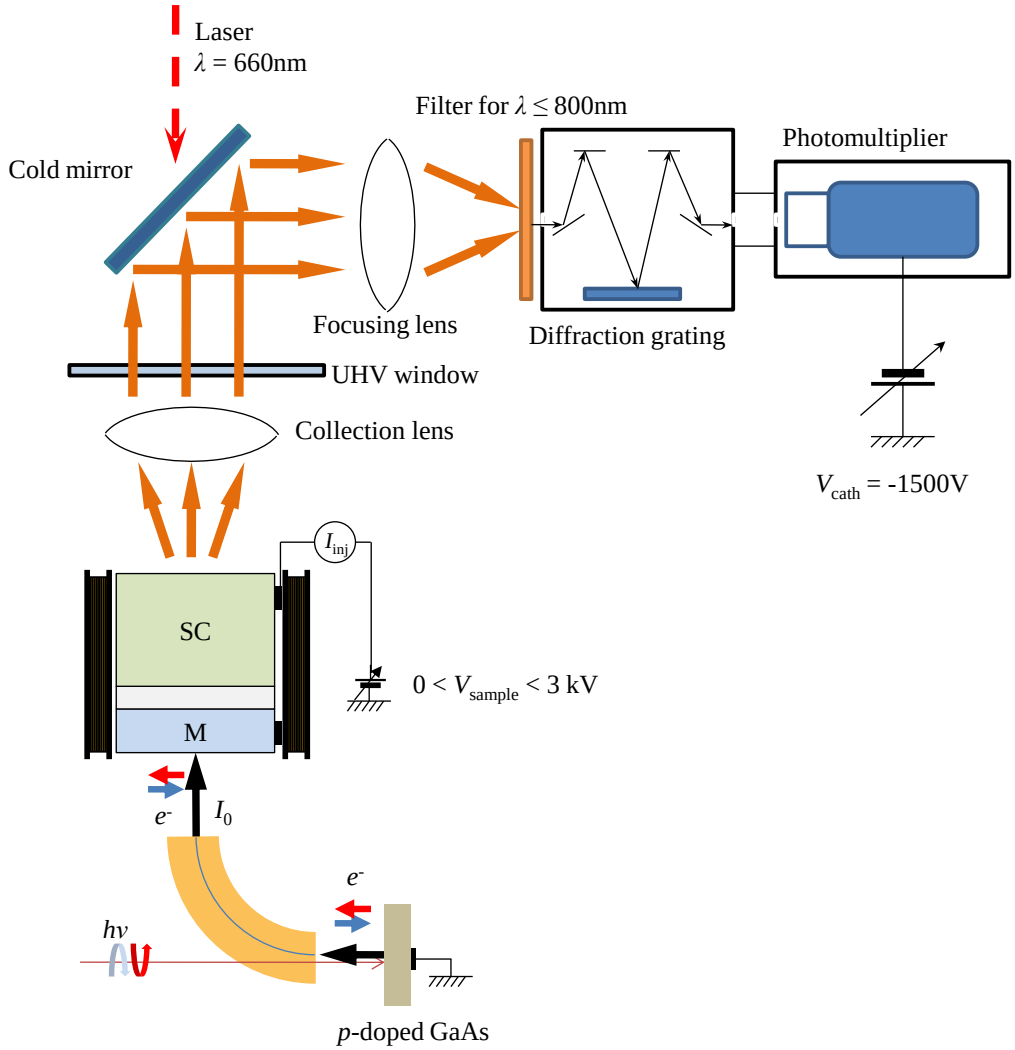

Figure 3.9: Cathodoluminescence setup combining electron injection and luminescence detection. The luminescence spectrum is measured with a spectrometer (a diffraction grating of 600 lines/mm blazed at 1 μm) coupled to a photomultiplier tube cooled at 200 K. All components of the optical detection are enclosed into a dark chamber in order to minimize the dark current of the photomultiplier. A red laser can be used to illuminate the GaAs substrate of the sample through a cold mirror. This allows photoluminescence measurements for alignment and calibration of the luminescence spectroscopy setup.

The Figure 3.10 compares the photoluminescence spectrum measured in the UHV setup with the one measured previously with the sample outside the chamber. Both spectra are recorded in the RR geometry with red lasers of different powers. As expected no

luminescence signal from QW's is observed since all the light is absorbed in the GaAs substrate. Our optical setup connected to the ultra high vacuum chamber allows to retrieve the GaAs PL results obtained in air. The main difference comes from the shape of the broad peak beyond 1000nm. This difference comes from the photomultiplier detector response in the high wavelength range.

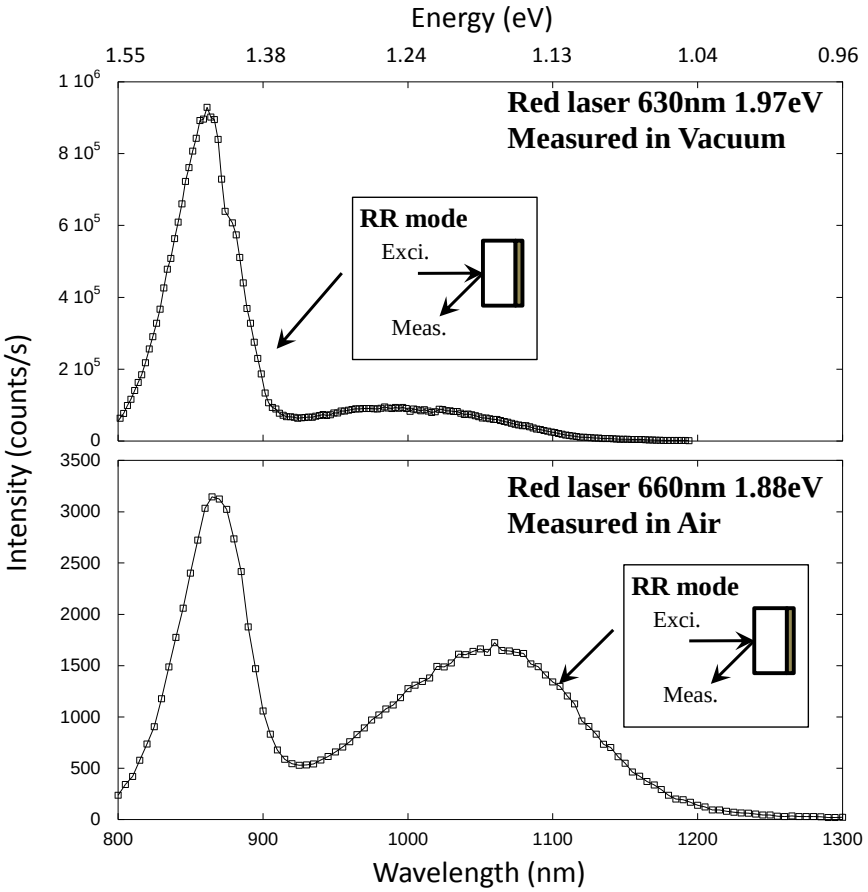

Figure 3.10: Comparison of the PL spectra recorded with sample under vacuum and in air in RR mode.

The CL spectrum can then be measured when turning on the electron beam. Setting the injection energy at 2.5 keV, where a large number of secondary electrons are generated in the front layer of the sample, we obtain the CL spectrum of Figure 3.11 for 100 nA of injected current. It exhibits the luminescence peak centered at the QW's ground state transition energy

(1.26 eV) and no contribution from the GaAs is observed. By comparison we show the PL spectrum recorded *ex-situ* in the transmission mode with red light excitation. The broad high-wavelength peak associated with the luminescence in the n^+-substrate seen in the PL spectrum does not appear in the CL spectrum. It means that transmitted electrons all recombine in the QW's and none have enough energy to overcome the AlGaAs barrier and recombine into the n^+-doped GaAs region.

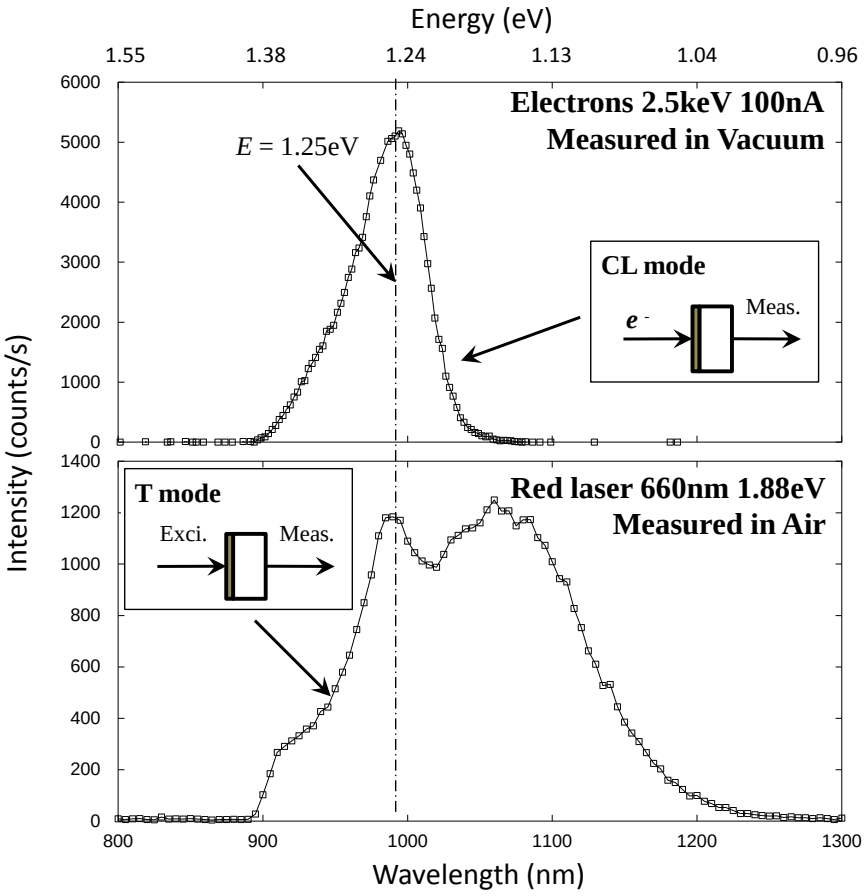

Figure 3.11: Comparison between the cathodoluminescence and the photoluminescence spectra in the same excitation geometry. CL spectrum is obtained for an injected electron beam of intensity 100 nA and of energy 2.5 keV.

Since the cathodoluminescence spectrum only exhibits the contribution from the QW's, electron transmission can be more efficiently detected by integrating the optical signal over the whole luminescence spectrum. This can be straightforwardly obtained by suppressing the

spectrometer and detecting directly the total luminescence light intensity. Figure 3.12 compares the CL signal collected with and without spectrometer for an injection energy of 1 keV. The cathode potential is scanned between – 4.2 V and – 3.2 V so that the measured luminescence signal replicates the injected electron distribution curve (EDC) measured simultaneously and plotted on the same graph. The EDC maximum coincides at – 3.65 V with the maximum of CL signal and no luminescence signal is detected out of the EDC. Interestingly enough working without spectrometer leads to gain a factor 6 on the CL intensity without any parasitic signal. Therefore we will adopt this configuration for the next CL experiments.

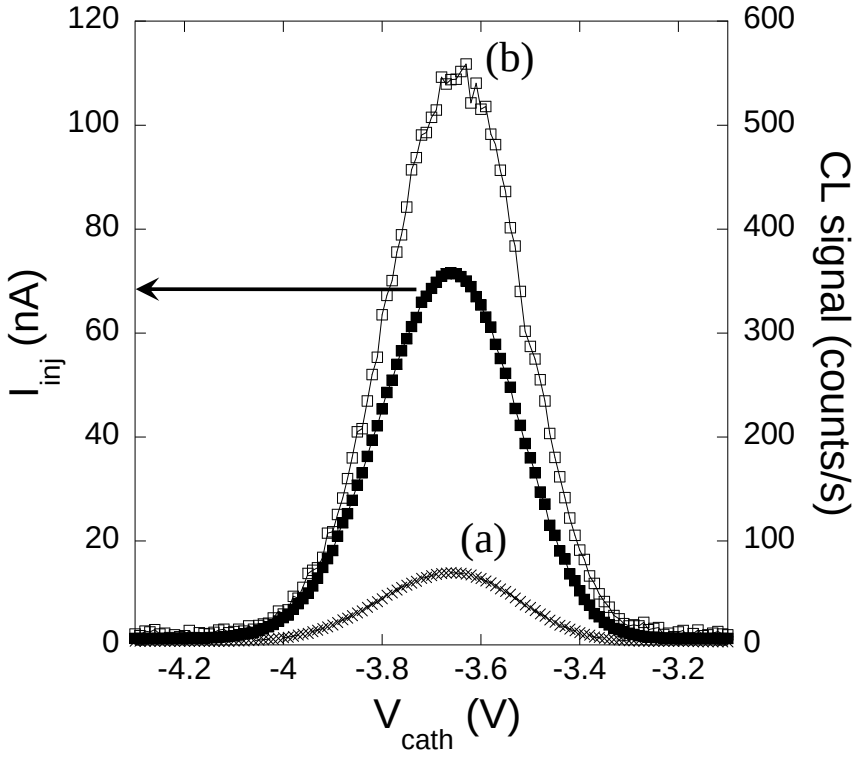

Figure 3.12: Variation of the cathodoluminescence signals versus the energy distribution of the injected electrons for the injection energy of 1 keV. (a) CL signal detected with the spectrometer; (b) CL signal detected without the spectrometer. The spectrometer is set at the maximum luminescence peak (984 nm). The background noise increases from 3 counts/s on average with spectrometer to 8-10 counts/s without spectrometer.

III.2.2 Cathodoluminescence intensity versus injection energy

While fixing the voltage on the photocathode at the EDC maximum, i.e. at – 3.65 V, we measure at the same time the injected current and the CL signal as a function of the injection energy. In Figure 3.13, the CL intensity is compared to the electrically-detected transmission.

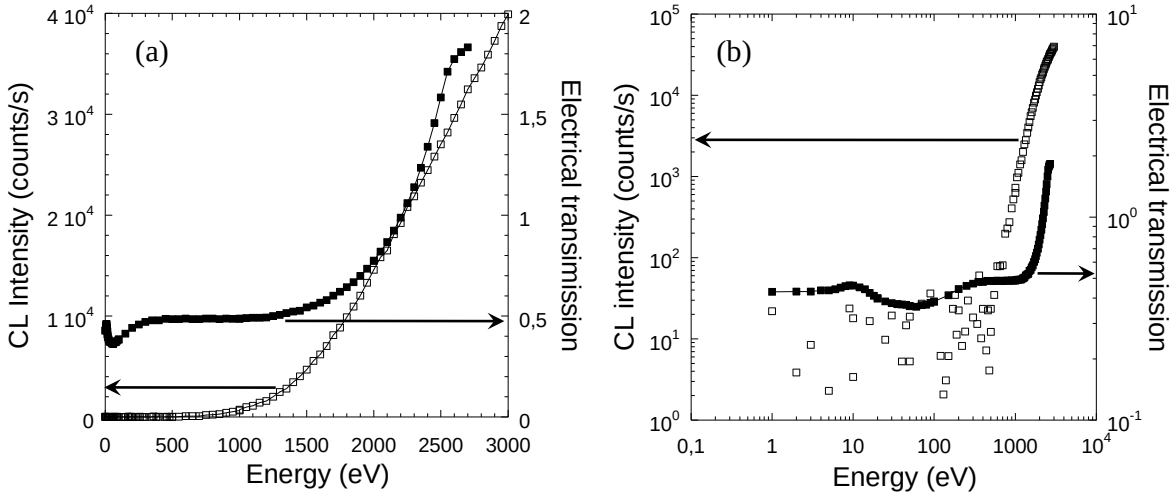

Figure 3.13: Cathodoluminescence induced by injecting unpolarized electrons in the junction InGaAs_1 (normalized to 100 nA of injected current) versus injection energy (a) in linear scale and (b) in logarithmic scale. The CL acquisition time is 10 s per point. The background is subtracted.

The onset of the cathodoluminescence signal occurs at 400 eV. Below this injection energy, no luminescence signal is detected while the transmitted current exhibits a high and constant value. Since CL is directly proportional to the number of electrons transmitted into the QW's region of the semiconductor collector, it is clear that the absence of a CL signal correlated with the high detected transmitted current at low injection energy tends to indicate that this high collector current does not correspond to hot-electron transmission through the metal / semiconductor junction. One could bring up the presence of pin holes in the metal to explain the high collected current at low injection energy. But the overall pinhole cross section would be very large since the collected current corresponds to half of the injected current. In this case the luminescence signal should exhibit a much larger value even at low

injection energy [Bréchet88, Fromme89, Alperovitch05].

Above 400 eV of injection energy, the cathodoluminescence signal increases by three orders of magnitude between 400 eV and 3000 eV of injection energy while the collector current start to increase significantly only above 1200 eV, and at 2500 eV it reaches a value only about four times larger than its low energy value.

At this point, the only correlated features between the variations of the luminescence intensity and the collector current as a function of the injection energy is the increases exhibited by these two signals at high injection energy. But it appears difficult to obtain coherent interpretations of these two quantities especially below 1200 eV.

Let us consider the variation of the CL intensity versus the injection energy. The luminescence intensity is related to the number of transmitted electrons in the semiconductor.

We can describe the transmission through the junction by the following expression:

$$T \approx \int_0^\infty \alpha(\varepsilon) F(\varepsilon) d\varepsilon \qquad (3.1)$$

where $F(\varepsilon)$ is the electronic distribution at the metal / semiconductor interface and $\alpha(\varepsilon)$ is the transfer probability from the metal into the semiconductor. Let us consider the simple case where $\alpha(\varepsilon)$ is zero for electron of energy ε smaller than E_G (the GaAs bandgap width) and $\alpha(\varepsilon)$ is equal to 1 for electron of energy ε larger than E_G. We also consider a convenient exponential shape for the electron distribution: $F(\varepsilon) = M \exp(-\varepsilon / E_M)$, where M is a multiplication factor which accounts for the secondary electron cascade and E_M is the mean electron energy. When assuming that on average the injection energy E_0 of an incident electron is shared by M secondary electrons of mean energy E_M, the multiplication factor is given by: $M = E_0 / E_M$. Then the transmission simply writes:

$$T \approx \frac{E_0}{E_M} exp\left(-\frac{E_G}{E_M}\right). \quad (3.2)$$

The mean energy E_M characterizes the width of the electron distribution at the metal / semiconductor interface. If E_M does not depend on E_0, only the intensity of the electron distribution and not its shape depends on E_0 and it is expected that T increases linearly with E_0. This linear regime is usually observed in electron transmission experiments for low injection energy (typically below 100 eV). Then, it is clear that any variation of T stiffer than linear should be due to an increase in the electron distribution width, which is an increase in E_M. The determination of the variation of E_M with E_0 requires a model which describes energy and momentum relaxation taking into account the variation of the electron mean-free-path over the entire considered energy range [Rougemaille08]. It is clear that this kind of description depends on many adjustable parameters and that the main virtue of such a model is that it provides a physical image of the formation of the electronic distribution in the metal layer. This image is all summed up in the variation of E_M versus E_0. Let us thus short circuit the technical description of the formation of the electronic distribution in the metal and try instead to find a simple and reasonable expression for the variation of E_M with E_0 that allows to fit with Eq. (3.2) the variation of the CL intensity versus E_0. Since, as discussed above, it can be assumed that in the low injection energy range E_M is constant, we may consider the following expression for E_M:

$$E_M \approx E_M^0 + b(E_0) \quad (3.3)$$

where E_M^0 is constant. For $b(E_0)$ we can consider different functions which describe an increase of E_M at high injection energy. We have tested basic power-law functions and we have found that a simple quadratic expression $b(E_0) = E_0^2 / \beta$ gives a satisfactory description in the probed energy range. In Figure 3.14 we have plotted the variation of T versus E_0 calculated after Eq. (3.2) and (3.3) when taking $E_M^0 = 0.14$ eV and $\beta = 10^7$ eV. It is compared with the experimental variation of the CL intensity. The simple phenomenological model that

we use to describe electron transmission accounts reasonably well for the variation of the CL intensity as a function of injection energy. The linear regime predicted by the model at low injection energy is not observed since it corresponds to CL intensities (for the present sample) lower than the detection limit of our setup. But the transmission increase due to the broadening of the transmitted electronic distribution at high injection energy reproduces very well the variation of the CL intensity. We can thus reasonably conclude that the CL measurement provides a reliable detection of the electron transmission through the metal / semiconductor junction. Note that the discrepancy between optical and electrical measurements of the electron collection into the semiconductor indicates that the interpretation of the electrical measurements in the case of a poor rectifying junction is not straightforward.

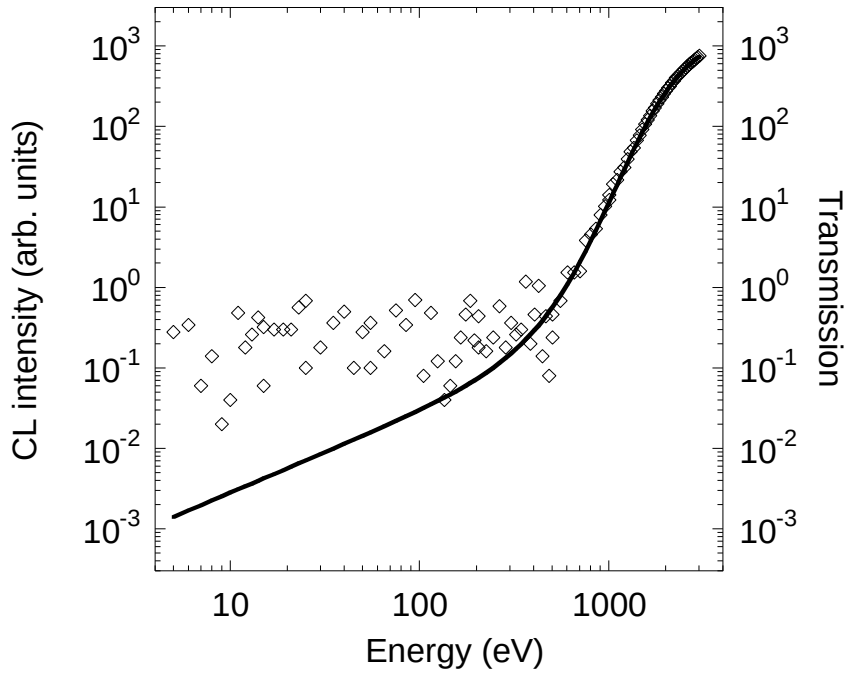

Figure 3.14: Compared variation between the CL intensity (symbols) and the calculated transmission (line) versus the injection energy. Note that the fitted transmission predicts a transmission value of 200 at 2000 eV when considering that the metal / semiconductor interface is fully transparent to electrons of energy larger than the GaAs bandgap.

Finally note that the variation of E_M versus E_0 is very similar to the one obtained from the full transport model previously proposed to describe electron transmission in metal / oxide / semiconductor structure [Rougemaille08]. This model allowed to account well for the electrical measurements of electron transmission in junctions with good rectifying properties

III.2.3 Spin asymmetry in the cathodoluminescence intensity

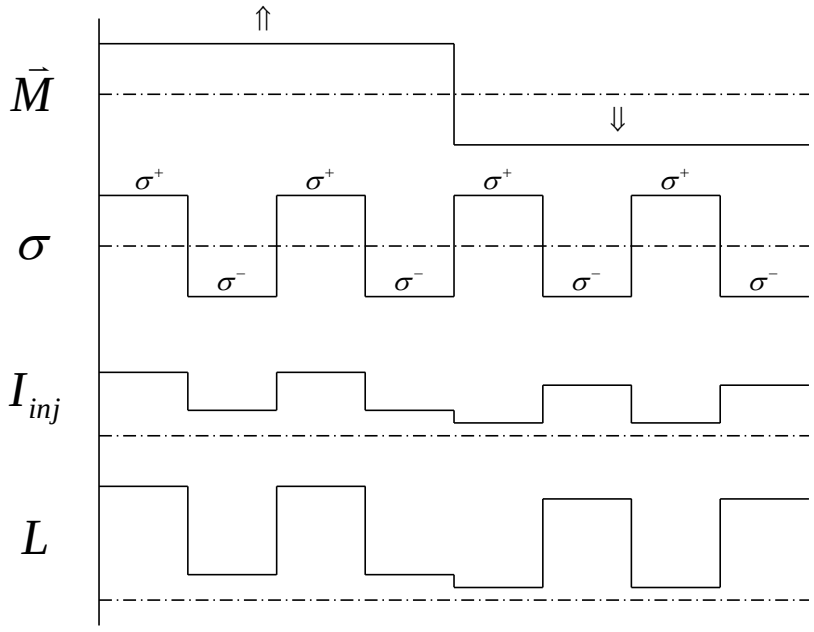

Figure 3.15: For a given saturated magnetization, the total injected current I_{inj} and the intensity of cathodoluminescence L are measured at the same time, while the polarization of the injected electron beam is modulated between spin parallel and antiparallel to the direction the magnetization. Typically the cycle of light excitation (σ^+, σ^-) is a 2 s run. The magnetic field applied to reverse the magnetization is 100 G.

We use the following experimental procedure described in Figure 3.15. Switching between positive and negative helicities of the light polarization allows us to modulate electron spin polarization relative to the fixed magnetization. The spin-dependent cathodoluminescence signal is given by the asymmetry $A_{CL} = (L^+ - L^-) / (L^+ + L^-)$, where L^+

(respectively L^-) is the luminescence intensity when injecting electrons of polarization $+P_0$ (respectively $-P_0$), excited by σ^+ (respectively σ^-) polarized light. The signature of the spin-dependent effect is checked by reversing the saturated magnetization, since it gives a change in sign of the asymmetry.

Ideally the injected current measured at one of the junction terminals should be constant, whatever the exciting light polarization. But in the practical case, due to the conjunction of temperature variation in the Pockels Cell and / or slight changes in the injected current when switching the light polarization, we have to take into account the asymmetry of the injected current: $A_I = (I^+ - I^-) / (I^+ + I^-)$, where I^+ and I^- are the injected current intensities corresponding respectively to the excitation of the photocathode with σ^+ and σ^- circular polarized light. So the actual spin asymmetry of the cathodoluminescence A is obtained from the difference between the measured CL asymmetry and the injected current asymmetry: $A = A_{CL} - A_I$. The background on the CL intensity detection (of typically 10 counts/s) is measured when switching off the photocathode light excitation (no electron beam) and is subtracted from the L^+ and L^- counting rates.

Let us now make a few comments concerning the counting statistics to estimate the accuracy that should be associated with the luminescence measurement. We expect to measure luminescence asymmetries of 10^{-3}. Considering that the raw counts follow a Gaussian distribution, at least 10^6 photon counts are needed to attain the desired error bound. Looking at the CL signal of Figure 3.13, the counting time should range from 10^3s to 10^5s depending on the injection energy.

In practice, we modulate the electron spin polarization between $+P_0$ and $-P_0$) (i.e. the excitation light polarization between σ^+ and σ^-) at a frequency of 0.5 Hz and we measure A_{CL} and A_I over each modulation cycle. Then we draw the running average variation of A_{CL} versus the number of cycles. The running average value of $\overline{A}_{CL}$ after N cycles is defined as:

$$\overline{A}_{CL} = \frac{1}{N}\sum_{i=1}^{N} A_{CL}(i) \tag{3.4}$$

i being the cycle number. The total number *N* of cycles runs as long as the statistical accuracy is not reached.

Figure 3.16 shows an example of the variation of the current and luminescence running average asymmetries. It clearly shows how respective average values build up cycles after cycles. Here the injected current is 100 nA and the injection energy is 1 keV. In these conditions, at least 1000 cycles are mandatory to get reliable averaging.

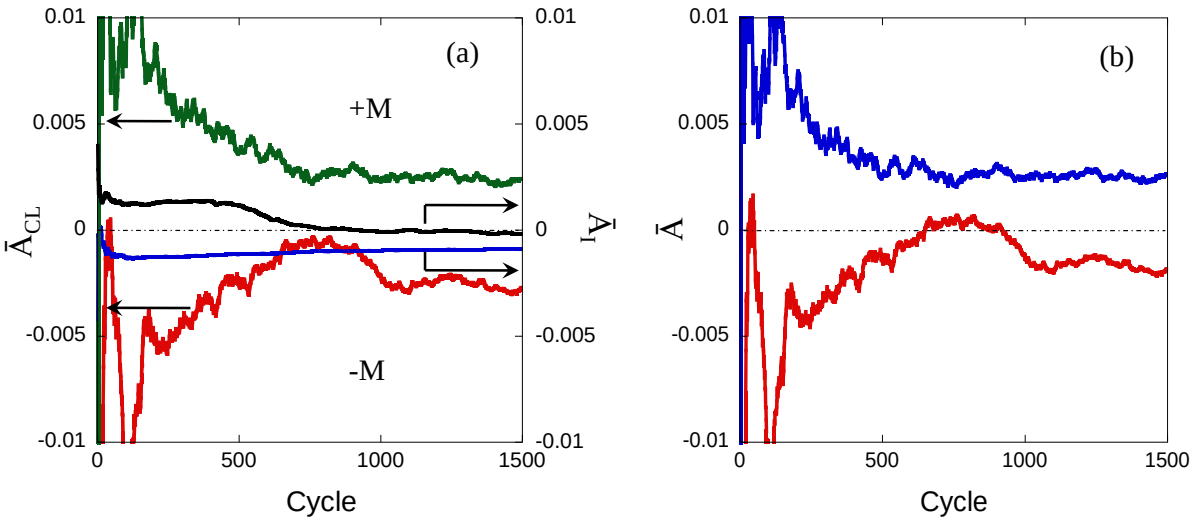

Figure 3.16: a) Evolution of the average asymmetries of luminescence and absorbed currents at 1 keV as a function of the number of polarization modulation cycles. Negative asymmetry values are obtained by reversing the saturated magnetization. The injected current is 100 nA for both σ^+ and σ^- polarizations. Injection energy of 1 keV. b) Evolution of the actual average CL asymmetry $\overline{A} = \overline{A}_{CL} - \overline{A}_I$ versus the number of polarization modulation cycles).

After 1500 measurements, the CL asymmetry is 0.26 %, when the magnetization is parallel to the incident polarization and of – 0.18 % when the magnetization is antiparallel to the polarization. The change in sign of asymmetries between + M and – M configuration unveils the spin-dependent character of the electron transport. To give further details on the

counting statistics, for all measurements done below 1 keV of injection energy, 5000 acquisition cycles have been performed. At higher injection energy, the signal-to-noise is significant enough to reduce the number *N* of cycles to 1500. The complete variation of the cathodoluminescence asymmetry is shown on Figure 3.17. The maximum value of asymmetry is 2×10^{-3} and it is obtained at 400 V, the onset of cathodoluminescence and around 1000 V. Above 1200 V the signal becomes zero. Right now we cannot interpret this variation and we will only give a qualitative description to explain the origin of asymmetry.

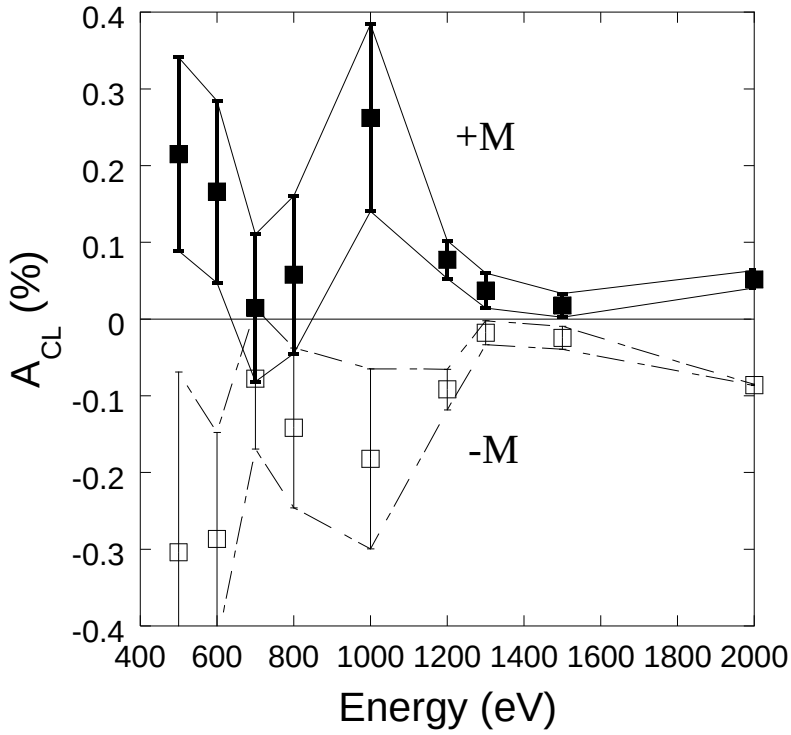

Figure 3.17: Variation of the cathodoluminescence asymmetry A_{CL} versus the electron injection energy. The curves referred as +M and –M correspond to the two Fe saturated magnetizations. The injected current is 100 nA for each (σ^+, σ^-) excitation cycles. The vertical bars are the error bars associated with experimental data (the total length of the error bar is equal to two times the standard deviation).

We can give a quantitative description of the cathodoluminescence asymmetry induced by the incident electron polarization P_0. Let us consider n_0^+ and n_0^- the numbers of injected spin up and spin down electrons. For σ^+ polarized light excitation we have $n_0^+(\sigma^+)$

$= n_0 (1 + P_0) / 2$ and $n_0^- (\sigma^+) = n_0 (1 - P_0) / 2$, where $n_0 = n_0^+ + n_0^-$ is the total number of injected electrons. Identically, the σ^- light generates the population of spin-polarized electrons $n_0^+(\sigma^-) = n_0 (1 - P_0) / 2$ and $n_0^-(\sigma^-) = n_0 (1 + P_0) / 2$. The spin-dependent transmission through the Fe layer can be described by the diagonal transmission matrix

$$T = \begin{pmatrix} t^+ & 0 \\ 0 & t^- \end{pmatrix}. \tag{3.5}$$

The number of transmitted electrons is then given by the relationship

$$\begin{pmatrix} n^+ \\ n^- \end{pmatrix} = T \begin{pmatrix} n_0^+ \\ n_0^- \end{pmatrix}. \tag{3.6}$$

We find that the total number of transmitted electrons is $n(\sigma^{+/-}) = n^+ + n^- = N (1 \pm s P_0) (t^+ + t^-) / 2$ where $s = (t^+ - t^-) / (t^+ + t^-)$ is the Sherman function of the iron spin filter. The luminescence asymmetry is proportional to the ratio $(n^+ - n^-) / (n^+ + n^-) = s P_0$. Thus, the measured asymmetry is the combined effect of the initial spin polarization with the spin filtering efficiency of the ferromagnetic layer. In the case of a perfect spin filter ($s = 1$), the asymmetry is equal to the initial spin polarization P_0. Taking for s a typical value of 0.4 and $P_0 = 0.25$, we find an asymmetry of 0.1. This estimation only accounts for ballistic electron transport through the metal layer. However, since primary electrons relax their energy and momentum across the metal by exciting a secondary electron cascade, one has to take into account the effective polarization seen by the spin filter which is different from P_0. Indeed, according to the simple model presented in the previous section, at a given energy ε, the total number of electrons is given by E_0 / ε, that is the energy of the incident electron is spread over E_0 / ε secondary electrons of energy ε. Thus, assuming that the secondary electron distribution is given by

$$F(\varepsilon) = \frac{1}{E_M} \frac{E_0}{E_M} \exp\left(-\frac{\varepsilon}{E_M}\right), \tag{3.7}$$

the distribution of primary electrons which carry the polarization is

$$F_P(\varepsilon) = \frac{1}{E_M}\frac{E_0}{E_M}\frac{\varepsilon}{E_0}\exp\left(-\frac{\varepsilon}{E_M}\right) = \frac{1}{E_M}\frac{\varepsilon}{E_M}\exp\left(-\frac{\varepsilon}{E_M}\right). \quad (3.8)$$

The primary electron transmission thus writes

$$T_P = \int_0^\infty \alpha(\varepsilon)F_P(\varepsilon)d\varepsilon\, F_P(\varepsilon) = \left(1+\frac{E_G}{E_M}\right)\exp\left(-\frac{E_G}{E_M}\right). \quad (3.9)$$

When considering that primary electrons carry a polarization P_0 and that the filtering efficiency is given by s, we find for the asymmetry:

$$A_{CL} = P_0 s\frac{T_P}{T} = P_0 s\frac{E_G + E_M}{E_0}. \quad (3.10)$$

Note that $E_G + E_M$ represents the average energy of the transmitted electrons. Thus it is expected that the asymmetry decreases like $1 / E_0$ because of the dilution of the incident polarization by secondary electrons. However, a deviation from this simple law can be observed when E_M increases. Moreover, for large value of E_M (compared to the exchange energy in Fe) s may decrease. Thus, the variation of A_{CL} may be non monotonous in the injection energy range where E_M varies significantly. This could explain the experimental variation of A_{CL} which exhibits a maximum for $E_0 = 1000$ eV. However, again taking $P_0 = 0.25$, $s \approx 0.4$, and $E_G = 1.42$ eV, a simple calculation shows that, for $E_0 = 1000$ eV, the asymmetry should be of the order of 0.01 % which is about 10 times smaller than the value actually measured.

As a conclusion, we have found that the CL emitted from the GaInAs_1 structure under injection of spin-polarized electrons exhibits spin asymmetry which takes a maximum value of about 0.2 % at an injection energy of 1000 eV. A simple estimation of the spin filtering effect through the ferromagnetic metal layer as a function of the injection energy provides a

value of the transmission spin-asymmetry about ten times smaller that the experimental CL asymmetry. However, the measurement of the CL spin asymmetry is hampered by a poor accuracy. The main drawback of the CL measurement is related to its very low efficiency (of the order 10^{-9} photons per electron injected at 1000 eV). Further exploitation of CL technique to the study of spin filtering effects would require improving the sensitivity of the measurement set up as well as the efficiency of the CL process itself. On the other hand, because of the complexity of the electron transmission process, calculations of the expected asymmetry rely on very rough approximations which neglect spin relaxation and exchange integral effects. The interpretation of the experimental data would thus require a better understanding of the cascading process taking into account the different aspects of the spin dependent interactions in the ferromagnetic material.

Conclusion and perspective

We have studied the spin-dependent transport of hot electrons into a two terminal hybrid structure composed of the Fe / Oxide / *n*-doped GaAs and Co / Oxide / *n*-doped Si junctions. The collected current corresponds to electrons, which have surmounted the oxide barrier height and the semiconductor band bending. The electron injector being spatially separated from the target, the injection energy can be easily scanned from 10 to 3000 eV and the initial spin polarization modulated between + 0.25 and – 0.25 to evidence the spin-filtering effect occurring during the crossing of the ferromagnetic layer. Such transmission experiment amounts to achieve the energy spectroscopy of an electron distribution made up of primary and secondary electrons, which propagates into the junction with a mean energy of a few eV. The mean energy of the distribution depends on the injection energy and on the initial spin polarization.

The investigation of the electron transmission was performed following two different approaches: the electrical method based on the measurement of electrical currents and the optical detection based on the measurement of the cathodoluminescence (CL) intensity resulting from the radiative recombination of the transmitted electrons in quantum wells inserted in the *p*-doped GaAs collector.

The electrical approach ensures the separate and simultaneous measurements of the base and the transmitted currents. However the price to pay relies on samples having excellent Schottky behavior with a very high dynamic resistance of junction. To that effect, we have considered junctions with different thicknesses of oxide layers sandwiched between the ferromagnetic layer and the semiconductor substrate. However, it remains difficult to find out a compromise which provides at the same time good electrical properties and detectable transmission at low injection energy.

On another hand, we did not succeed in unambiguously demonstrating a spin-valve effect by injection of unpolarized electrons in a structure comprising two magnetically decoupled Co layers. We indeed measure a weak spin asymmetry of the order of 3 % only at high injection energy while a much higher value is expected. We do not have a clear explanation for this result.

On the other hand, the optical detection allows us to track electrons transmitted into the GaAs

conduction band, without being restricted by the electrical quality of the Schottky junction. The CL intensity indicates that electron transmission occurs into the GaAs conduction band despite the existence of the band bending barrier. Moreover, the luminescence spin asymmetry evidences spin-filtering effect through the magnetic layer. However the conversion rate defined as the ratio of detected photons per incident electron is so low that it restrains our counting statistics. The figure below shows the variation of the cathodoluminescence quantum yield as a function of the injection energy. One reason for this inefficiency comes from the poor optical yield of the luminescence experiment. We are indeed very far from the yield of doped GaAs which is known as a very efficient light emitter with external efficiencies of the order of 10^{-2} [Craford97].

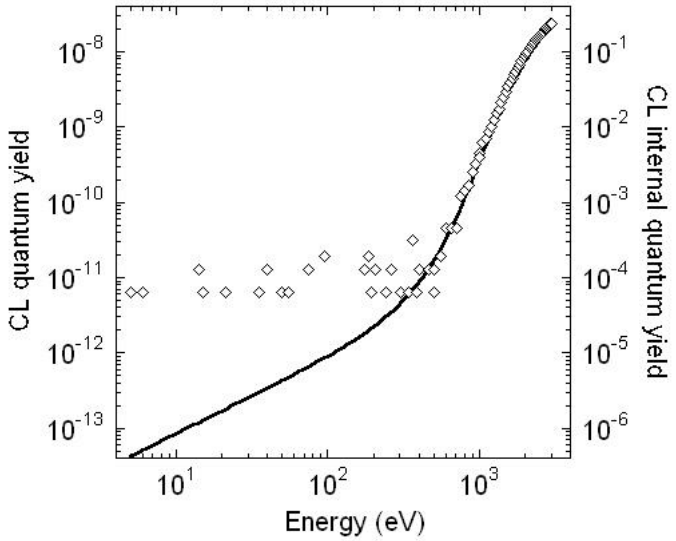

Figure C.1: Variation of the cathodoluminescence external (left axis) and internal (right axis) quantum yield (photons per incident electron) as a function of the injection energy. The solid line represent the variation of the electron transmission (in arbitrary units) calculated after the model described in chapter 3.

To ensure that the optical detection of injected electrons constitutes an attractive alternative, the overall sensitivity of the experiment must be improved in particular at low injection energy. To do so, we have to review the limiting factors in the light detection. First the photomultiplier, which is a S1 cathode, has a quantum-yield of 10^{-3} in the energy range of the GaInAs QW's emission. The following geometrical factors also contribute to the weak detection efficiency: the aperture of the collecting lens is

of the order of 1/3 and provides detection in a solid angle of about 2 % of the half space on the back side of the sample; the light propagation through ten interfaces (lenses, filters, windows…), which gives a loss of intensity of about a factor of 10; and finally the light extraction efficiency of the GaAs sample, i.e. the fraction of emitted photons. Its value is limited by the light reflection, which traps photons inside the sample. In the case of GaAs with n = 3.6, the light extraction in air is equal to 2 %. In total we end up with an intensity loss of 10^{-7}. Now we can estimate the internal quantum efficiency of the structure: it is the fraction of electron-hole pairs reaching the junction, which recombine radiatively. It is limited by non radiative recombination of electron-hole pairs in the band bending of the *p*-doped GaAs. We find the internal quantum efficiency plotted in Figure C.1 (right axis). So, when comparing the experimental CL quantum yield with the calculated electron transmission variation, in order to achieve detection of the CL signal at low injection energy we have to improve the overall quantum yield by at least 2 orders of magnitude. This can be done by changing the detector and optimizing the collection optics. We might expect to gain only a factor 10^2. On another hand, since the internal quantum yield is particularly low in our sample, we can envisage to fabricate a structure in which the non-radiative carrier lifetime is increased. This could be achieved by placing the QW's structure in the flat band regime either by bandgap engineering or by applying a positive bias to the junction.

Finally, let us mention that working with light detection also provides the capability of measuring the spin polarization of electrons [Bréchet88, Alperovitch05] once that they have crossed the spin filter. Indeed, the degree of the recombination light polarization is directly proportional to the electron spin polarization. In this case, to satisfy the selection rules of the optical orientation, electron polarization must be parallel to the light detection direction. Thus, the structure must be characterized by a magnetization perpendicular to the surface. Note that, when measuring the polarization of the transmitted electrons, it is not necessary to inject polarized electrons, since electrons acquire polarization across the magnetic layer. Moreover, the excitation of a secondary electron cascade does not induce a polarization dilution and one can therefore fully benefit from its amplification effect.

Appendix A

Details of samples introduced in the thesis

a) **Sample GaAs_1** (corresponding to sample DP34_1 made in LPMC, Palaiseau)

- Structure: Pd (5nm) / Fe (4nm) / Uvocs (10 Å) / *n*-GaAs
- Substrate: *n*-doped GaAs (10^{16} cm^{-3}), (100)($\pm$ 0.5 deg) orientation
- Surface: 5mm × 7mm

b) **Sample MgO_1** (corresponding to sample 1806R made in LPM, Nancy)

- Structure: Pt (3nm) / Co (5nm) / MgO (2nm) / *n*-Si
- Substrate: *n*-doped Si (10^{15} cm^{-3}), (100)($\pm$ 0.5 deg) orientation
- Surface: 5mm × 5mm

c) **Sample MgO_2** (corresponding to sample 1901R made in LPM, Nancy)

- Structure: Pt (2nm) / IrMn (7.5nm) / Co (5nm) / Cu (3.5nm) / Co (5nm) / MgO (3nm) / *n*-Si
- Substrate: *n*-doped Si (10^{15} cm^{-3}), (100)($\pm$0.5deg) orientation
- Surface: 10mm × 5mm

d) **Sample InGaAs_1** (corresponding to sample InGaAs_1 made in LPMC, Palaiseau; the part without the metal layers corresponds to sample 3246 (VS1-47) made in the Institute of Semiconductor Physics, Novosibirsk)

- Structure: Pd (2nm) / Fe (4nm) / *p*-GaAs:Be (7×10^{17} cm^{-3}) (20nm) / *p*-$In_{0.18}Ga_{0.82}As$:Be ($7\times10^{17}$$cm^{-3}$) (10nm) / *p*-GaAs:Be ($7\times10^{17}$ cm^{-3}) (20nm) / *p*-$In_{0.18}Ga_{0.82}As$: Be (7×10^{17} cm^{-3}) (10nm) / *p*-GaAs (20nm): Be (7×10^{17} cm^{-3}) / *p*-$Al_{0.3}Ga_{0.7}As$: Be (7×10^{17} cm^{-3}) (40nm) / GaAs: Si (2×10^{18} cm^{-3}) (100nm) / n^+-GaAs
- Substrate: n^+-doped GaAs epi-ready, (100) orientation
- Surface: 7mm × 4mm

Appendix B

List of data files introduced in the thesis

All the paths here are following the root path "\thesis_xli\manuscript\data"

Chapter II

Figure 2.6	Raw data file:	IV\GaAs_1\data files\DP34_1_15_02_11-1545_I-V
		IV\GaAs_1\data files\DP34_1_15_02_11-1547_I-V
	Treated data file:	IV\GaAs_1\GaAs_1_IV_dark.QDA
		IV\GaAs_1\ GaAs_1_IV_Redlaser2.15mW.QDA
Figure 2.7	Raw data file:	IV\MgO_1\data files\Nancy_1806R_23_06_10-1237_I-V
		IV\MgO_1\data files\Nancy_1806R_23_06_10-1239_I-V
	Treated data file:	IV\MgO_1\ MgO_1_IV_dark.QDA
		IV\MgO_1\ MgO_1_IV_laser.QDA
Figure 2.9	Raw data file:	IV\MgO_2\data files\Nancy_1901R_16_06_10-1957_I-V
		IV\MgO_2\data files\Nancy_1901R_16_06_10-1959_I-V
	Treated data file:	IV\MgO_2\ MgO_2_IV_dark.QDA
		IV\MgO_2\ MgO_2_IV_laser.QDA
Figure 2.10	Raw data file:	Hysteresis\data files\DP34_1_02_07_09_config_1
		Hysteresis\data files\DP34_1_02_07_09_config_2
	Treated data file:	Hysteresis\GaAs_1_hysteresis.QDA
Figure 2.11	Raw data file:	Hysteresis\data files\1806-R1-rest.res
	Treated data file:	Hysteresis\MgO_1_hysteresis.QDA
Figure 2.12	Raw data file:	Hysteresis\data files\1901-R3-MH_precis_300K-18h49.res
	Treated data file:	Hysteresis\MgO_2_hysteresis.QDA
Figure 2.16	Raw data file:	Cesiation\data files\03_12_09-1713_cesiation_data
	Treated data file:	Cesiation\Cesiation.QDA
Figure 2.19 b	Raw data file:	EDC\data files\30_10_09-1139_EDC_data_average
	Treated data file:	EDC\GaAs_1_EDC_data_500V.QDA

Figure 2.22 Figure 2.23 Figure 2.24	Raw data file: Treated data file:	T_lock-in_auto\GaAs_1\data files\09_12_09-2208_T_auto T_lock-in_auto\GaAs_1\data files\09_12_09-2222_T_auto T_lock-in_auto\GaAs_1\GaAs_1_T_lock_in_auto.QDA
Figure 2.25	Data file:	T_lock-in_auto\GaAs_1\Hysteresis_DP34_1_reproduct.QDA
Figure 2.26 Figure 2.27	Raw data file: Treated data file:	T_lock-in_auto\MgO_1\data files\03_02_10_T_auto_1806R_1 T_lock-in_auto\MgO_1\MgO_1_T_all.QDA
Figure 2.28 Figure 2.29	Raw data file: Treated data file: 	T_lock-in_auto\MgO_2\data files\ Nancy_1901R_2_22_04_10-1902_T_auto_data_normalized T_lock-in_auto\MgO_2\data files\ Nancy_1901R_2_22_04_10-1932_T_auto_data_normalized T_lock-in_auto\MgO_2\ Nancy_1901R_2_22_04_10-1902_T_auto_noFieldPulse.QDA T_lock-in_auto\MgO_2\ Nancy_1901R_2_22_04_10-1902_T_all.QDA

Chapter III

Figure 3.2	Raw data file: Treated data file:	IV\InGaAs_1\data files\24_03_11_I-V_InGaAs_1 IV\InGaAs_1\ InGaAs_1_IV.QDA
Figure 3.3	Raw data file: Treated data file:	Hysteresis\data files\ 2Pd-4Fe-GaAs-InGaAs-45 °-Calibrated-5-average Hysteresis\InGaAs_1_hysteresis.QDA
Figure 3.4	Data file:	Lum_spetro\optical_absorption_GaAs.QDA
Figure 3.5 Figure 3.10 Figure 3.11	Raw data file: Treated data file:	Lum_spetro\data files (folder) Lum_spetro (folder)
Figure 3.6	Raw data file: Treated data file:	T_auto\InGaAs_1\data files\ InGaAs_Oleg_05_07_10-1917_T_auto_data_normalized T_auto\InGaAs_1\InGaAs_1_T_auto_data.QDA
Figure 3.7	Raw data file: Treated data file:	T_lock-in_auto\InGaAs_1\data files\ InGaAs_Oleg_06_07_10-2023_Lock_in_auto_data_normalized T_lock-in_auto\InGaAs_1\InGaAs_1_T_lock_in_auto.QDA

Figure 3.12	Raw data file:	EDC_lum\data files\ InGaAs_1_15_02_11-1617_EDC_lum_data_average
	Treated data file:	EDC_lum\InGaAs_1_EDC_Lum.QDA
Figure 3.13	Raw data file:	Lum_energy\data files\ InGaAs_1_17_09_10-1914_LumNonPola_energy_data
		T_auto\InGaAs_1\data files\ InGaAs_Oleg_05_07_10-1917_T_auto_data_normalized
	Treated data file:	Lum_energy\InGaAs_1_LumNonPola_energy_data.QDA
		T_auto\InGaAs_1\InGaAs_1_T_auto_data.QDA
Figure 3.16	Raw data file:	Lum_time_at_fixed_energy\data files\1000eV\ GaInAs_1_08_12_10-1702_LumPala_1000eV_-M_data
		Lum_time_at_fixed_energy\data files\1000eV\ GaInAs_1_24_01_11-1714_LumPola_1000eV_+M_data
	Treated data file:	Lum_time_at_fixed_energy\ GaInAs_1_LumPola_at_1000V_field_plus_1500CL.QDA
		Lum_time_at_fixed_energy\ GaInAs_1_LumPola_at_1000V_field_minus_1500CL.QDA
Figure 3.17	Raw data file:	Lum_time_at_fixed_energy\data files (folder)
	Treated data file:	Lum_time_at_fixed_energy\selected (folder)
		Lum_time_at_fixed_energy\GaInAs_1_LumPola_Asym_Ep.QDA

References

Introduction

Cacho02: C. cacho, Y. Lassailly, H.-J. Drouhin, G. Lampel, and J. Peretti, *Spin filtering of free electrons by magnetic multilayers: Towards an efficient self-calibrated spin polarimeter*, Phys. Rev. Lett. **88**, 066601 (2002).

Drouhin96 : H. J. Drouhin, A. J. van der Sluijs, Y. Lassailly, and G. Lampel, *Spin-dependent transmission of free electrons through ultrathin cobalt layers*, J. Appl. Phys. **79**, 4734—4739 (1996).

Filipe98: A. Filipe, H.-J. Drouhin, G. Lampel, Y. Lassailly, J. Nagle, J. Peretti, V. I. Safarov, and A. Schuhl, *Spin-dependent transmission of electrons through the ferromagnetic metal base of a hot-electron transistorlike system*, Phys. Rev. Lett. **80**, 2425—2428 (1998).

Getzlaff93: M. Getzlaff, J. Bansmann, and G. Schonhense, *Spin-polarization effects for electrons passing through thin iron and cobalt films*, Solid State Commun. **87**, 467—469 (1993).

Gröbli95: J. C. Gröbli, D. Guarisco, S. Frank, and F. Meier, *Spin-dependent transmission of polarized electrons through a ferromagnetic iron film*, Phys. Rev. B **51**, 2945—2949 (1995).

Heer04 : R. Heer, J. Smoliner, J. Bornemeier, H. Brückl, *Ballistic electron emission microscopy on spin valve structures*, Appl. Phys. Lett. **85**, 4388—4390 (2004).

Hopster82: H. Hopster, R. Raue, E. Kisker, G. Guntherodt, and M. Campagna, *Evidence for Spin-Dependent Electron-Hole-Pair Excitations in Spin-Polarized Secondary-Electron Emission from Ni(110)*, Phys. Rev. Lett. **50**, 70—73 (1983).

Jiang04: 21 X. Jiang, S. van Dijken, R. Wang, and S. S. P. Parkin, *Bias voltage dependence of magnetocurrent in magnetic tunnel transistors*, Phys. Rev. B **69**, 014413 (2004).

Kaidatzis08: A. Kaidatzis, S. Rohart, A. Thiaville, and J. Miltat, *Hot electron transport and a quantitative study of ballistic electron magnetic imaging on Co/Cu multilayers*, Phys. Rev. B **78**, 174426 (2008).

Kinno97: T. Kinno, K. Tanaka, and K. Mizushima, *Ballistic-electron-emission spectroscopy on an Fe/Au/Fe multilayer*, Phys. Rev. B **56**, R4391—R4393 (1997).

Kisker82: E. Kisker, W. Gudat, and K. Schroder, *Observation of a high spin polarization of secondary electrons from single crystal Fe and Co*, Solid State Commun. **44**, 591—595 (1982).

Lassailly94: Y. Lassailly, H.-J. Drouhin, A. J. van der sluijs, and G. Lampel, *Spin-dependent transmission of low-energy electrons through ultrathin magnetic layers*, Phys. Rev. B **50**, 13054 (1994).

Monsma95: D. J. Monsma, J. C. Lodder, Th. J. A. Popma, and B. Dieny, *Perpendicular hot electron spin-valve in a new magnetic field sensor: The spin-valve transistor,* Phys. Rev. Lett. **74**, 5260—5264 (1995).

Oberli98: D. Oberli, R. Burgermeister, S. Riesen, W. Weber, and H. C. Siegmann, *Total Scattering Cross Section and Spin Motion of Low Energy Electrons Passing through a Ferromagnet*, Phys. Rev. Lett. **81**, 4228—4231 (1998).

Pappas91: D. P. Pappas, K. -P. Kämper, B. P. Miller, H. Hopster, D. E. Fowler, C. R. Brundle, and A. C. Luntz, *Spin-Dependent Electron Attenuation by Transmission through Thin Ferromagnetic Films*, Phys. Rev. Lett. **66**, 504—507 (1991).

Penn85a: D. R. Penn, S. P. Apell, and S. M. Girvin, *Spin polarization of secondary electrons in transition metals: Theory*, Phys. Rev. B **32**, 7753—7768 (1985).

Rippard99: W. H. Rippard and R. A. Buhrman, *Ballistic electron magnetic microscopy: Imaging magnetic domains with nanometer resolution,* Appl. Phys. Lett. **75**, 1001—1003 (1999).

Rippard00: W. H. Rippard and R. A. Buhrman, *Spin-Dependent Hot Electron Transport in Co / Cu Thin Films*, Phys. Rev. Lett. **84**, 971—974 (2000).

Rougemaille08: N. Rougemaille, D. Lamine, G. Lampel, Y. Lassailly, and J. Peretti, *Injection energy dependence of spin-polarized hot-electron transport through a ferromagnetic metal / oxide / semiconductor junction*, Phys. Rev. B **77**, 094409 (2008)

Schönhense93: G. Schönhense and H. C. Siegmann, *Transmission of electrons through ferromagnetic material and applications to detection of electron spin polarization*, Annalen Der Physik **505**, 465—474 (1993).

Unguris82: J. Unguris, D. T. Pierce, A. Galejs, and R. J. Celotta, *Spin and Energy Analyzed Secondary Electron Emission from a Ferromagnet*, Phys. Rev. Lett. **49**, 72—76 (1982).

VanDijken03: S. van Dijken, X. Jiang, and S. S. P. Parkin, *Giant magnetocurrent exceeding 3400% in magnetic tunnel transistors with spin-valve base layers*, Appl. Phys. Lett. **83**, 951—953 (2003).

Vescovo95: E. Vescovo, C. Carbone, U. Alkemper, O. Rader, T. Kachel, W. Gudat, and W. Eberhardt, *Spin-dependent electron scattering in ferromagnetic Co layers on Cu(111)*, Phys. Rev. B **52**, 13497—13503 (1995).

Chapter I

Alvarado92: S. F. Alvarado and Philippe Renaud, *Observation of Spin-Polarized-Electron Tunneling from a Ferromagnet into GaAs*, Phys. Rev. Lett. **68**, 1387—1390 (1992).

Cacho02: C. cacho, Y. Lassailly, H.-J. Drouhin, G. Lampel, and J. Peretti, *Spin filtering of free electrons by magnetic multilayers: Towards an efficient self-calibrated spin polarimeter*, Phys. Rev. Lett. **88**, 066601 (2002).

Filipe98: A. Filipe, H.-J. Drouhin, G. Lampel, Y. Lassailly, J. Nagle, J. Peretti, V. I. Safarov, and A. Schuhl, *Spin-dependent transmission of electrons through the ferromagnetic metal base of a hot-electron transistorlike system*, Phys. Rev. Lett. **80**, 2425—2428 (1998).

Grobli95: J. C. Gröbli, D. Guarisco, S. Frank, and F. Meier, *Spin-dependent transmission of polarized electrons through a ferromagnetic iron film*, Phys. Rev. B **51**, 2945—2949 (1995).

Hong00: J. Hong and D. L. Mills, *Spin dependence of the inelastic electron mean free path in Fe and Ni: Explicit calculations and implications*, Phys. Rev. B **62**, 5589—5600 (2000).

Huang07: B. Huang, D. J. Monsma, and I. Appelbaum, *Coherent spin transport through a 350 micron thick silicon wafer*, Phys. Rev. Lett. **99**, 177209 (2007).

Jansen03: R. Jansen, *The spin-valve transistor: a review and outlook*, J. Phys. D: Appl. Phys. **36**, R289—R303 (2003).

Kaidatzis: A. Kaidatzis, S. Rohart, A. Thiaville, and J. Miltat, *Hot electron transport and a quantitative study of ballistic electron magnetic imaging on Co/Cu multilayers*, Phys. Rev. B, **78**, 174426 (2008).

LaBella01: V. P. LaBella, D. W. Bullock, Z. Ding, C. Emery, A. Venkatesan, W. F. Oliver, G. J. Salamo, P. M. Thibado, and M. Mortazavi, *Spatially Resolved Spin-Injection Probability for Gallium*

Arsenide, Science **292**, 1518—1521 (2001).

Lamine07: D. Lamine, *Effet de filtre à spin dans les jonctions métal ferromagnétique / semi-conducteur : transport et effets d'interface*, Ph.D. thesis, Ecole Polytechnique (2007).

Lassailly94: Y. Lassailly, H.-J. Drouhin, A. J. van der sluijs, and G. Lampel, *Spin-dependent transmission of low-energy electrons through ultrathin magnetic layers*, Phys. Rev. B **50**, 13054 (1994).

Monsma95: D. J. Monsma, J. C. Lodder, Th. J. A. Popma, and B. Dieny, *Perpendicular hot electron spin-valve in a new magnetic field sensor: The spin-valve transistor*, Phys. Rev. Lett. **74**, 5260—5264 (1995).

Oberli98: D. Oberli, R. Burgermeister, S. Riesen, W. Weber, and H. C. Siegmann, *Total Scattering Cross Section and Spin Motion of Low Energy Electrons Passing through a Ferromagnet*, Phys. Rev. Lett. **81**, 4228—4231 (1998).

Pappas91: D. P. Pappas, K.-P. Kämper, B. P. Miller, H. Hopster, D. E. Fowler, C. R. Brundle, and A. C. Luntz, *Spin-Dependent Electron Attenuation by Transmission through Thin Ferromagnetic Films*, Phys. Rev. Lett. **66**, 504—507 (1991).

Penn85b: D. R. Penn, S. P. Apell, and S. M. Girvin, *Theory of Spin-Polarized Secondary Electrons in Transition Metals*, Phys. Rev. Lett. **55**, 518—521 (1985).

Rippard99: W. H. Rippard and R. A. Buhrman, *Ballistic electron magnetic microscopy: Imaging magnetic domains with nanometer resolution*, Appl. Phys. Lett. **75**, 1001—1003 (1999).

Rippard00: W. H. Rippard and R. A. Buhrman, *Spin-Dependent Hot Electron Transport in Co / Cu Thin Films*, Phys. Rev. Lett. **84**, 971—974 (2000).

Rougemaille03: N. Rougemaille, Transmission d'électrons chauds, polarisés de spin, dans les jonctions Schottky métal ferromagnétique / semi-conducteur, Ph.D. thesis, Ecole Polytechnique (2003).

Rougemaille08: N. Rougemaille, D. Lamine, G. Lampel, Y. Lassailly, and J. Peretti, *Injection energy dependence of spin-polarized hot-electron transport through a ferromagnetic metal / oxide / semiconductor junction*, Phys. Rev. B **77**, 094409 (2008).

VanDijken03: S. van Dijken, X. Jiang, and S. S. P. Parkin, *Giant magnetocurrent exceeding 3400% in*

magnetic tunnel transistors with spin-valve base layers, Appl. Phys. Lett. **83**, 951—953 (2003).

Vu11: D. Vu, H. F. Jurca, F. Maroun, P. Allongue, N. Tournerie, A. C. H. Rowe, and D. Paget, *Spin-dependent photoelectron tunneling from GaAs into magnetic cobalt*, Phys. Rev. B **83**, 121304 (2011).

Weber01: W. Weber, S. Riesen, H. C. Siegmann, *Magnetization Precession by Hot Spin Injection*, Science **291**, 1015—1018 (2001).

Weber02: W. Weber, S. Riesen, C. H. Back, A. Shorikov, V. Anisimov, and H. C. Siegmann, *Spin motion of electrons during reflection from a ferromagnetic surface*, Phys. Rev. B **66**, 100405 (2002).

Chapter II

Av-Ron78: M. S. Av-Ron, T. H. DiStefano, and I. B. Cadoff, *The nature of electron Tunneling in SiO_2*. The Physics of SiO_2 and Its Interfaces, edited by S.T. Pantelier. New York, Pergamon (1978).

Bernos10: J. Bernos, *Elaboration de jonctions tunnel magnétiques et de jonctions métal / isolant / semi-conducteur pour l'étude du transport et de la précession du spin d'électrons chauds*, Ph.D. thesis, Université Henri Poincaré – Nancy I (2010).

Cacho00: C. Cacho, *Effet de filtre à spin dans les métaux ferromagnétiques par transmission d'électrons de très basse énergie*, Ph.D. thesis, Ecole Polytechnique (2000).

Cacho02: C. Cacho, Y. Lassailly, H.-J. Drouhin, G. Lampel, and J. Peretti, *Spin filtering of free electrons by magnetic multilayers: Towards an efficient self-calibrated spin polarimeter*, Phys. Rev. Lett. **88**, 066601 (2002).

Dekker58: A. J. Dekker, *Secondary Electron Emission*. Solid State Physics, edited by F. Seitz and D. Turnbull, Vol. 6. New York and London (1958).

Drouhin85a: H. -J. Drouhin, C. Hermann, and G. Lampel, *Photoemission from activated gallium arsenide. I. Very-high-resolution energy distribution curves*, Phys. Rev. B **31**, 3859—3871 (1985).

Drouhin85b: H. -J. Drouhin, C. Hermann, and G. Lampel, *Photoemission from activated gallium arsenide. II. Spin polarization versus kinetic energy analysis*, Rhys. Rev. B **31**, 3872—3886 (1985).

Fiederling99: R. Fiederling, M. Keim, G. Reuscher, W. Ossau, G. Schmidt, A. Waag, and L. W.

Molenkamp, *Injection and detection of a spin-polarized current in a light-emitting diode*, Nature **402**, 787—790 (1999).

Hermann85: C. Hermann, G. Lampel, and V. I. Safarov, *Optical pumping in semiconductors*, Ann. Phys. Fr. **10**, 1117—1138 (1985).

Houdre85: R. Houdré, *Photoemission de puits quantiques et de superréseaux GaAs / GaAlAs en état d'affinité électronique négative*, Ph.D. thesis, Université de Paris – Sud (1985).

James69: L. W. James and J. L. Moll, *Transport properties of GaAs obtained from photoemission measurements*, Phys. Rev. **183**,740—753 (1969).

Kiyomura00: T. Kiyomura, Y. Maruo, and M. Gomi, *Electrical properties of MgO insulating layers in spin-dependent tunneling junctions using Fe_3O_4*, J. Appl. Phys. **88**, 4768—4771 (2000).

Kurt10: H. Kurt, K. Oguz, T. Niizeki, and J. M. D. Coey, *Giant tunneling magnetoresistance with electron beam evaporated MgO barrier and CoFeB electrodes*, J. Appl. Phys. **107**, 083920 (2010).

Lampel68: G. Lampel, *Nuclear dynamic polarization by optical electronic saturation and optical pumping in semiconductors*, Phys. Rev. Lett. **20**, 491—493 (1968).

Lamine07: D. Lamine, *Effet de filtre à spin dans les jonctions métal ferromagnétique / semi-conducteur : transport et effets d'interface*, Ph.D. thesis, Ecole Polytechnique (2007).

Meier84: F. Meier and B. P. Zakharchenya, *Optical Orientation*. Modern problems in Condensed Matter Sciences, edited by V. M. Agranovich and A. A. Maradudin, Vol. **8**. North-Holland, Amsterdam (1984).

Ohno99: Y. Ohno, D. K. Young, B. Beschoten, F. Matsukura, H. Ohno, and D. D. Awschalom, *Electrical spin injection in a ferromagnetic semiconductor heterostructure*, Nature **402**, 790—792 (1999).

Parkin04: S. S. P. Parkin, C. Kaiser, A. Panchula, P. M. Rice, B. Hughes, M. Samant, and S.-H. Yang, *Giant tunneling magnetoresistance at room temperature with MgO (100) tunnel barriers*, Nature Materials **3**, 862—867 (2004).

Pierce75: D. T. Pierce, F. Meier, and P. Zürcher, *Negative electron affinity GaAs: a new source of spin-polarized electrons*, Appl. Phys. Lett. **26**, 670—672 (1975).

Rhoderick78: E. H. Rhoderick, *Metal-semiconductor contacts*, Clarendon Press, Oxford (1978).

Rougemaille03: N. Rougemaille, *Transmission d'électrons chauds, polarisés de spin, dans les jonctions Schottky métal ferromagnétique / semi-conducteur*, Ph.D. thesis, Ecole Polytechnique (2003).

Rougemaille08: N. Rougemaille, D. Lamine, G. Lampel, Y. Lassailly, and J. Peretti, *Injection energy dependence of spin-polarized hot-electron transport through a ferromagnetic metall / oxide /semiconductor junction*, Phys. Rev. B **77**, 094409 (2008).

Tantraporn70: W. Tantraporn, Determination of low barrier heights in metal-semiconductor contacts, J. App. Phys. **41**, 4669—4671 (1970).

Uhrmann08: T. Uhrmann, T. Dimopoulos, H. Brückl, V. K. Lazarov, A. Kohn, U. Paschen, S. Weyers, L. Bär, and M. Rührig, *Characterization of embedded MgO/ferromagnet contacts for spin injection in silicon*, J. Appl. Phys. **103**, 063709 (2008).

Zhu01: H. J. Zhu, M. Ramsteiner, H. Kostial, M. Wassermeier, H.-P. Schönherr, and K. H. Ploog, *Room-Temperature Spin Injection from Fe into GaAs*, Phys. Rev. Lett. **87**, 016601 (2001).

Chapter III

Alperovitch05: V.L. Alperovitch, A.S. Terekov, A.S. Jaroshevich, G. Lampel, Y. Lassailly, J. Peretti, N. Rougemaille, and T. Wirth, *Polarized cathodoluminescence induced by very low energy spin-polarized electrons injected in p-GaAs(Cs,O)*, Nuclear Instruments and Methods in Physics Research A **536**, 302—307 (2005).

Bréchet88: Ph. Bréchet, M. Campbell, G. Lampel, D. Paget, Proceedings of the 19th International Conference on the Physics of Semiconductors, vol. 2, 1369 (1988).

Filipe97: A. Filipe, A. Schuhl, and P. Galtier, *Structure and magnetism of the Fe/GaAs interface*, Appl. Phys. Lett. **70**, 129—131 (1997).

Fromme89: B. Fromme, G. Baum, D. Göckel, W. Raith, *Emission of circularly polarized recombination radiation from p-doped GaAs and $GaAs_{0.62}P_{0.38}$ under the impact of polarized electrons*, Phys. Rev. B **40**, 12312—12318 (1989).

Porod83: W. Porod and D. K. Ferry, *Modification of the virtural-crystal approximation for ternary*

III-V compounds, Phys. Rev. B **27**, 2587—2589 (1983).

Rougemaille08: N. Rougemaille, D. Lamine, G. Lampel, Y. Lassailly, and J. Peretti, *Injection energy dependence of spin-polarized hot-electron transport through a ferromagnetic metall / oxide /semiconductor junction*, Phys. Rev. B **77**, 094409 (2008).

Tereshchenko99: O. E. Tereshchenko, S. I. Chikichev, and A. S. Terekhov, *Composition and structure of HCL-isopropanol treated and vacuum annealed GaAs (100) surfaces*, J. Vac. Sci. Technol. A **17(5)**, 2655—2662 (1999).

Tereshchenko11: O. E. Tereshchenko, D. Lamine, G. Lampel, Y. Lassailly, X. Li, D. Paget, and J. Peretti, *Transport and magnetic properties of Fe/GaAs Schottky junctions for spin polarimetry applications*, to appear in J. Appl. Phys. (2011).

Conclusion

Alperovitch05: V. L. Alperovitch, A. S. Terekov, A. S. Jaroshevich, G. Lampel, Y. Lassailly, J. Peretti, N. Rougemaille, and T. Wirth, *Polarized cathodoluminescence induced by very low energy spin-polarized electrons injected in p-GaAs(Cs,O)*, Nuclear Instruments and Methods in Physics Research A **536**, 302—307 (2005).

Bréchet88: Ph. Bréchet, M. Campbell, G. Lampel, D. Paget, Proceedings of the 19th International Conference on the Physics of Semiconductors, vol. 2, 1369 (1988).

Craford97: M. G. Craford, *High brightness light emitting diodes*, in Semiconductors and Semimetals, vol. 48, edited by G.B. Stringfellow, M. Georges Craford, Academic Press, New York, 1997, p. 47.